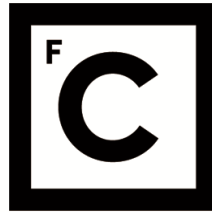UNIVERSIDADE DE LISBOA

FACULDADE DE CIÊNCIAS

Simplified Modeling of Wind-driven Single-sided Ventilation

"Documento Definitivo"

Doutoramento em Sistemas Sustentáveis de Energia

Daniel Pedro Paquito de Albuquerque

Tese orientada por:

Professor Doutor Guilherme Carvalho Canhoto Carrilho da Graça

Documento especialmente elaborado para a obtenção do grau de doutor

2021

2021

UNIVERSIDADE DE LISBOA

FACULDADE DE CIÊNCIAS

Simplified Modeling of Wind-driven Single-sided Ventilation

Doutoramento em Sistemas Sustentáveis de Energia

Daniel Pedro Paquito de Albuquerque

Tese orientada por:

Professor Doutor Guilherme Carvalho Canhoto Carrilho da Graça

Júri:

Presidente:

● Doutor João Manuel de Almeida Serra, Professor Catedrático e Presidente do Departamento de Engenharia Geográfica, Geofísica e Energia da Faculdade de Ciências da Universidade de Lisboa

Vogais:

● Doutor Henry Burridge, Lecturer; Faculty of Engineering do Imperial College London, Reino Unido;

● Doutor Twan van Hooff, Associate Professor; Department of the Built Environment da Eindhoven University of Technology, Países Baixos;

● Doutor Per Heiselberg, Professor; Faculty of Engineering and Science da University of Aalborg, Dinamarca;

● Doutor Fernando Marques da Silva, Investigador Auxiliar; Departamento de Estruturas do Laboratório Nacional de Engenharia Civil - LNEC;

● Doutor Guilherme Carvalho Canhoto Carrilho da Graça, Professor Auxiliar Faculdade de Ciências da Universidade de Lisboa

Documento especialmente elaborado para a obtenção do grau de doutor

2021

"Big whirls have little whirls,

That feed on their velocity,

And little whirls have lesser whirls,

And so on to viscosity."

Lewis Fry Richardson

ACKNOWLEDGMENTS

ABSTRACT

In the last decades there has been an expansion in the use of building mechanical cooling systems. This increase is due to several factors such as global warming, higher internal heat gains, widespread use of unshaded glazed façades and more stringent thermal comfort requirements. In mild to warm climates, buildings without operable windows require mechanical cooling during most of the year, even in moments when the outdoor conditions would allow for natural cooling by ventilation. To reverse this trend designers are encouraged to use natural cooling strategies such as natural ventilation (NV). A well-designed building NV system can reduce building energy use and contain the increasing demand for mechanical cooling systems in buildings. Unfortunately, building designers often struggle when trying to predict the performance of an NV system due, in part, to the lack of precision of the existing simple models for NV airflow in real-world conditions.

This thesis investigates the wind driven NV airflow over a multitude of NV systems: night ventilation (NVC), single sided ventilation (SS1), pumping ventilation (SS2 and CR2), and corner ventilation (CR2). For these NV systems, this thesis developed simplified correlations that improve existing models for predicting these NV airflows.

The results of this research show that NV systems can be modeled using simple correlations that can assist designers in the integration of these systems in modern buildings. The experimental study of NVC showed that this strategy can significantly reduce mechanical cooling load. The study of window effects on wind driven NV in SS1 systems showed that the window geometry can significantly increase the ventilation flow. Finally, the studies on pumping ventilation showed that this recently discovered ventilation mechanism is very prevalent in isolated buildings with SS rooms with two or more openings.

Keywords: Natural ventilation; Night cooling; Single-sided ventilation; Pumping ventilation; Corner ventilation.

RESUMO

Nas últimas décadas, tem havido uma expansão na utilização de sistemas de arrefecimento mecânico de edifícios. Este aumento deve-se a vários fatores, tais como o aquecimento global, maiores ganhos de calor interior, utilização generalizada de fachadas envidraçadas sem sombreamento e requisitos mais rigorosos de conforto térmico. Em climas amenos a quentes, os edifícios sem janelas operáveis requerem arrefecimento mecânico durante a maior parte do ano, mesmo nos momentos em que as condições exteriores permitiriam um arrefecimento por ventilação natural. Para inverter esta tendência, os projetistas têm sido incentivados a utilizar estratégias de arrefecimento natural, tais como a ventilação natural (NV). Um sistema NV bem concebido pode reduzir a utilização de energia pelos edifícios, tão bem como conter a procura crescente de sistemas de arrefecimento mecânico em edifícios. Infelizmente, os projetistas de edifícios debatem-se frequentemente com problemas quando tentam prever o desempenho de um determinado sistema NV. Em parte, estes problemas devem-se à falta de precisão na previsão de caudais de ar de NV por parte dos atuais modelos simples.

Esta tese investiga o caudal de ar de NV induzido pela ação do vento sobre uma variedade de sistemas de NV: arrefecimento noturno (NVC), ventilação mono-fachada (SS1), ventilação por bombagem (SS2 e CR2), e ventilação de canto (CR2). Para estes sistemas NV, esta tese desenvolveu correlações simplificadas que melhoram os modelos existentes para prever estes caudais de ar de NV.

Esta tese está dividida em quatro tópicos principais, e cada tópico apresenta um estudo diferente que partilha uma abordagem comum: uma combinação de métodos experimentais e numéricos que permite avanços no conhecimento sobre o desempenho de cada geometria de ventilação natural. As experiências desta tese abrangem três escalas: escala reduzida (1/20), escala completa de partes da fachada de um espaço e, finalmente, um estudo à escala completa do desempenho da ventilação natural cruzada de um grande átrio de um edifício de escritórios. Esta ampla gama de escalas e detalhes de análise também ocorre para as abordagens numéricas, que vão desde correlações simplificadas a modelos de simulação computacionais LES (*large eddy simulations*).

A primeira parte desta tese apresenta a primeira medição à escala real da redução da carga de arrefecimento devido ao arrefecimento noturno (NVC) num grande edifício de serviços. As medições foram realizadas num grande átrio de um edifício de escritórios que estava exposto a um clima quente. Os resultados confirmaram que o arrefecimento noturno por ventilação

natural pode proporcionar uma redução mensurável na procura de energia de arrefecimento de edifícios de serviços com massa térmica interna exposta. A comparação da carga de arrefecimento diurna medida em dias com tempo semelhante e uma utilização variável do sistema NVC na noite anterior (ligado ou desligado) mostrou que o sistema NVC reduziu a carga de arrefecimento do piso radiante (CF) em 27%. A combinação de duas ferramentas de simulação (EnergyPlus e CFD) utilizadas neste capítulo conseguiu prever a redução da carga de arrefecimento, temperaturas do ar interior e caudais de ar devido a NVC com erros médios de 1.7%, 11.2% e 14.1%, respetivamente. Os resultados apresentados neste capítulo permitiram uma melhor compreensão da expectável redução da procura de energia de arrefecimento que os sistemas NVC podem alcançar. Além disso, os resultados indicaram que a precisão das ferramentas de simulação existentes é adequada para avaliar a poupança de energia esperada, assim como para a viabilidade dos sistemas NVC durante a fase de projeto dos edifícios.

A segunda parte da tese apresenta o primeiro estudo experimental do impacto de oito geometrias típicas de janela em escoamentos de NV SS1 induzidos pelo cisalhamento do vento paralelo à fachada do edifício. As visualizações do escoamento perto de uma abertura plana confirmaram que os escoamentos de SS1 movidos pelo vento em grandes fachadas são o resultado de uma camada de cisalhamento turbulenta que se desenvolve no plano de abertura. Os resultados para as outras sete configurações de janelas mostraram que a combinação entre a geometria da janela e a direção do vento tem um grande impacto na ventilação SS1 (pode variar por um facto de 5). Os resultados das experiências foram incorporados no modelo SS1 simplificado existente mais bem-sucedido (Warren & Parkins), permitindo uma grande precisão na previsão do caudal de NV SS1 induzidos pela ação do vento. Este capítulo identificou também as melhores configurações de janelas para sistemas de NV SS1, induzidos pela ação do vento, em ambientes urbanos densos. Combinando os resultados médios para as velocidades do vento medidas em zonas urbanas, com a medição do desempenho de escoamentos de ar para NV SS1, foi possível propor correlações simples para o SS1, impulsionado pelo vento, em ambientes urbanos que são mais precisas do que os modelos existentes.

Na terceira parte da tese, foi apresentado um conjunto de dados experimentais detalhados do escoamento de ventilação por bombagem. A frequência média de desprendimento de vórtices foi medida utilizando três métodos independentes (visualização com recurso a fumo, HWA e PIV). A frequência média de oscilação medida implica um número Strouhal de 0.10, um valor em linha com os estudos experimentais e numéricos existentes. Os resultados experimentais confirmaram que o caudal de ventilação por bombagem aumenta com a separação das janelas.

Além disso, este estudo revelou uma relação aproximadamente linear entre o caudal efetivo e a separação das janelas. Este capítulo também avaliou a capacidade de métodos de simulação numérica comummente utilizados (LES e URANS) em prever a ventilação por bombagem. LES mostrou ser um método de simulação adequado para a ventilação por bombagem, com um erro médio absoluto de 5%, enquanto os resultados de URANS subestimaram as taxas de ventilação em mais de 40%, mostrando ser um método desapropriado ao estudo de ventilação por bombagem.

Finalmente, a quarta parte da tese apresentou um estudo experimental e numérico da ventilação de espaços, com aberturas numa só fachada e em fachadas adjacentes, inseridos num edifício retangular exposto ao vento. A visualização com recurso a fumo permitiu confirmar a existência de ventilação por bombagem de CR2 (à frente e atrás do modelo) quando o vento estava alinhado com o canto do edifício, e também a transição entre a instável ventilação por bombagem para a estável ventilação cruzada em fachadas adjacentes (CR2) ou na mesma fachada (SS2). Os resultados experimentais mostraram que a ventilação por bombagem ocorre numa gama de ângulos de incidência de vento de: ± 19° para espaços com ventilação mono-fachada (SS2); e ± 9° para espaços com ventilação de canto (CR2). Como resultado, um edifício retangular isolado com múltiplos espaços SS2 e CR2 pode ter ventilação por bombagem em 62% das direções de incidência do vento. Foram realizadas simulações LES para investigar o efeito das componentes da pressão (estática e dinâmica) no mecanismo de ventilação de espaços com configurações SS2 e CR2. Os resultados da simulação LES mostram que a transição da ventilação por bombagem para a ventilação cruzada ocorre quando a pressão estática se torna mais elevada do que a componente dinâmica. Claramente, a ventilação por bombagem é impulsionada pela pressão dinâmica enquanto a ventilação cruzada (para CR2) e a ventilação transversal (para SS2) são impulsionadas pela pressão estática. Os resultados das medições dos caudais efetivos e dos coeficientes de pressão simulados foram utilizados para desenvolver um modelo simples que destaca o efeito da pressão estática e dinâmica e prevê a ventilação por bombagem e a ventilação cruzada em espaços CR2 com precisão de engenharia.

Em suma, os resultados desta investigação mostram que os sistemas NV podem ser modelados utilizando correlações simples que, por sua vez, podem ajudar os projetistas na integração destes sistemas em edifícios modernos. O estudo experimental de NVC mostrou que esta estratégia pode reduzir significativamente a carga de arrefecimento mecânico. O estudo dos efeitos de janela em NV acionada pelo vento em sistemas SS1 mostrou que a geometria da janela pode aumentar significativamente o fluxo de ventilação. Finalmente, os estudos sobre a

ventilação por bombagem mostraram que este mecanismo de ventilação recentemente descoberto é muito prevalente em edifícios isolados cujos espaços são ventilados por mono-fachada e que tenham duas ou mais aberturas.

Palavras-chave: Ventilação natural; Arrefecimento noturno; Ventilação por mono-fachada; Ventilação por bombeamento; Ventilação por fachadas adjacentes.

LIST OF ORIGINAL CONTRIBUTIONS

Paper 1: **Daniel P. Albuquerque**, Mats Sandberg, P.F. Linden, Guilherme Carrilho da Graça, *Experimental and numerical investigation of pumping ventilation on the leeward side of a cubic building*, Building and Environment, Volume 179, 2020, 106897, ISSN 0360-1323, https://doi.org/10.1016/j.buildenv.2020.106897.

Paper 2: **Daniel P. Albuquerque**, Nuno Mateus, Marta Avantaggiato, Guilherme Carrilho da Graça, *Full-scale measurement and validated simulation of cooling load reduction due to nighttime natural ventilation of a large atrium*, Energy and Buildings, Volume 224, 2020, 110233, ISSN 0378-7788, https://doi.org/10.1016/j.enbuild.2020.110233.

Paper 3: **Daniel P. Albuquerque**, Paul D. O'Sullivan, Guilherme Carrilho da Graça, *Effect of window geometry on wind driven single sided ventilation through one opening*, Under review in Energy and Buildings, in 2021.

Paper 4: Guilherme Carrilho da Graça, **Daniel P. Albuquerque**, Mats Sandberg, P.F. Linden, *Pumping ventilation of corner and single sided rooms with two openings*, Under review in Building and Environment, in 2021.

CONTENTS

LIST OF FIGURES

LIST OF TABLES

1. INTRODUCTION

In the last decades there has been an expansion in the use of building mechanical cooling systems [1]. This increase is due to several factors such as global warming, higher internal heat gains, widespread use of unshaded glazed façades [2] and more stringent thermal comfort requirements. In mild to warm climates, buildings without operable windows require mechanical cooling during most of the year [3], even in moments when the outdoor conditions would allow for natural cooling by ventilation. To reverse this trend designers are encouraged to use natural cooling strategies such as natural ventilation (NV) [4]. A well-designed building NV system can reduce building energy use and contain the increasing demand for mechanical cooling systems in buildings [1,5]. Unfortunately, building designers often struggle when trying to predict the performance of an NV system due, in part, to the lack of precision of the existing simple models for NV airflow in real-world conditions [6].

NV airflow can be driven by wind, buoyancy, or a combination of the two. Buoyancy forces are present in most NV flows, yet, even in shielded urban areas, moderate winds can generate forces that dominate the NV airflow [6]. When wind and buoyancy forces are comparable, their contribution to NV flows is difficult to predict, particularly in rooms with multiple openings. In these cases, the interaction between the two forces and the NV opening geometry may increase or reduce the flow [7]. Depending on the relative strength of the driving forces and ventilation opening positions, rooms with two openings will have a NV airflow that can be categorized into one of the following regimes:

- Single sided ventilation (SS, openings in the same façade).
- Cross-ventilation (CV, openings in opposing facades).
- Displacement ventilation (DV, openings at different heights).
- Corner ventilation (CR, openings in perpendicular facades).

To reflect the number of openings, these acronyms can be supplemented by a number, SS1 for a façade with a single opening and SS2 for two openings.

In addition to daytime use, in buildings with exposed internal mass, NV can be used during the unoccupied hours for nighttime precooling of the building for the next day [8]. This heat dissipation passive cooling technique, known as night cooling by NV (NVC), relies on low nighttime air temperature, buoyancy, and wind to achieve convective cooling by ventilation [9]. The effectiveness of NVC strategies varies with climate and building type [10]. To quantify these variations, a recent study proposed a climate cooling potential (CCP) indicator [11].

Existing CCP calculations indicate that, in central and northern Europe, NVC could eliminate the need for daytime mechanical cooling in spaces with high internal mass. In southern Europe, the mean CCP per night for July is less than a third of the value for northern Europe. As a result, in this region, in the warmer months of the year, NVC alone cannot provide sufficient cooling and must be used in combination with mechanical daytime cooling (an approach known as hybrid cooling). The main quantitative indicator of a successful NVC system is its cooling capability. When NVC is used to complement mechanical cooling there should be a measurable reduction in cooling load.

For small rooms of residential buildings or single offices in service buildings, the simplest, most commonly used NV geometry relies on a single openable window (SS1) [6]. When compared to configurations with more NV openings, SS1 systems are easier to integrate into the building layout and simpler to operate. In most cases, SS1 is able to provide controlled natural airflow, avoiding the draft induced thermal discomfort that can occur in NV systems with multiple openings [12]. In the simpler case of a single opening (SS1), whenever moderate wind flows near the façade (1-2 m/s), wind-dominates the flow and buoyancy forces increase mixing and do not reduce the total NV airflow [13]. Therefore, neglecting buoyancy forces is a conservative approach for SS1 flows.

Existing research on wind driven SS1 in plain opening or sash windows shows that this type of flow can be driven by pressure differences or shear [14]. Isolated rectangular buildings have significant static pressure variations along wind exposed façades. Whenever an SS1 opening occupies a relevant part of the façade, these static pressure variations also occur along the opening. In this pressure driven SS1 flow, wind generated pressure defines the inflow and outflow areas that occur in the window open area [15]. For small, isolated buildings with a relatively large façade to window opening area ratio ($A_{op}/A_f \sim 10\%$), the majority of incoming wind directions and opening geometries result in a pressure driven SS1 flow. A recent wind tunnel study of SS ventilation [16] showed that the wind generated pressure difference between two points in a façade is proportional to the distance between the points divided by the façade length scale ($\sqrt{A_F}$). This variation implies that a 1 m^2 opening in a 10 m^2 facade is subjected to a static pressure variation that is one order of magnitude larger than the same opening in a building with a 1000 m^2 façade (such as a 30 m wide ten-story building façade).

Shear driven SS1 flows occur in buildings where the opening to façade ratio is one percent or less ($A_{op}/A_f \sim 1\%$ [17,18]), making the static pressure variation along the opening negligible. In these geometries, typical of large single-story or multistory buildings, wind flows parallel to

2

the façade [19], and the plain opening or sash window SS1 flow is driven by the turbulent shear layer that develops along the opening [20,21]. More specifically, an asymmetric nearly 2D mixing layer that protrudes into the ventilated room [14,22]. Most buildings that are found in modern urban locations have several stories and, as a result, have large façade areas that generate shear driven flows in rooms with SS1 NV systems.

While small rooms often rely on a single ventilation opening, NV systems in larger rooms tend to use two or more openings. From a fluid mechanics perspective, buildings may be regarded as stationary bluff bodies obstructing the wind. On the leeward side of an isolated building, this obstruction creates a wake region surrounded by two shear layers [23]. The interaction of these shear layers is unstable and causes periodic vortex shedding [24], producing a phenomenon known as a Karman vortex street [25]. In addition to the vortex shedding, this unstable interaction can generate natural ventilation (NV) airflow in rooms with two (SS2) or more openings facing the windward or leeward side of the building due to alternating pressure differences at the openings. This recently discovered natural ventilation flow is called pumping ventilation [16,26], in reference to the alternating nature of the shear layer instability that drives it [12].

This thesis investigates the wind driven NV airflow over a multitude of NV systems: night ventilation (NVC), single sided ventilation (SS1), pumping ventilation (SS2 and CR2), and corner ventilation (CR2). For these NV systems, this thesis developed simplified correlations that improve existing models for predicting these NV airflows. Each chapter presents a different study that share a common approach: a combination of experimental and numerical methods that allows for new insights into the performance of each natural ventilation geometry. The experiments span three scales: reduced scale (1/20), full-scale of parts of the façade with a room and, finally, a full-scale study of the natural cross-ventilation performance of a large atrium. This wide array of scales and detail of analysis also occurs in the numerical approaches that go from simplified correlations to large eddy simulation models.

1.1. Research questions

This thesis investigated the following set of research questions in the area of building NV:

1. What is the cooling load reduction from a fully operational NVC system?
2. When does wind shear driven SS1 ventilation occur?
3. How does pumping ventilation vary with window separation (SS2)?
4. Can LES and/or URANS predict pumping ventilation?
5. Can pumping ventilation occur in a CR2 room?
6. What are the wind incident angles for which pumping occurs in SS2 and CR2 rooms?

1.2. Thesis structure

In addition to the introduction (Chapter 1), this thesis is composed by five other chapters. Chapter 2 presents the first measured energy savings due to NVC in a large non-residential building. Chapter 3 presents an experimental study of the impact of typical window geometries on SS1 NV flows driven by wind shear parallel to the building façade using reduced-scale models and a full-scale test chamber. Chapter 4 presents an experimental and numerical study of pumping ventilation in a three-story cubic building with two leeward openings in its middle floor. Chapter 5 presents a reduced-scale measurement of corner ventilation (CR2) and further investigates the scale and occurrence of pumping ventilation in SS2 and CR2 rooms. Finally, Chapter 6 presents the general conclusions of the thesis.

2. NATURAL NIGHTTIME VENTILATIVE COOLING

2.1. Nomenclature

Symbols

ΔC_p pressure coefficient difference [-]

Δp pressure difference [Pa]

ΔP_b pressure induced by buoyancy [Pa]

ΔP_{tot} total pressure [Pa]

ΔP_w pressure induced by wind [Pa]

ε turbulent dissipation rate [m^2/s^3]

κ von Kármán constant [-]

ρ air density [kg/m^3]

$\bar{v}_{air\_in}$ average measured air velocity at the inlet [m/s]

A_{window} window area [m^2]

A_{floor} floor area [m^2]

$C(t_j)$ CO_2 concentration at time t_j [mg/m^3]

C_μ k-ε turbulence model empirical constant [-]

C_{bg} background CO_2 concentration [mg/m^3]

C_{inlet} CO_2 concentration levels measured at the inlet [mg/m^3]

C_{outlet} CO_2 concentration levels measured at the outlet [mg/m^3]

Cp_w specific heat capacity of water [kJ/kg.K]

F bulk volume flow rate [m^3/s]

g gravitational acceleration [m/s^2]

H height [m]

H_{inlet} height of the inlet to the ground [m]

H_{max} maximum height of the building [m]

H_{outlet}	height of the outlet to the ground [m]
k	correlation coefficient between inlet air velocity and the bulk airflow [-]
k	turbulent kinetic energy [m^2/s^2]
k_s	equivalent sand-grain roughness height [m]
L	length [m]
$\dot{m}_{released}$	constant CO$_2$ mass flow rate released during the experiment [mg/s]
$\dot{m}_w$	constant water mass flow rate [kg/s]
n	total number of measured points [-]
P_{local}	local wind driven static pressure [Pa]
Q_{cool}	daily cooling load of the CF system [kWh]
t_j	elapsed time since the initial time of the decay curve [h]
$T_{outside}$	outdoor air temperature [K]
$T_{vertical\ mean}$	mean indoor air temperature [K]
$T_{w,r}$	return water temperature [K]
$T_{w,s}$	supply water temperature [K]
u^*_{ABL}	friction velocity [m/s]
$U(z)$	wind velocity at a given height, z [m/s]
U_H	velocity at building's height [m/s]
U_{ref}	reference wind velocity [m/s]
V_{atrium}	volume of the atrium [m^3]
W	width [m]
z	height to the ground [m]
z_0	aerodynamic roughness length [m]
z_{ref}	reference height of the weather station (=10m) [m]

2.2. Introduction

This chapter presents an experimental and simulation-based analysis of NVC performance in a large atrium. There is a limited number of experimental studies of the impact of NVC in NV cooling capability [27]. An early comparative study using two similar rooms, with and without NVC, showed that NVC can lead to an average daytime maximum temperature reduction of up to 2ºC [28]. Recent field monitoring work of an office building exposed to a mild climate showed that, with low internal gains, an NVC system can keep indoor temperatures within the limits of the adaptive comfort model [29]. Although in some cases, NVC systems can suffer from overcooling [30], the most commonly found limitation is overheating. A recent field study in an academic building found that NVC systems can fail to meet indoor comfort requirements during heat waves and/or periods with high occupancy [31]. An experimental study based in a smart building showed that adequate control of NVC systems is central to consistent performance [32]. There is only one published study of measured cooling energy savings due

to NVC use [33]. This large-scale experimental study analyzed energy data from two hundred fourteen air-conditioned residential buildings, concluding that NVC use resulted in a 26% reduction in the cooling load. To overcome the difficulties of obtaining measured data, several authors have performed studies with annual cooling energy savings predicted using simulation models that are validated using short measurement campaigns (a few hours of data with no measured energy savings). A recent validated thermal simulation-based study [34] showed that, for an office building in southeast China, optimal use of the cool roof and night ventilation can reduce the cooling energy consumption by 28%. A validated thermal simulation-based study [35] of the impact of NVC in supermarkets with high cooling demand showed that NVC can achieve a 17% reduction in cooling annual energy use.

Atrium spaces can be particularly suited to NVC systems due to the large stack height and, in many cases, less stringent thermal comfort requirements. In most cases, atriums are transitional spaces used predominantly for circulation and access to the building. A study of an atrium used as a transitional indoor space concluded that, even with direct inflow of outdoor air at 8ºC (below the typically acceptable minimum for NV systems), the conditions can still be thermally acceptable for circulation [30]. Atriums and other transitional spaces are known to require significant amounts of cooling energy in the summer [36]. A study that measured atrium overheating concluded, using simulation, that NVC can reduce cooling energy demand in atrium spaces with high solar gains [37]. Unfortunately, in some cases, designing a functional NV stack driven system can be challenging due to wind interference [38]. Clearly, NVC systems are potentially effective for atrium spaces with exposed thermal mass and high cooling demand. The relatively low vulnerability to overcooling that characterizes these transitional spaces is a further advantage for successful application of NVC. A review of the thermal and ventilation performance of atriums with NV systems concluded that the existing knowledge on atrium passive designs is incomplete given the complexity and lack of full-scale measurements [39]. A recent review of more than 90 research studies of hybrid cooling systems from 1996 to 2016 [40] identified the need for more experimental studies with field data and full-scale measurements. The abundance of simulation-based studies focused on energy savings contrasts with the lack of studies with measured energy savings due to NV or NVC in non-residential buildings. As a consequence, building system designers lack reliable and accurate data about expected performance and operation of low energy cooling systems [41]. In this context, two significant research gaps were identified in the area of energy savings due to NVC:

- there are no measurements of energy savings due to ventilation-based hybrid cooling systems in non-residential buildings;
- and, consequently, there is not field validation of the simulation tools used to model these systems in the design phase.

To address these research gaps and with the goal of contributing to increased use of NVC systems, this chapter presents an experimental and simulation study of a hybrid-ventilated large atrium of a service building, exposed to the warm summer climate of Southern Europe. The atrium is mechanically cooled during the day by a chilled floor (CF) system and naturally cooled during the night by NVC. The chapter will focus on measuring the cooling load reduction due to the use of NVC and validating the thermal and airflow simulation tools that are used in the design of NVC systems. The next chapter describes the methodology used (Chapter 2.3). Chapter 2.4 describes the atrium, its NVC and CF cooling systems. Chapter 2.5 presents the computational fluid dynamics (CFD) simulations performed to estimate wind-induced pressure on the atrium façades. Chapter 2.6 presents the results of the atrium NVC system performance assessment, including a thermal comfort survey. Chapter 2.7 presents the building thermal dynamic simulations. The last chapter (2.8) presents the main conclusions.

2.3. Methodology

Measuring the impact of NVC on the cooling load of a building requires an extensive experimental campaign that must include several days with similar conditions (occupancy, weather, daytime cooling system operation). The impact of NVC on the daytime cooling load can then be obtained by comparing similar days with and without NVC in the previous night. In addition to the cooling load, the measurements must include internal air temperatures, and nighttime NVC bulk airflow. To ensure that the indoor environment remains equally comfortable in both cases (with and without NVC), the experimental campaign included a thermal comfort survey. Figure 2.1 shows the four components of the methodology used in this study. There were two stages of measurement:

1. Measurement of NV bulk airflow. Bulk airflow measurement in large spaces is challenging due to the large amounts of tracer gas required to fill the large internal volume. For this reason, this study used a hybrid approach based on an initial tracer gas measurement followed by hot wire air velocity sensor measurements (described in Chapter 2.6.2).

2. Multi-day comparative CF cooling load measurements. The energy savings were obtained in multi-day comparative measurements. In these measurements indoor thermal comfort was assessed using indoor conditions and a field survey.

The simulation of the NVC system and CF cooling load required two stages shown on the right side of Figure 2.1:

3. CFD simulations of the building and its surroundings were performed to predict the static wind-induced pressure on the NVC system windows [42]. The static wind-induced pressures were then converted into pressure coefficients that are used in the calculation of the natural ventilation driving forces that occurred during the steady-state bulk airflow measurement period (Chapters 2.6.2.1 and 2.6.2.2). Pressure coefficients were also used as input in the thermal simulations for the wind-driven component of the NVC system (Chapter 2.7).

4. In the fourth stage, a dynamic thermal and airflow simulation of the atrium was performed for the multi-day comparative measurement period. This simulation model predicted the cooling load reduction, internal air temperature and bulk airflow rates for the multi-day comparative measurements, allowing for an extensive validation of the simulation tools used in this study.
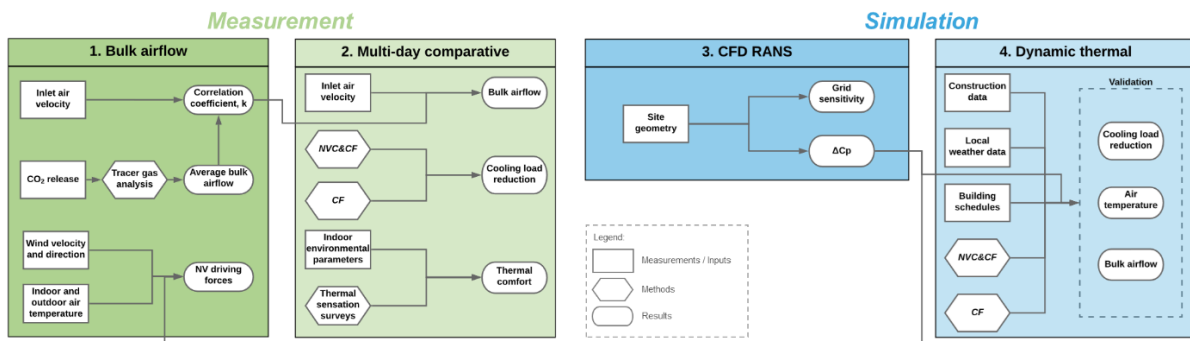
Figure 2.1 – The four components of the methodology used in this study.

2.4. Description of the atrium

The measurement campaign was performed in the Seixal City Hall (SCH) service building, shown in Figure 2.2. The building is located 5 km south of Lisbon, Portugal, a region with a mild temperate climate [43]. With a total floor area of 15000 m^2, the building is divided into two main blocks with three levels of office spaces that stand above a partially underground

floor. The two above ground office space volumes are connected by a central atrium that functions as a transitional space for visitors and a working area for city employees that provide customer services. The office spaces are mechanically conditioned by ceiling mounted fan-coil units with fresh air supplied via centralized air handling units.

Figure 2.2 – Aerial image (left), exterior view of the openable windows located at the west façade (center) and internal view of the atrium (right).

This study focused on the cooling load and NVC system performance of the large volume atrium space (~16200 m^3). The atrium is mechanically cooled by a CF system (fed by heat pumps). The CF system is on during the daytime (from 07:30 to 20:00) whenever the average occupied zone air temperature exceeds the cooling setpoint of 24 ºC. During mid-season and summer, the mechanical cooling system is supported by an NVC system that uses openable windows in opposite façades of the atrium at different heights. The NV system was designed to guarantee that the prevailing winds from west assist the stack effect, maximizing natural airflow. The wind and stack driven NV system is only used during the night for night cooling (NVC). Due to the large volume of the atrium and the constant use of the outdoor entrance, the space does not require mechanical or natural ventilation during daytime to maintain adequate indoor air quality, relying solely on infiltration.

The NVC system windows are operated by motorized actuators with two positions: closed or open at 25º (top-hung outward openings). The inlet on the west façade is composed by one row of seven openable windows at 3.1 m height. Outflow occurs at 13.8 m height on the east façade through three larger openable windows. When the NVC system is used, the windows remain open from 8 p.m. to 8 a.m.. The details of the windows used in the NVC system are shown in Table 2.1. The effective opening areas shown were calculated by adding the two triangular areas on the window sides with the rectangular area at the bottom.

Table 2.1 – NVC system window sizes.

Façade orientation	Net opening area	Number of openings	Reference height of the middle plane from the ground	Total opening effective area [m²]	A_{window}/A_{floor}
West	1.3 m x 0.95 m	7	3.1 m	9.7	0.92%
East	1.24 m x 1.45 m	3	13.8 m		

2.5. CFD simulation of external flow

The CFD simulations were performed with the commercial software ANSYS Fluent 19.2, using the steady Reynolds-averaged Navier-Stokes (RANS) equations. The standard *k*-ε turbulence model was used given its proven capacity to predict pressure coefficients on the façades of buildings [44].

2.5.1. Geometry, computational domain and grid

The SCH building is located in a suburban environment, with no significant nearby buildings in the South, West and North incoming wind directions. On the East side of the building there is a residential building block that can be seen in Figure 2.2. This building block was included in the CFD simulation geometry, as shown in Figure 2.3(a). The computational model is full scale, with 159 m width and 108 m length. The highest building in the area of interest is the SCH building with 16 m height (H_{max}). The upstream boundary of the simulation domain was set at the recommended distance from the area of interest of $5H_{max}$ [45]. The total computational domain dimensions are $59.4H_{max}$ [W] x $58.5H_{max}$ [L] x $6H_{max}$ [H] m³, preserving a directional blockage ratio of less than 17%, as recommended [46].

The computational grid has approximately 4.6 million cells. The use of tetrahedral meshes has been discouraged by CFD best practice guidelines, due to convergence problems and increased truncation error [45]. Consequently, the simulation model uses a combination of cell geometries: prismatic; polyhedral; and hexahedral cells (Figure 2.3(b)). In accordance with the current best practices for CFD simulation, this study included a grid-sensitivity analysis. Simulations were performed for eight different incoming wind directions: N, NW, NE, W, E, SW, SE, and S.
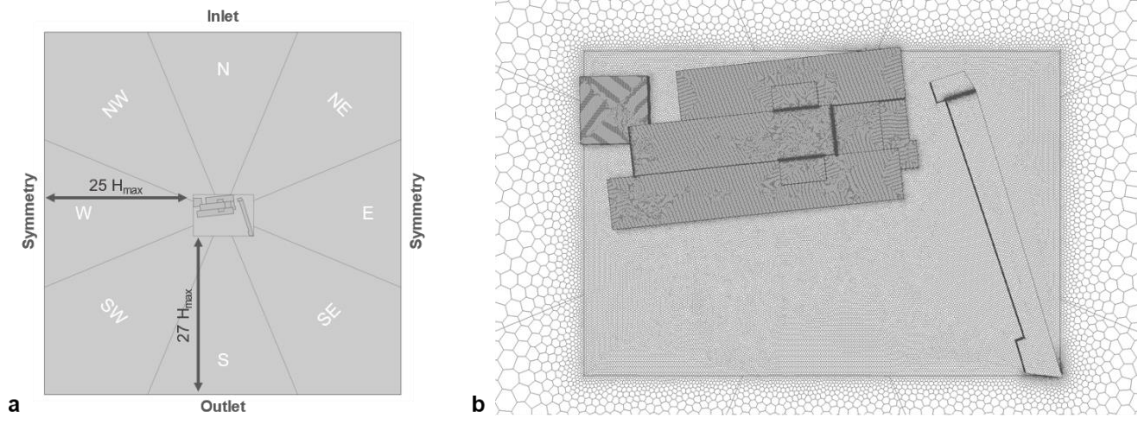
Figure 2.3 – Computational domain: a – Dimensions and the boundary conditions if the wind comes from north;
b – Mesh resolution.

2.5.2. Boundary conditions and numerical settings

The inlet boundaries, located upstream, use the inflow profiles shown in Eqs.(2.1)–(2.3) [47]. The inflow wind velocity profile follows the log-law equation (Eq.(2.1)), where U(z) is the streamwise velocity at height z (m). The aerodynamic roughness length, z_0, is set as 0.4 m, as proposed by the updated Davenport roughness classification [48]. The friction velocity (u^*_{ABL}, 1.29 m/s) was calculated using Eq.(2.1). This calculation used a reference height (z_{ref}) of 10 m, a reference wind velocity (U_{ref}) of 10 m/s and a von Kármán constant (κ) of 0.42. Depending on the wind direction, the lateral boundaries were set as a velocity inlet or a pressure outlet. The turbulent kinetic energy (k) and turbulent dissipation rate (ε) vertical profiles of the inlet are defined using Eqs.(2.2) and (2.3):

$$U(z)=\frac{u^*_{ABL}}{\kappa}\ln\left(\frac{z+z_0}{z_0}\right) \tag{2.1}$$

$$k(z)=\frac{\left(u^*_{ABL}\right)^2}{\sqrt{C_\mu}} \tag{2.2}$$

$$\varepsilon(z)=\frac{\left(u^*_{ABL}\right)^3}{\kappa(z+z_0)} \tag{2.3}$$

13

Cμ is a turbulence model constant with a value of 0.09. The downstream boundaries were set as outlets with a static zero pressure condition set. The top boundary is a symmetry plane with a zero normal velocity condition and zero normal gradients to the remaining flow variables. The ground surface, and the walls of the buildings have a zero sand-grain roughness height set (k_s = 0 m). The SIMPLE solver was set to pressure-velocity coupling scheme, solving the momentum and pressure-based continuity equations separately. The convection, pressure, turbulent kinetic energy, and turbulent dissipation rate terms use second order discretization schemes. The pressure at the inlet and outlet were monitored during each simulation. Once the pressure values stabilized over hundreds of iterations the simulations were stopped. The final net mass imbalance of the simulations had an order of magnitude of 10^{-10}. The residuals were 10^{-6} for continuity and ε, 10^{-7} for k, and 10^{-8} for each velocity component.

2.5.3. Grid sensitivity analysis

A grid sensitivity analysis was performed to assess grid resolution impact on the pressure difference between inlet and outlet, Δp. As shown in Figure 2.4, this pressure difference varied between 5 Pa and 8 Pa when using grids with 450-thousand cells and 3.5 million cells. The predicted pressure difference stabilized after the grid refinement to 4.6 million cells, consequently, this grid was used for the remaining CFD simulations [49].
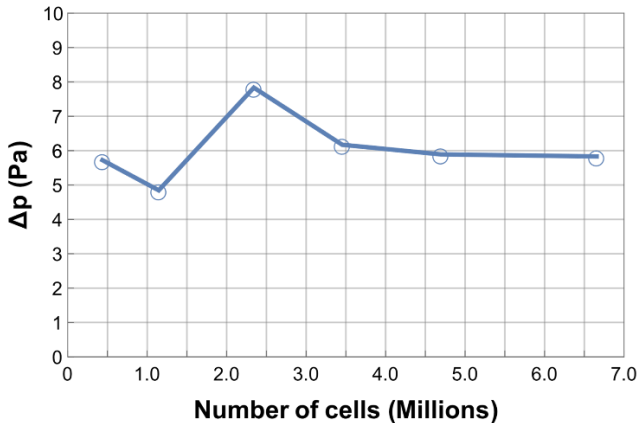
Figure 2.4 – Pressure results from different grid resolutions.

14

2.5.4. CFD simulation results

The simulated static pressures in the openings of the NVC system were converted into pressure coefficients using Eq.(2.4), where P_{local} is the local wind driven static pressure (Pa), ρ is the air density (kg/m^3), and U_{ref} is the reference wind speed at 10 m height (m/s). The pressure coefficient is defined as a relation between the static and the dynamic pressures (see Eq.(2.4)), that is constant at any given point in the domain. The pressure coefficient difference, ΔC_p, shown in Table 2.2, results from the difference between the pressure coefficient of the inlet and outlet.

$$C_p = \frac{P_{local}}{\frac{1}{2} \cdot \rho \cdot U_{ref}^2} \tag{2.4}$$

Table 2.2 – Pressure coefficients at inlet, outlet and difference between both.

	N	NW	W	SW	S	SE	E	NE
Cp_{in}	-0.45	0.04	0.55	0.25	-0.17	-0.34	-0.14	-0.28
Cp_{out}	-0.55	-0.41	-0.24	-0.45	-0.50	0.10	0.24	0.42
ΔCp	0.10	0.45	0.79	0.70	0.33	-0.44	-0.38	-0.70

2.6. Measurements

2.6.1. Measurement setup

The measurement setup monitored the interior conditions of the atrium, cooling load, bulk airflow, and local weather. The atrium measurements used 9 combined air temperature and CO_2 concentration (TCD) sensors and 2 hot-wire anemometers (HWA). Figure 2.5 shows the sensor locations in the atrium: a column with 4 TCD sensors positioned at different heights (1.5 m, 3 m, 5 m and 11 m) was installed in the middle of the atrium to measure the stratification; 3 TCD sensors monitored the occupied zone at 0.6 m; 2 more TCD sensors measured the air conditions at the inlet and outlet; and the 2 HWA sensors measured the air velocity at the inlets. To avoid radiation effects on the measurements of the air temperatures the sensors were shielded and mechanically ventilated using small extract fans (4 cm in diameter).

A local weather station was installed in an open field located west of the building site (exposed to the predominant wind direction and avoiding interference from adjacent buildings). The

weather station measured air temperature, relative humidity, wind velocity and direction, as well as global and diffuse solar radiation. The specifications of the equipment used are shown in Table 2.3.
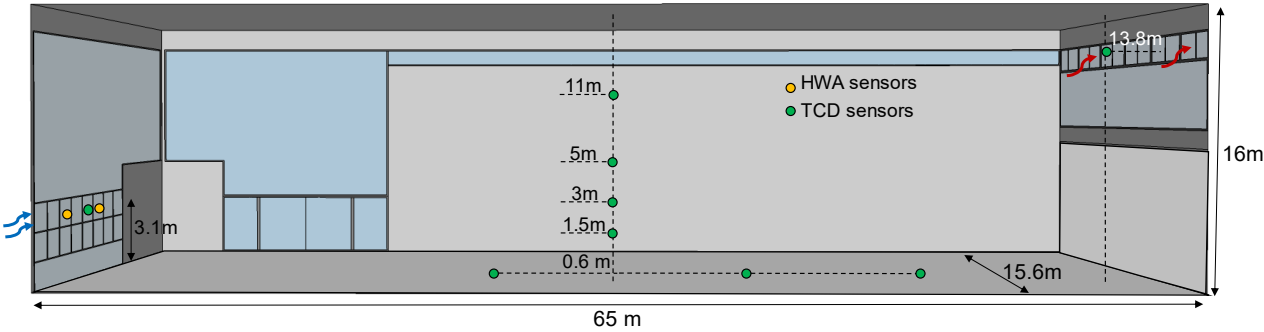
Figure 2.5 – Distribution of TCD and HWA sensors within the atrium.

Table 2.3 – Specification of the measurement equipment used.

Sensor	Measurement	Specification	
Anemometer Wind Monitor 05103 Campbell Scientific	Wind speed (outdoor)	Range	$0 - 100$ [m/s]
		Accuracy	± 0.3[m/s] or 1% reading
	Wind Direction (outdoor)	Range	$0 - 360°$
		Accuracy	$\pm 3°$
Pyranometer SPN1, Delta-T Devices	Solar radiation (global and diffuse)	Range	$1 - 2000$ [W/m^2]
		Accuracy	$\pm 5\%, \pm 10$ [W/m^2]
HOBO (U12-013) & Telaire 7001	Temperature (outdoor)	Range	$-20.0 - 70.0$ [ºC]
		Accuracy	± 0.35 [ºC] from $0 - 50.0$ [ºC]
	Relative humidity (outdoor)	Range	$5\% - 95\%$
		Accuracy	$\pm 2.5\%$ from $10 - 90\%$
	Carbon dioxide (outdoor)	Range	$0 - 2500$ [ppm]
		Accuracy	$5\% \pm 50$ [ppm]
Hot-wire anemometer E+E elektronik EE65	Air velocity (indoor)	Range	$0 - 10$ [m/s]
		Accuracy	± 0.2 [m/s], $+ 3\%$
CO$_2$ Meter (K-33 ELG)	Temperature (indoor)	Range	$-40 - 60$ [°C]
		Accuracy	± 0.4 [°C] at 25 [°C]
	Carbon dioxide concentration (indoor)	Range	$0 - 10000$ [ppm]
		Accuracy	± 30 [ppm], $+ 3\%$

2.6.2. Bulk NVC airflow measurement

The bulk airflow measurement aims to determine the relation between inlet air velocity and the bulk airflow rate of the NVC system. This correlation will be used to measure the bulk NVC airflow during the multi-day measurements using only the easily measurable inlet air velocities (discussed in Chapter 2.6.3).

The tracer gas measurement was performed in an evening period of 3.5 h (with no occupancy). The tracer gas bulk airflow measurement technique consists of injecting a pollutant (tracer) gas

into the space, achieving a uniform pollutant concentration, and monitoring the pollutant decay over time to infer the bulk airflow rate. In large rooms, it can be difficult to reach adequate mixing of the tracer gas [50]. Large space rooms require a high number of sensors, large quantities of traceable gas and long measurement periods.

In this study, carbon dioxide (CO_2) is used as a tracer gas. Two tracer gas methods, constant release and concentration decay are used with the measurement setup described in Chapter 2.6.1. CO_2 was injected in front of the inflow windows in two points (3.1 m height, near the HWA positions, indoor).

2.6.2.1. Tracer gas methods

The first tracer method used is constant release of 1.57 mg/s of CO_2 traceable gas into the atrium during two hours and fifty-five minutes. After the initial mixing period, steady-state conditions were achieved, and the bulk airflow rate can be calculated using simple tracer gas mass balance equation (Eq.(2.5)) [51]:

$$F = \frac{\dot{m}_{released}}{C_{outlet} - C_{inlet}} \tag{2.5}$$

where F is the bulk volume flow rate [m³/s], $\dot{m}_{released}$ is the constant CO_2 flow rate [mg/s] released during the experiment, C_{outlet} and C_{inlet} are the CO_2 concentration levels [mg/m³] measured at the outlet and inlet, respectively. In the end of the stabilized phase, after the CO_2 injection period, a second transient method is used to calculate the bulk airflow rate from the natural decay of the CO_2 concentration, known as decay method. From the time variation of the CO_2 concentration during the decay, the bulk airflow is calculated using Eq.(2.6) [52]:

$$F = \frac{(\sum_{j=1}^{n} t_j) \cdot \sum_{j=1}^{n} \ln(C(t_j) - C_{bg}) - n \cdot \sum_{j=1}^{n} t_j \cdot \ln(C(t_j) - C_{bg})}{n \cdot \sum_{j=1}^{n} t_j^2 - (\sum_{j=1}^{n} t_j)^2} \times \frac{V_{atrium}}{3600} \tag{2.6}$$

where F is the bulk volume flow rate [m³/s], t_j is the elapsed time since the initial time of the decay curve [h] and $C(t_j)$ the CO_2 concentration at that time [mg/m³], n is the total number of

measured points during the decay process (=47), C_{bg} is the background CO_2 concentration [mg/m^3], and V_{atrium} is the volume of the atrium [m^3].

Equations (2.5) and (2.6) evaluate the bulk airflow rate at different periods of the same measurement. For steady-state external conditions, both equations will predict the same flow. Using two methods increases the confidence in the measured bulk airflow rate.

To verify that, during the airflow measurements, an approximately steady-state external driving force conditions exist, the total pressure of the NVC system must be analyzed. Natural ventilation is driven by pressure differences that can be generated by wind or buoyancy, or a combination of both. The pressure induced by wind (ΔP_w) and buoyancy (ΔP_b) are defined by Eqs.(2.7)-(2.8), respectively. Further, the combined effect (ΔP_{tot}) can be calculated according with Eq.(2.9).

$$\Delta P_w = \frac{1}{2} \cdot \Delta C_p \cdot \rho \cdot U_{ref}^2 \tag{2.7}$$

$$\Delta P_b = \rho \cdot g \cdot (H_{outlet} - H_{inlet}) \cdot \left(\frac{T_{vertical\ mean} - T_{outside}}{T_{outside}} \right) \tag{2.8}$$

$$\Delta P_{tot} = \sqrt{\Delta P_w^2 + \Delta P_b^2} \tag{2.9}$$

where ΔC_p is the difference between the pressure coefficients at the inlet and the outlet (see Table 2.2), ρ is the density of the air [kg/m^3], g is the gravity of Earth [m/s^2], H_{outlet} and H_{inlet} are the height of the outlet and inlet [m], respectively. $T_{vertical\ mean}$ is the mean indoor air temperature from the TCD sensors in the vertical column at the middle of the atrium (cf. Chapter 2.6.1) and $T_{outside}$ is the outdoor air temperature [K].

2.6.2.2. Bulk airflow results

Figure 2.6(a) shows the measured wind direction and its magnitude, and the pressure generated by wind obtained according to the pressure coefficients predicted by the CFD simulations (cf. Chapter 2.5.4). During the measurements, the prevailing wind direction was from west and north-west orientation and the wind speed decreased progressively over the experiment, as well as the wind-induced pressure. The difference between indoor and outdoor temperature increased, resulting in a higher buoyant-induced pressure, as shown in Figure 2.6(b). This figure also shows that, as expected in light of the absence of internal gains, there is minimal stratification in the space: less than 0.8K difference between 1.5 m and 11 m heights. Comparing the induced pressure in both figures, it can be seen that wind effect is the main driving force for the first half of the measurement period, whilst for the second half, the airflow is mainly driven by buoyant forces.
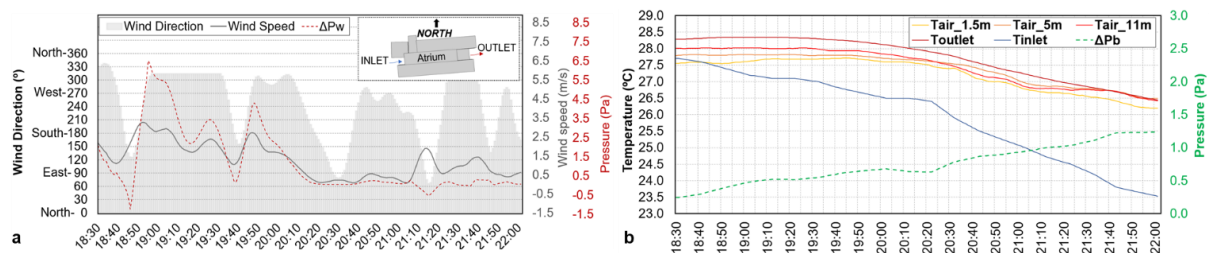
Figure 2.6 – Measurement of the natural airflow performance of the atrium NVC system: a) Wind speed and direction, pressure generated by the wind during the experiment; b) temperature distribution during the experiment and buoyant-induced pressure.

Figure 2.7 shows the measured interior average CO_2 concentration, the total pressure induced by the NVC driving forces, and the average inlet air velocity during the intra-day experiment. It is possible to identify three sequential phases in the variation of the CO_2 concentration profile:

1. The mixing phase is characterized by a high fluctuation of the total pressure variation and a progressive increase of the CO_2 concentration indoors (high wind effect). This unstable phase lasts for around one hour and forty-five minutes until a concentration of CO_2 at around 740 ppm is reached.

2. The stabilization phase where it is possible to identify quasi-steady conditions for CO_2 concentration and total flow driving static pressure over one hour and ten minutes. In this period, it is possible to calculate the average bulk airflow rate. Using Eq.(2.5), a bulk airflow rate of 2.9 m³/s was obtained.

3. The decay phase begins once the CO_2 release ceases, triggering a decay that lasted approximately 35 minutes. Since the total pressure variation is constant during this phase, is possible to calculate the bulk airflow rate using Eq.(2.6), obtaining a bulk airflow rate of 2.7 m^3/s.

In both methods, $CO_{2,\,inlet}$ and C_{bg} are assumed equal to the measured outdoor CO_2 concentration ($\approx$ 400 ppm). The difference between the bulk airflow rate measured by both methods is 0.2 m^3/s, corresponding to a deviation of 7%, revealing the consistency and accuracy of the methods used.
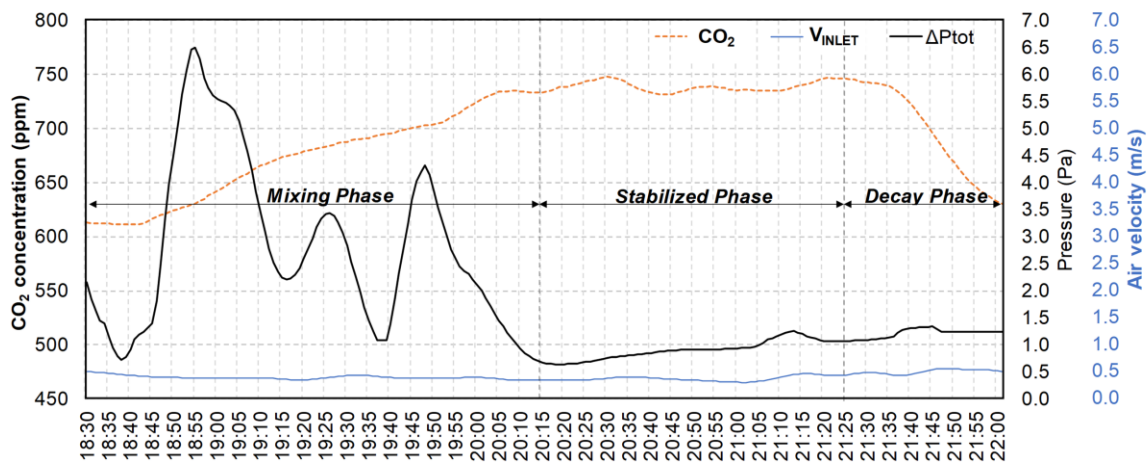
Figure 2.7 – Measured profiles during the short-term experiment (interior average CO_2 concentration, total pressure variation and average inlet air velocity) and its division in three different phases.

2.6.2.3. *Determining correlation coefficient, k*

With the goal of simplifying the measurement of the bulk airflow rate during the multi-day comparative campaign (see next chapter), the intraday results were used to calculate the relation between the average measured air velocity at the inlets (HWA sensors, $\bar{v}_{air\_in}$, 0.40 m/s) and the average bulk flow rate. The bulk airflow rate used to define this linear relation was the average of the measured bulk airflow rates using the constant release and decay methods ($\bar{F}$ = 2.8 m^3/s). The correlation coefficient, k, was obtained using the following expression:

$$k = \frac{\bar{F}}{\bar{v}_{air\_in}} = 7.0 \qquad (2.10)$$

21

2.6.3. Multi-day comparative measurement

Field studies of building energy consumption and indoor environment monitoring are difficult to implement and, in the case of NV or hybrid cooling systems, setting up an adequate comparative measurement scenario can be very challenging. An ideal setup to display the energy saving capabilities of NV requires two identical buildings with similar occupancy and internal gains, allowing for a direct comparison of NV and mechanical cooling solutions. These experiments are difficult since the indoor conditions in both buildings must be comparable and similarly comfortable (possibly relying on different thermal comfort standards for mechanically cooled and naturally ventilated environments). Alternatively, the experiments can be performed on a single building by comparing cooling load for two similar days or intra-day periods using NV or mechanical cooling exclusively. This study used a simpler version of this procedure to assess the impact of NVC on mechanical cooling load in the next day: comparing daytime cooling demand in similar days, with and without NVC in the previous night.

The multi-day measurement campaign used in this study is composed of 23 days of detailed monitoring of the atrium (from the 6th to 28th July of 2017). The measurements include two cooling modes: CF (chilled floor system); and NVC&CF (natural nighttime ventilative cooling and chilled floor system). The measurement setup was identical to the one presented in Chapter 2.6.1. Data was acquired with a timestep of 5 minutes, and the number of occupants of the atrium, including the total number of visitors and employees. The CF cooling load was measured by monitoring the supply ($T_{w,s}$) and return ($T_{w,r}$) water temperatures, using two thermocouples in the supply and return chilled water pipes. The CF system operates with a constant water flow of 7.2 kg/s ($\dot{m}_w$). The daily cooling load of the CF system is then obtained from:

$$Q_{cool} = \dot{m}_w . Cp_w . \frac{1}{12} . \sum_{n=1}^{149} \left(T_{w,r} - T_{w,s} \right) \qquad (2.11)$$

where Q_{cool} is the daily cooling load of the CF system [kWh], Cp_w is the specific heat capacity of water (= 4.19 kJ/kg.K), and $T_{w,s}$ and $T_{w,r}$ are the supply and return water temperatures [K]. To compare the CF and NVC&CF cooling modes, sets of two days were chosen based on having similar values of the following variables:

- Maximum and mean outdoor air temperature.
- Maximum and mean indoor temperature.
- Mean horizontal solar radiation.

Table 2.4 shows the two groups of comparable days that were identified: mild summer days (1-2 and 15-16 days) and hot summer days (days 20 to 23). Figure 2.8 shows the weather data of the measuring period and the days that will be compared, and the cooling systems used in these days.

Table 2.4 – Analyzed weather data of comparable days between cooling modes: NVC&CF and CF.

Mode	Day	Max. T_{ext} [ºC]	Avg. T_{ext} [ºC]	Avg. T_{ext} [ºC] (8 a.m. -7 p.m.)	Avg. Atrium temp. [ºC]	Max. Atrium temp. [ºC]	Avg. Horizontal Rad. [W/m²] (8 a.m. -7 p.m.)
NVC&CF	1	27.0	21.9	24.1	23.1	25.9	649
	2	27.4	22.7	25.3	23.5	26.1	
CF	15	25.8	21.4	23.4	23.9	25.9	694
	16	26.6	21.4	24.1	24.0	26.5	
NVC&CF	20	34.2	25.2	29.4	24.2	27.3	725
	21	34.3	26.8	30.6	24.5	27.5	
CF	22	31.9	24.7	28.0	24.5	27.8	747
	23	34.6	26.0	30.2	24.6	28.1	
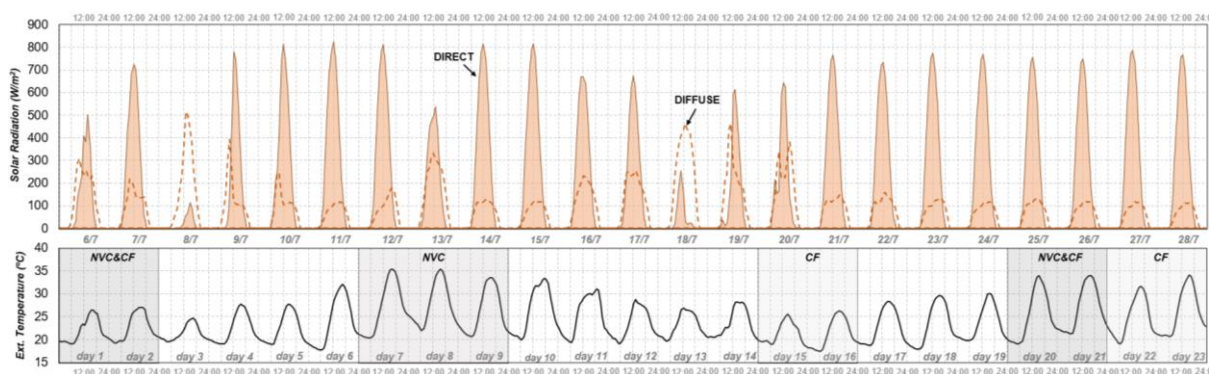
Figure 2.8 – Weather data during the measuring period and the selected days to be compared.

2.6.3.1. *Energy savings due to NVC*

Figure 2.9 shows the measured cooling load in mild and hot summer days. The results obtained revealed significant cooling load reduction when night ventilation (NVC&CF) is used. In mild summer days, the NVC&CF had a total cooling load of 477 kWh_t, representing a 32% cooling load reduction (compared with CF operation without NVC). For hot summer days, the total cooling load of the NVC&CF scenario was 818 kWh_t (24% less than the cooling load of CF without NVC).

Even with significant energy savings when night cooling (NVC&CF) is used, it can also be observed that the chosen NVC&CF days have a higher average outdoor air temperature than the CF days, which makes this magnitude of savings a conservative number.

The cooling load is proportional to the average outdoor air temperature for 7 out of 8 days analyzed. Day 23 is the only case when this does not occur. Wind speed may be the factor that explains the decrease in cooling load between days 22 and 23. Even with higher air temperatures on day 23, the average wind speed is 40% lower than on day 22. Wind speed directly affects the air exchange with the interior of the atrium through the envelope.
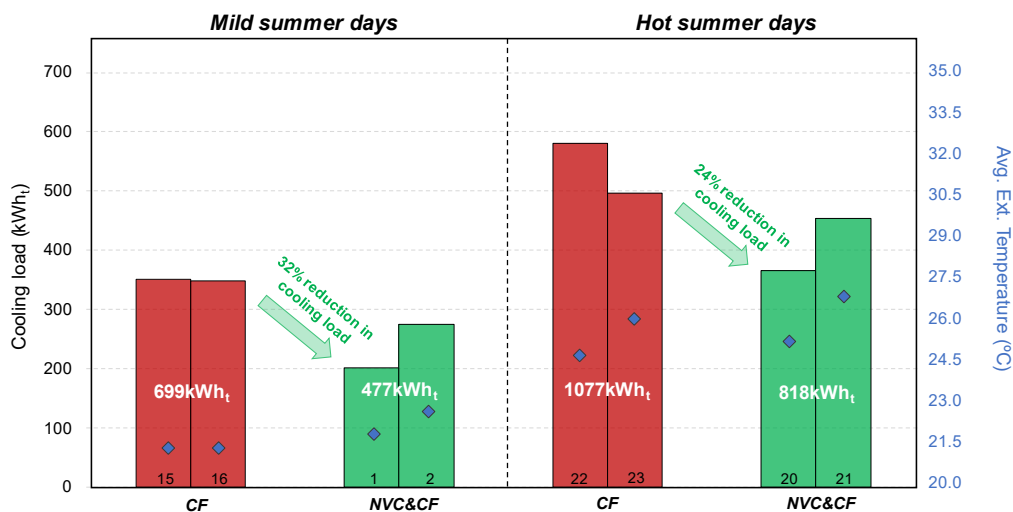
Figure 2.9 – Cooling load comparison between NVC&CF and CF modes over comparable days.

24

2.6.3.2. Thermal comfort assessment

The experimental campaign included a thermal comfort survey to confirm that NVC use did not affect occupant thermal comfort. In particular, this analysis ensured that the NVC system did not create overcooling in the first hours of the morning, a common problem in NVC systems.

The thermal comfort assessment used a voluntary questionnaire for atrium occupants. During each questionnaire, a mobile environment-monitoring cart (MEMO) [53] was used to measure indoor environmental parameters near the occupant. A total of 30 questionnaires in each day were filled by occupants (details about the questionnaire can be found in [53]). The MEMO system measured environmental parameters at 0.6 m height (abdomen level for a seated person): air temperature; operative temperature; air velocity; and relative humidity. Table 2.5 shows the specifications of the sensors used. The accuracy of the sensors meets the recommendations of the European standard EN ISO 7726 [54]. The radiative temperature was measured using a 40 mm globe thermometer (painted in grey inside and black on the outside) [54, 55, 56]. Each sensor had a sampling interval of 10 seconds. The questionnaires evaluated the perception of the thermal environment by the occupants in terms of thermal sensation, preference, and comfort.

Thermal comfort was also assessed in a purely passive cooling mode NVC, thereby confirming the need to use the CF during the day. The measurements and questionnaires were performed in NVC&CF and NVC modes, days 21 and 9, respectively (cf. Figure 2.8).

Table 2.5 – Specification of the sensors used in MEMO to monitor indoor environmental parameters.

Sensor	Measurement	Specification	
Tersid Pt100 class A	Air temperature (T_{air})	Range	-50 — 150 [°C]
		Accuracy	$\pm$ 0.2 [°C] from -25 — 74.9 [°C]
Tersid Pt100 class A	Mean radiant temperature (T_{mr})	Range	-50 — 150 [°C]
		Accuracy	$\pm$ 0.2 [°C] from -25 — 74.9 [°C]
Anemometer Sensor electronics SensoAnemo 5130LSF	Air speed (V_{air})	Range	0.05 — 5.0 [m/s]
		Accuracy	0.02 [m/s], +1.5% reading
EE08 series HC101 sensor	Relative humidity, RH [%]	Range	0 — 100%
		Accuracy	$\pm$ 2% from 0 — 90% $\pm$ 3% from 90 — 100%

Table 2.6 shows the weather conditions of the days 9 and 21. Table 2.7 shows the clothing levels and number of users in each survey.

Table 2.6 – Analyzed weather data of comparable days between cooling modes: NVC&CF and NVC.

Mode	Day	Max. T_{ext} [ºC]	Avg. T_{ext} [ºC]	Avg. T_{ext} [ºC] (8a.m. -7p.m.)	Avg. Atrium temp. [ºC]	Max. Atrium temp. [ºC]	Avg. Horizontal Rad. [W/m²] (8a.m. -7p.m.)
NVC&CF	21	34.3	26.8	30.6	24.5	27.5	725
NVC	9	33.8	26.3	30.0	25.1	29.1	664

Table 2.7 – Indoor environmental parameters, clothing level and statistics of the sample.

Modes		Indoor			Clothing	Number of Users		
		T_{op} [ºC]	V_{air} [m/s]	RH [%]	Clo	Female	Male	Total
NVC&CF	Mean	24.1	0.11	60	0.60	17	13	30
	St.dv	0.2	0.09	1	0.11			
NVC	Mean	25.0	0.10	58	0.59	17	13	30
	St.dv	0.2	0.08	1	0.13			

The thermal sensation votes (TSV) were divided in the following subcategories:

- TSV (-1, 0, 1): occupants are satisfied with the thermal environment;
- TSV (-3, -2): occupants are dissatisfied due to cold environment;
- TSV (+3, +2): occupants are dissatisfied due to warm environment.

Analysis of the thermal sensation and thermal preference results, shown in Figure 2.10, reveal small but relevant differences between the cooling modes tested. All the interviewed reported being comfortable in the cooling mode NVC&CF, while in the NVC only cooling mode, 13% of the interviewed reported a thermal sensation towards warm (+3, +2). The thermal preference vote in both modes shows that the majority of the occupants (87% in NVC&CF and 67% in NVC) felt comfortable and preferred no changes in the thermal environment. As expected, in NVC&CF mode, 3 people preferred a cooler environment, while in NVC mode there were 9 occupants with this preference.
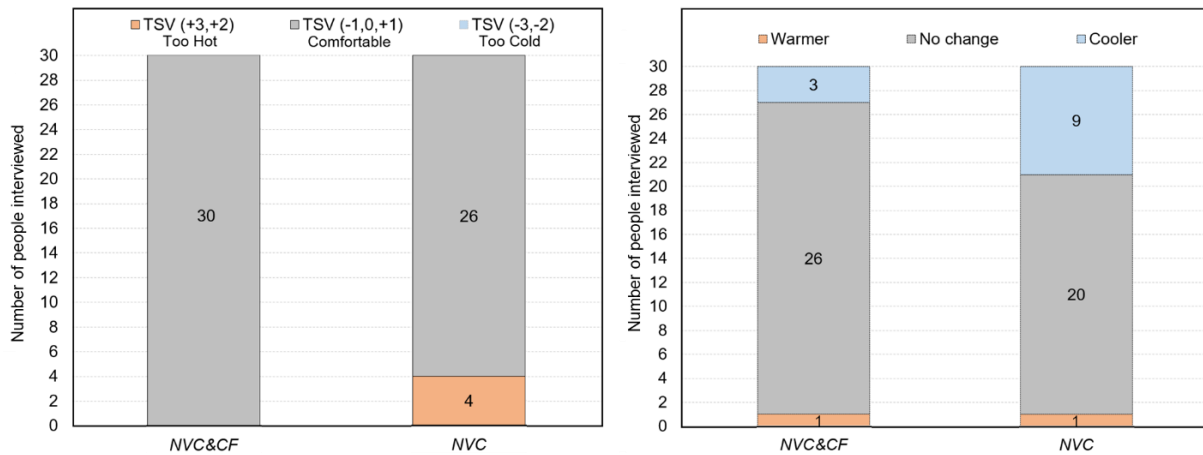
Figure 2.10 – Distribution of thermal sensation (left) and thermal preference (right).

The distribution of thermal comfort votes, shown in Figure 2.11, revealed that both cooling modes achieved the minimum threshold of 80% for people that was comfortable [57]. Further, under the NVC&CF cooling mode 93% of the occupants were comfortable, whereas under the NVC cooling mode the percentage fells to 84%.

Considering the thermal comfort results, the NVC&CF mode shows an increment in the thermal comfort perception by the occupants when compared with the NVC cooling mode. Although both systems may be considered as thermally comfortable to most of the occupants of the atrium, the NVC cooling mode alone revealed that 30% of the occupants would prefer a cooler environment, which exposes its cooling limitations over the warmer periods of the summer.
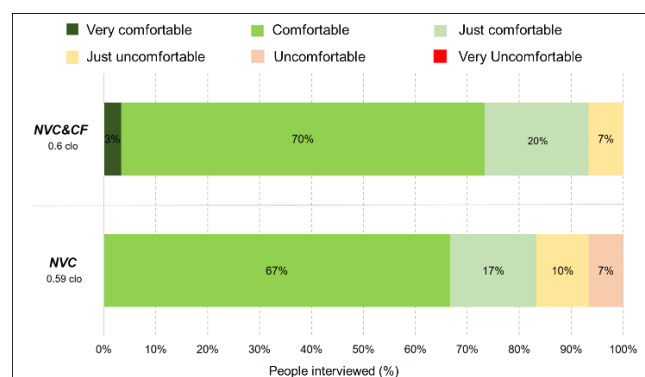
Figure 2.11 – Distribution of thermal comfort votes under NVC&CF and NVC modes.

27

2.7. EnergyPlus simulations

Dynamic thermal simulations were performed in EnergyPlus (version 8.7.0, [58, 59]). This open source thermal simulation code is developed by the United States Department of Energy, has the capability to model NV [60, 61] and HVAC systems [62, 63]. There are only a limited number of EnergyPlus validation studies in mixed-mode spaces such as the atrium of the SCH building. To simulate the atrium mixed cooling system required a combination between a detailed HVAC system with a CF system and an airflow network [59] model of the NVC system. The airflow network model uses the wind driven pressure coefficients shown in chapter 4.4. A discharge coefficient of 0.6 was used for the atrium windows [64]. Internal convection was simulated using the TARP algorithm [65].

The atrium boundary conditions were defined using five thermal zones (shown in Figure 2.12): two office blocks (north and south oriented), the auditorium, the cafeteria, and an underground parking lot. With the exception of the atrium, the HVAC system of the other zones was modelled using the EnergyPlus template for a unitary system with the daytime temperature setpoint that is used in these spaces (23 ºC). The atrium façade has double glazed windows with a low-emissivity coating with a U-value of 1.5 W/m^2.K. The CF system was incorporated in the atrium floor (from outside to inside): a 20 cm thick concrete outside layer; 5 cm of expanded polystyrene; 6 cm of concrete; CF system; and 6 cm of concrete. The occupancy profile used was defined accordingly with the information collected by the central system of the building, ranging between 28 and 101 people during the working hours. The internal gains due to electric equipment were divided into permanent and variable gains. The permanent gains were related to equipment that was always turned on, while the variable gains referred to office equipment only used during working hours. The permanent and variable gains were 1.3 W/m^2 and 1.1 W/m^2, respectively. The lighting system of the atrium was only used on weekdays between 21:00 and 22:30 for cleaning purposes with a consumption of 7 W/m^2. The run period of each simulated case equals the measurement periods shown in Figure 2.8. The measurements of the weather station, located close to the SCH building, were incorporated in the weather file used in the simulations.
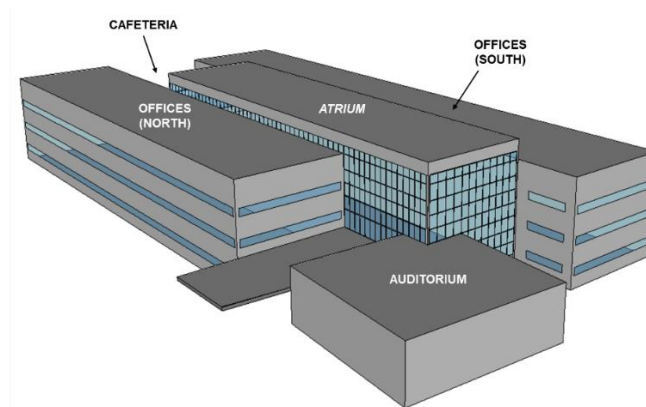
Figure 2.12 – Thermal zones considered in the EnergyPlus model.

2.7.1. Validation

The results of the multi-day measurements were used to validate the thermal simulation model for the two cooling modes (CF and NVC&CF). The validation focused on three variables: cooling load, air temperature in the atrium and bulk NVC airflow.

Figure 2.13 and Figure 2.14 show the measured and simulated results for the atrium average air temperatures, cooling load and bulk airflow. The upper half of each graph in Figure 2.13(a)–(d) shows the average air temperature inside the atrium, while the lower half shows the instantaneous cooling power demand and the total cooling load per day. The results show good agreement between the simulations and experiments. In the temperature predictions, the results display consistent overpredictions during the peak of solar radiation (14h-16h), and underprediction when the direct solar gains flow into the space from the fully glazed west façade (18h-20h). The cooling load is well predicted during most days, however, the simulations show that the CF system is required slightly earlier on the mild summer days, due to temperature overpredictions at night that causes the temperature to reach the cooling setpoint sooner in the morning. Although the simulated NV bulk airflow shows some discrepancies during the day, the total bulk NVC airflow is very similar to the measured one (see Figure 2.14).
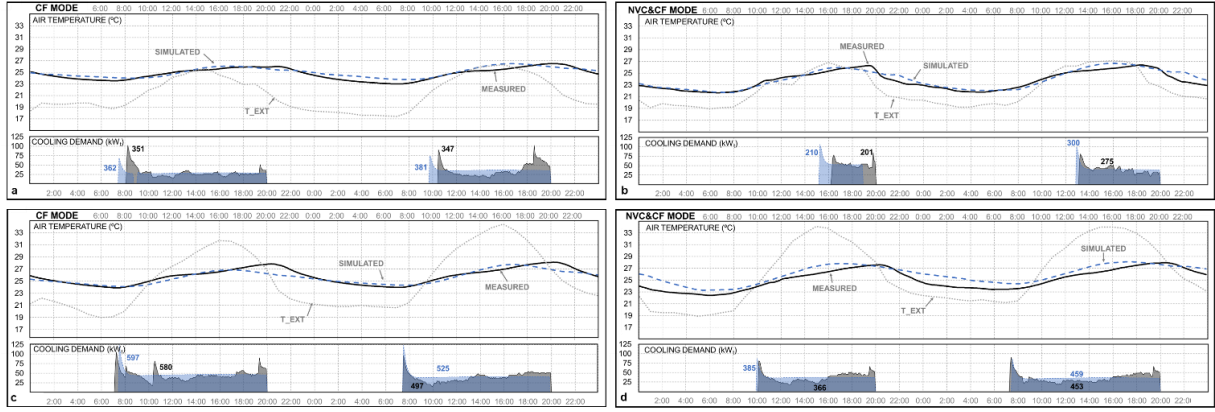
Figure 2.13 – EnergyPlus validation results for the atrium average air temperature and cooling power demand during mild summer days (a and b) and hot summer days (c and d).
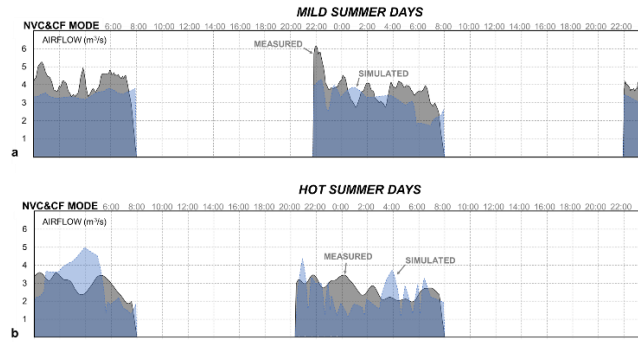
Figure 2.14 – EnergyPlus validation results for the bulk airflow rate when NVC&CF cooling mode was used during: a) – mild summer days; b) – hot summer days.

The precision of the thermal simulation model was quantified using the following error indicators:

$$\text{Avg. Dif. } [kW_t; K; m^3/s] = \frac{\sum_{i=1}^{n} |Sim._i - Meas._i|}{n} \tag{2.12}$$

$$\text{Avg. Bias } [kW_t; K; m^3/s] = \frac{\sum_{i=1}^{n} Sim._i - Meas._i}{n} \tag{2.13}$$

$$\text{Avg. Error } [\%] = \frac{100\%}{n} \times \sum_{i=1}^{n} \left| \frac{Sim._i - Meas._i}{Meas._{Max.} - Meas._{Min.}} \right| \tag{2.14}$$

where Avg. Dif. is the average difference, Avg. Bias is the average bias and Avg. Error is the average percentage error. The percentage error is calculated by normalizing the difference between measurement and simulated using the total variation during the measurement period (see Eq.(2.14)):

For air temperature i stands for each timestep of the thermal simulation (five minutes). For bulk airflow and cooling demand i indexes the measurement day. The results of the EnergyPlus simulation validation are presented in Table 2.8. The predicted indoor mean air temperature has a good agreement with the measurements, with an average error and bias of 11.2% and 0.28 K, respectively. The predicted daily bulk NVC airflow has the highest average error (14.1%). This may be partially due to uncertainties in using the correlation coefficient, k, to infer the bulk airflow during the multi-day comparative measurements. The overall agreement with the daily cooling demand is very good, with the average error being less than 6% and a bias of 18.6 kW$_t$.

Table 2.8 – EnergyPlus validation results: average error, average difference, and average bias.

Mode	Temperature			Bulk airflow			Cooling demand		
	Avg. Error [%]	Avg. Difference [K]	Avg. Bias [K]	Avg. Error [%]	Avg. Difference [m³/s]	Avg. Bias [m³/s]	Avg. Error [%]	Avg. Difference [kW$_t$]	Avg. Bias [kW$_t$]
CF	11.1	0.42	0.03	-	-	-	5.3	22.4	22.4
NVC&CF	11.2	0.65	0.52	14.1	0.48	-0.31	5.0	14.8	14.8
Average	**11.2**	**0.54**	**0.28**	**14.1**	**0.48**	**-0.31**	**5.2**	**18.6**	**18.6**

A daily comparison between the measured and predicted cooling load reduction is shown in Table 2.9. Both the daily and the average energy savings are well predicted by the thermal simulations (average error is below 2%).

Table 2.9 – Comparison of the measured and simulated cooling load reduction.

Cooling demand		Mild summer days		Hot summer days		Average savings (%)
		Day 1 [kWh]	Day 2 [kWh]	Day 3 [kWh]	Day 4 [kWh]	
Simulated	CF	362	381	597	525	
	NVC&CF	210	300	385	459	28
	Savings	**42%**	**21%**	**35%**	**13%**	
Measured	CF	351	347	580	497	
	NVC&CF	201	275	366	453	27
	Savings	**43%**	**21%**	**37%**	**9%**	

2.8. Conclusions

This chapter presented the first measurement of cooling load reduction due to NVC in a service building. The measurements were performed in an NVC system that is installed in a large atrium of a building that is exposed to a warm climate. The NVC system is driven by a combination of stack and wind. In addition, it was performed a CFD study of the wind-induced pressure on the NV openings of the atrium, and an EnergyPlus dynamic thermal simulation of cooling load, space air temperature and bulk NVC airflow. Using this measured data, it was performed the first field data-based validation of thermal, HVAC cooling load, and airflow simulation tools that designers use to size and study the viability of NVC systems.

The results confirmed that night cooling by natural ventilation could provide a measurable reduction in cooling energy demand of service buildings with exposed internal mass. Comparison of the measured daytime cooling load of days with similar weather and variable use of the NVC system in the previous night (on or off) shows that the NVC system reduces the CF cooling load by 27%. This reduction is similar to a previous study focusing on residential buildings with NVC. A survey of the thermal comfort of the atrium users showed that this NVC system did not create overcooling in the first hours of the morning (a common problem in these systems). The combination of two simulation tools used in this chapter can predict the cooling load reduction, internal air temperatures and bulk NVC airflow rates with average errors of 1.7%, 11.2% and 14.1%, respectively.

3. SINGLE SIDED VENTILATION

3.1. Nomenclature

Symbols

α power law coefficient [-]

β incident angle of the local wind (parallel to façade) [º]

γ tilt angle of the window [º]

θ incident angle of the reference wind (parallel to ground) [º]

ρ air density [-]

$\Delta C_{p_{op}}$ maximum pressure coefficient difference across the opening [-]

Δp pressure difference [Pa]

Δp_b buoyancy pressure [Pa]

Δp_f fluctuation pressure [Pa]

ΔT temperature difference between interior and exterior [ºC]

ΔT^* ratio of ΔT_{eff} and ΔT [-]

ΔT_{eff} effective temperature difference at the opening [ºC]

a base correction coefficient [-]

A_{eff} effective opening area [m^2]

A_f façade area [m^2]

A_{op} opening area [m^2]

Ar Archimedes number [-]

b exponent correction coefficient [-]

$C(t_j)$ CO_2 concentration at time, t_j [mg/m^3]

C_{bg} background CO_2 concentration [mg/m^3]

C_d discharge coefficient [-]

C_p pressure coefficient [-]

$\overline{C}_{room}$ average CO_2 concentration [mg/m³]

CF   correlation coefficient factor [-]

D   depth of the room [m]

F_{LB} bulk flow number (based on the local wind velocity, U_L) [-]

F_{LE} effective flow number (based on the local wind velocity, U_L) [-]

F_{LE}^{*} normalized effective flow number (based on the local wind velocity, U_L) [-]

F_{RE} effective flow number (based on the reference wind velocity, U_{ref}) [-]

g   gravitational acceleration [m/s^2]

Gr   Grashof number [-]

H   height [m]

H_0 elevation of the bottom of the opening above the ground [m]

H_B height of the building [m]

H_{nl} distance from the neutral level to the ground [m]

H_{op} height of the opening [m]

I_u turbulence intensity [-]

L   length [m]

n   total number of measured points during the decay process [-]

p_w wind pressure [Pa]

Q_b buoyancy driven ventilation rate [m^3/s]

$Q_{w,bulk}$ wind driven bulk ventilation rate [m^3/s]

$Q_{w,eff}$ wind driven effective ventilation rate [m^3/s]

Q   total ventilation rate [m^3/s]

t_j elapsed time since the initial time of the decay curve [h]

$\overline{T}$ average temperature [ºC]

u_{ABL}^{*} friction velocity [m/s]

U(z)   streamwise velocity at a given height, *z* [m/s]

U_{10} wind velocity at the reference height of 10m [m/s]

U_{eff} effective air velocity through the opening [m/s]

U_{H_B} velocity at building's height [m/s]

U_L local wind velocity [m/s]

U_{L_x} horizontal component of the local wind velocity (parallel to façade) [m/s]

U_{L_z} vertical component of the local wind velocity (parallel to façade) [m/s]

U_{ref} reference freestream wind velocity [m/s]

V_{room} volume of the room [m^3]

W   width [m]

W_{op} width of the opening [m]

z height to the ground [m]

z_0 aerodynamic roughness length [m]

z_{10} reference height of the weather station (=10m) [m]

Acronyms

2D   two-dimensional

ABL   atmospheric boundary layer

CFD   computational fluid dynamics

CO_2 carbon dioxide

CR   cross ventilation

CV   corner ventilation

fps   frames per second

HWA   hotwire anemometer

NV   natural ventilation

PIV   particle image velocimetry

SS   single sided ventilation

SS1   single sided ventilation with one opening

SS2   single sided ventilation with two openings

WT   wind tunnel

3.2. Introduction

Most existing studies of wind driven SS1 ventilation use large opening to façade area ratios due to constraints in wind tunnel model size and flow scaling limitations. As a result, the SS1 flows that are studied are driven by pressure variations along the opening [14]. Further, SS1 flows are usually studied using plain openings [13,20,66,67,68]. Yet, most buildings do not use plain openings, instead, a partially opened and tilted window is the most common NV configuration [69,70].

Experimental studies focusing on the effect of windows in wind-driven SS1 flows are scarce, with just a few using reduced-scale models in WT [20,71] or measuring in full-scale buildings [20,72]. The remaining SS1 studies with windows focus on flows dominated by buoyant forces [73,74,75] or by the combination of wind and buoyancy [76,77]. In the existing literature, there is no comprehensive full-scale study on wind driven SS1 NV flows through partially opened windows.

3.2.1. Existing simplified models of SS1 airflow

Four main empirical correlations to predict SS1 airflow were proposed in the last five decades. Warren & Parkins [20] proposed the first empirical correlation. This correlation separates the flowrate calculation due to wind and buoyancy. The buoyancy component was based in previous studies on the natural convection of vertical openings [78,79] and is calculated using Eq.(3.1):

$$Q_b = \frac{1}{3} A_{op} C_d \sqrt{\frac{H_{op} g \Delta T}{\overline{T}}} \qquad (3.1)$$

The wind component is calculated using an expression derived from a simplified analysis of the two-dimensional turbulent shear-layer that develops along the opening:

$$Q_{w,eff} = F_{LE} A_{op} U_L \qquad (3.2)$$

This model introduces the effective flow number, F_{LE}, to account for the effects of the turbulent mixing process. Reduced-scale experiments were performed using an SS1 cubic model placed on the sidewall of a wind tunnel (outside the working section). The interface surface between the SS1 model and the WT working section had the plain SS1 opening (flush with the wind tunnel wall). This setup reproduces the effects of an infinitely large façade ($A_{op}/A_f \sim 0\%$) as the approaching wind is parallel to the opening plane, and the ventilation flow is driven by shear. For a parallel flow with a turbulent intensity of 9%, the authors measured an average mean F_{LE} for a plain opening of 0.035. In addition, this study also performed full-scale experiments in an SS1 room (with a plain opening) located in a single-story building. The measured ventilation rates were converted into F_{LE} using a U_L/U_{ref} ratio that was obtained through another WT experiment with a reduced-scale model of the full-scale building. As Warren & Parkins were interested in the mean features of SS1 NV, only the mean F_{LE} of 0.1 was reported. Note that no conclusion can be made on the value of F_{LE} for shear driven SS1 once this $F_{LE} = 0.1$ is also affected by pressure driven SS1 for certain wind incident angles. Yet, the authors suggested the mean F_{LE} value of 0.1 in the simple correlation for wind driven SS1 NV flows (see Eq.(3.2)). It is also relevant to highlight that Warren & Parkins also performed full-scale experiments to study the influence of side-hung windows on the effective ventilation rate. However, the authors concluded that there was a scarcity of data across the different wind angles that precluded further findings. In this model, the total SS1 flowrate was defined as the maximum of the predicted values from Eqs.(3.1)–(3.2):

$$Q = max(Q_s, Q_w) \qquad (3.3)$$

Building on the previous work, Yamanaka et al. [21] performed a set of WT studies using an SS1 reduced-scale cubic model located outside the tunnel, with the plain opening in the tunnel wall. This study indirectly measured F_{LE} for several opening aspect ratios (1:2, 2:1, 1:8, and 8:1), obtaining an average F_{LE} of 0.03. A second set of measurements was also performed, placing the same SS1 cubic room inside the wind tunnel, using a smaller, circular SS1

ventilation opening at the center of the façade. This measurement used three different approaching wind profiles (two uniform flows with different turbulent intensities and an atmospheric boundary layer), a range of wind velocities (3-9 m/s), and incoming wind angles (0º-180º). A mean value of $F_{LE} = 0.06$ was obtained, the double of the value measured with the model mounted on the side of the tunnel. The authors suggested that this discrepancy might be due to the presence of fluctuating wind pressure on the opening when the model was placed inside the wind tunnel.

It is important to note that three independent wind tunnel studies [20,21,71] measured an F_{LE} value significantly lower than the one proposed by Warren & Parkins (=0.1, cf. Eq.(3.2)) for wind-dominant SS1 flows. All these experiments had similar setups, with an SS1 model mounted outside the wind tunnel with a rectangular opening located in the tunnel surface. This configuration reproduces an infinitely large façade that models the shear ventilation mechanism in an SS1 room of a multistory building. The experimental results showed that F_{LE} is approximately 1/3 of the proposed value by Warren & Parkins and varied between 0.034 and 0.037. These similar wind tunnel results suggest that shear ventilation may only occur for a limited range of wind incident angles in an SS1 room in isolated buildings, but further research is still needed.

Recently, Carrilho da Graça [14] presented a simple analytical model of the turbulent mixing between outdoor and indoor air in a wind driven SS1 NV system. The model was developed using the shear layer entrainment hypothesis, following the same approach as [20]. The author introduced the bulk flow number, F_{LB}, because the new proposed model was based on the analytical calculation of the two-dimensional flow features of the mixing layer rather than on measurements of effective airflow (that are characterized by F_{LE}). The model is shown in Eq.(3.4) below (F_{LB} value of 0.051). In addition, the author calculated a value for the effective flow number (=0.035), as shown in Eq.(3.5). This model is applicable to rectangular openings located in a building façade with an opening to façade ratio (A_{op}/A_f) lower than 2%.

$$Q_{w,bulk} = F_{LB} A_{op} U_L = 0.051 A_{op} U_L \tag{3.4}$$

$$Q_{w,eff} = F_{LE} A_{op} U_L = 0.035 A_{op} U_L \tag{3.5}$$

In a previous study, Caciolo et al. [77] had concluded that the existing SS1 models overestimated the ventilation rates in buildings with a leeward opening. To address this problem, the same authors [80] proposed a correction factor to the thermal buoyancy expression suggested by Warren (cf. Eq.(3.1)) based on validated CFD simulations of an SS1 room with a plain opening. The new correction factor, ΔT^*, is a ratio of the effective temperature difference (ΔT_{eff}) to the temperature difference and is given by Eq.(3.6). The leeward SS1 correlation suggested by [80] can be then obtained substituting the temperature difference, ΔT, present in Eq.(3.1), by the effective temperature difference, ΔT_{eff}, as defined in Eq.(3.7).

$$\Delta T_{eff} = \Delta T \Delta T^* = \Delta T \left(1.335 - 0.179 \times U_{ref} \right) \tag{3.6}$$

$$Q = Q_b = \frac{1}{3} A_{op} C_d \sqrt{\frac{H_{op} g \Delta T^* \Delta T}{\overline{T}}} \tag{3.7}$$

De Gifs & Phaff [72] presented the second SS1 correlation based on 33 full-scale SS1 experiments performed on the first floor of a building located in an urban environment composed by low-rise buildings. The authors stated that the weighting of ½ in Eq.(3.8) is due to the bidirectional flow present in SS1 ventilation, i.e., the fresh air that enters the room only goes through half of the opening area, while extraction occurs in the other half. The effective velocity, U_{eff}, is calculated using Eq.(3.9) and depends on three terms, each representing the wind, thermal buoyancy, and turbulence, respectively. The values of the constants were obtained through its best fit with the measured data: $C_1 = 0.001$, $C_2 = 0.0035$ and $C_3 = 0.01$. The use of different window configurations (horizontally pivoted, side-hung, and sash windows) was investigated, but the authors concluded that no clear distinctions could be made for the window effect on the ventilation rate.

$$Q = \frac{1}{2} A_{op} U_{eff} \tag{3.8}$$

$$U_{eff} = \sqrt{C_1 U_{ref}^2 + C_2 H_{op} \Delta T + C_3} \tag{3.9}$$

Larsen & Heiselberg [13] performed a comprehensive set of 159 full-scale wind tunnel tests using an SS1 model with a plain opening and proposed a new SS1 correlation based on the orifice equation, as shown in Eq.(3.10). The authors adopted the same approach as [72] and considered that the inflow area was only half of the opening area, and that the pressure difference could be induced by wind, buoyancy, and/or turbulence, resulting in Eq.(3.11). The new correlation, shown in Eq.(3.12), is dependent on variables such as the incident wind angle (θ), the mean pressure coefficient at the opening (C_p) and the maximum pressure coefficient difference across the opening ($\Delta C_{p_{op}}$).

$$Q = C_d \frac{1}{2} A_{op} \sqrt{\frac{2|\Delta p|}{\rho}} \tag{3.10}$$

$$Q = \frac{1}{2} C_d A_{op} \sqrt{\frac{2\left|p_w + \Delta p_b + \Delta p_f\right|}{\rho}} \tag{3.11}$$

$$Q = A_{op} \sqrt{C_1 f(\theta)^2 |C_p| U_{ref}^2 + C_2 H_{op} \Delta T + C_3 \frac{\Delta C_{p_{op}} \Delta T}{U_{ref}^2}} \tag{3.12}$$

The three correlation constants (C_1, C_2, and C_3) were obtained using the least-squares method applied to the experimental data, and their values depend on the wind incident angle (θ), as summarized in Table 3.1. The function depending on the wind incident angle, $f(\theta)$, was obtained by fitting a four-order curve shape to $(U_L/U_R)/\sqrt{|C_p|}$. The average error of the Larsen & Heiselberg model is less than 23%, while the De Gifs & Phaff correlation gave an average error of 29%.

Table 3.1 – Values of the three correlation constants depending on the wind incident angles.

Wind incident angle (θ)	C_1	C_2	C_3
$\theta = 285°–360°$, $\theta = 0°–75°$	0.0015	0.0009	-0.0005
$\theta = 105°–255°$	0.0050	0.0009	0.0160
$\theta = 90°$, $\theta = 270°$	0.0010	0.0005	0.0111

The third SS1 correlation was proposed by Dascalaki et al. [81]. This study conducted a total of 52 full-scale SS1 experiments, 4 in a test cell and 48 on the first floor of a three-story office building. The objective of this work was to compare the measured SS1 ventilation rates (using a plain opening) with the prediction of six airflow network models and, if needed, propose calibration factors for those models. The ventilation rates generated by wind and thermal buoyancy were measured using tracer gas. The authors concluded that when the temperature difference between the exterior and interior was less than 1º C, the contribution of thermal buoyancy became negligible. As all six models were based on an identical approach (cf. Eq.(3.1)) to predict the SS1 NV flow, the authors opted to propose a correction factor, CF, to be added into Eq.(3.1). This correction factor varies the weight of the wind contribution to the total SS1 NV flow depending on the ratio of buoyant to viscous forces (as shown in Eq.(3.13)). This ratio is known as the Archimedes number, Ar, and is given by Eq.(3.14). Finally, the total SS1 NV flow could be expressed as Eq.(3.15), considering a $C_d = 1$. The values of $a = 0.08$ and $b = -0.38$ were found to best fit the experimental data.

$$CF = aAr_D^b \tag{3.13}$$

$$Ar_D = \left(\frac{Gr_{H_o}}{Re_D^2}\right) = \frac{g\ H_{op}^3\ \Delta T}{\overline{\overline{T}}\ U_{10}^2 D^2} \tag{3.14}$$

$$Q = Q_{b\ (C_d=1)} CF \tag{3.15}$$

Argiriou et al. [82] used a similar approach and proposed new correlation factors for SS1 NV systems in combination with four shading devices: external awning shading, external horizontal and vertical fins, or an external roller blind. As shown in Table 3.2, the values of the constants a and b depend on the configuration tested and, for the external fins, also depend on the position of the slats (open, tilted, or closed).

Table 3.2 – *Values of the constants a and b, depending on the external shading device.*

Shading device	Slat position	a	b
Awning	–	0.16	-0.23
Horizontal fins	Open	0.15	-0.29
	Tilted (37°)	0.16	-0.25
	Closed	0.14	-0.21
Vertical fins	Open	0.38	-0.16
	Tilted (45°)	0.06	-0.16
	Closed	0.08	-0.27
Roller blind	–	0.04	-0.31

Wang & Chen [83] performed a series of computational fluid dynamics (CFD) simulations with the goal of developing a new model that predicts SS1 wind driven NV flows for doorlike apertures. The fourth proposed SS1 correlation predicts the ventilation rate for a plain opening using the following expression (Eq.(3.16)):

$$Q_{w,eff} = \frac{C_d W_{op} \sqrt{C_p} \int_{H_{nl}}^{H_{op}+H_0} \sqrt{z^{2/7} - H_{nl}^{2/7}} \, dz}{z_{10}^{1/7}} U_{10} \tag{3.16}$$

where W_{op} is the width of the opening [m], H_{nl} is the distance from the neutral level (height at which the pressure difference becomes zero) to the ground [m], and z_{10} the reference height of the weather station (=10 m) [m]. Afterwards, Wang et al. [69] extended the model to also predict the ventilation rate for top, side, and bottom hung windows with the inclusion of a correction factor to the original model (cf. Eq(3.16)). The new factor is a function of the window tilt angle, γ, and the incident wind angle, θ. Given the complexity of the correction factors, with each of them being heavily dependent on the window used, the readers are referred to the original reference for a detailed description of the model.

The accuracy of existing SS1 models has been assessed in several studies. Results show that, despite being the simplest, the Warren & Parkins wind-driven correlation (Eq.(3.2)) is the most consistent and accurate, with average errors below 30% [13,68,76,80,84,85]. Still, two recent studies [86,87] indicate that the Warren & Parkins correlation may underpredict the ventilation

rate by a large margin. Part of that discrepancy may be due to inaccuracy in wind velocity near the window (local velocity, U_L).

A comprehensive literature review on the impact of windows on NV [88] has concluded that there are no simple SS1 correlations that model the effect of windows. According to this review, the increased complexity of the correlation proposed by [69] did not improve the accuracy of the Warren & Parkins correlation. This review also suggested the use of the Warren & Parkins approach as a basis to develop a model that can account for the impact of different window configurations in wind driven NV flows. Ideally, empirical correlations should be capable of predicting the NV flows with engineering precision and should be simple to facilitate the design of NV systems. However, the complexity of most of the SS1 correlations limits its widespread use for designing purposes. Moreover, most of the existing wind driven SS1 models do not distinguish shear and pressure driving mechanisms.

3.2.2. Proposed contribution

The present chapter (3) addresses three existing research gaps in the area of wind driven SS1 ventilation:

1. There are no detailed full-scale measurements of wind shear driven SS1 NV;
2. There are no full-scale measurements of the impact of different window geometries in wind shear driven SS1 NV;
3. There is no simple correlation based on local velocity to predict wind shear driven SS1 flows that can model different window geometries.

To address these research gaps, this chapter uses two interconnected experimental setups that test wind driven SS1 ventilation using reduced and full-scale models. The first is a reduced scale model that was tested in an atmospheric boundary layer (ABL) wind tunnel. This WT study was followed by a full-scale experiment in a test chamber that allowed for detailed measurements of the impact of eight window configurations on the effective airflow rate. The third and final phase of this research focused on the calculation of the effective flow coefficient (F_{LE}) for each window that was tested. These coefficients allow for a significant increase in the precision of Eq.(3.2) when modelling wind driven SS1 flows with windows. The next chapter (3.3) presents the experimental methods used. Chapter 3.4 presents the experimental results, followed by a discussion of the results (3.5) and the conclusion (3.6).

3.3. Methods

This chapter presents the measurement setups and methods used in the two experiments that were performed in this investigation. The WT study allowed for an analysis of the wind driven SS1 flow that spans outdoor and indoor. The model used has a plain opening (or sash window). The full-scale experiment begins with a plain opening and proceeds to test the impact of seven other window geometries on the SS1 flow.

3.3.1. Wind tunnel measurements

The wind tunnel measurements were performed in a closed-circuit WT (Gävle University, Sweden). This facility has a test section with 3 m (width) and 1.5 m (height) and adjustable air velocity (from 0.5 m/s to 27 m/s). WT air temperature is controlled by a dedicated air handling unit with heating and cooling capacity that ensures isothermal measurement conditions. The tunnel used a scaled representation of the atmospheric boundary layer (Figure 3.1(a)). The ABL profile was created by two sets of obstructions/roughness at the upstream region of the test section (cf. Figure 3.1(a)). The resulting incident wind velocity profile followed closely the power-law shown in Eq.(3.17), where: $U(z)$ is the streamwise velocity at a given height [m/s], H_B is the height of the building (=45 cm), U_{H_B} is the velocity at building height (≈3.5 m/s), z the height to the WT floor [m], and α is the power law coefficient (=0.26, the typical roughness of residential suburbs and small towns [89]). Figure 3.1(b) shows the measured wind velocity and turbulence intensity (I_u) profiles of the ABL, as well as the power-law wind profile predicted using Eq.(3.17). The turbulent intensity in a real ABL usually varies from 30%–40% at ground level to 5%–8% at gradient height (height above the ground where the friction due to the urban environment has a negligible effect on the wind speed) [90,91,92]. In Figure 3.1(b), one may observe that the turbulent intensity across the plain opening is around 15%, which agrees well with the typical values of a real ABL. The SS1 building was a three-story model with dimensions of 0.75 m × 0.60 m × 0.45 m (W × L × H), as shown in Figure 3.1(c). Only the middle floor had an active SS1 room where the ventilation was measured. The single square plain opening was positioned at mid-height of the active room and had an area of 56.3 cm^2, corresponding to an opening to wall area ratio of 1.7%. The ventilated room was centered with the wider façade of the model (cf. Figure 3.1(c)), had a square footprint with a 0.45 m side and a floor to ceiling height of 0.15 m. The active room had 4mm thickness Plexiglass walls, and the remaining components of the building models used opaque wooden boxes.

$$\frac{U(z)}{U_{H_B}} = \left(\frac{z}{H_B}\right)^{\alpha} \tag{3.17}$$
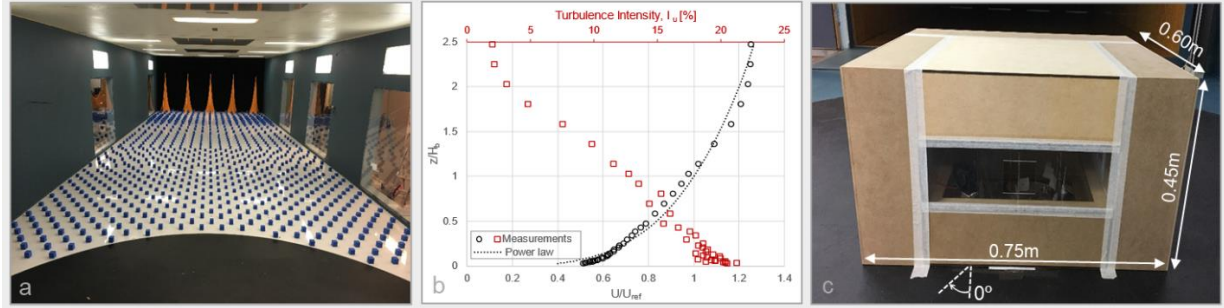
Figure 3.1 – (a) Setup of the roughness elements in the upstream zone of the WT; (b) measurements of the WT ABL profile and the fitting power-law for the velocity profile, predicted by Eq.(3.17) (black circles – normalized wind velocity; red square – measured turbulence intensity; black dashed line – power-law wind profile); (c) windward view of the reduced scale SS1 model and its dimensions.

The effective ventilation rates were measured, using the tracer gas decay method [93], in 13 different incoming wind directions (from 0º to 180º, with intervals of 15º). In each measurement, carbon dioxide (CO_2) was injected in the active room of the model using a vertical rod with holes in various directions to ensure well-mixed conditions. The CO_2 sampling system consisted of a grid of 15 evenly spaced CO_2 sampling points in the room at mid-height (sampling frequency of 20 Hz). The CO_2 concentration inside the WT was also measured. The effective ventilation rates were calculated using the time variation of the CO_2 concentration during the decay that occurred after CO_2 injection was turned off, through Eq.(3.18) [5,26,52]:

$$Q_{eff} = \frac{\left(\sum_{j=1}^{n} t_j\right) \cdot \sum_{j=1}^{n} ln\left[C(t_j)-C_{bg}\right] - n \cdot \sum_{j=1}^{n} t_j \cdot ln\left[C(t_j)-C_{bg}\right]}{n \cdot \sum_{j=1}^{n} t_j^2 - \left(\sum_{j=1}^{n} t_j\right)^2} \times \frac{V_{room}}{3600} \tag{3.18}$$

where Q_{eff} is the effective ventilation rate [m³/s], t_j is the elapsed time since the initial time of the decay curve [h] and $C(t_j)$ the CO_2 concentration at that time [mg/m³], n is the total number of measured points during the decay process, C_{bg} is the background CO_2 concentration, i.e., the CO_2 concentration inside the WT [mg/m³], and V_{room} is the volume of the active room [m³].

With the goal of mapping the two components of the local parallel to façade wind, air velocity measurements were made using two constant-temperature hot-wire anemometers (HWA, Multichannel CTA 54N82) with a single fiber-film probe (DANTEC 55R01). HWA measurements focused on the magnitude of the horizontal component of the local wind velocity, U_{L_x}, parallel to the wind tunnel floor surface, and on the magnitude of the vertical local wind velocity, U_{L_z}, perpendicular to the WT floor. The probes had their wires positioned vertically or horizontally to measure the air velocity in the horizontal or vertical planes, respectively [94]. The probes were located at the mid-height of the room and close to the center of the model (in front of the sealed window). The measurements were performed in isothermal conditions, in periods of 60 seconds, with a sampling frequency of 1kHz. The velocity measurements were performed for all the 13 wind incident angles used for the ventilation rate.

Smoke and particle image velocimetry (PIV) visualization techniques were used to analyze the shear layer that develops along the opening. With the wind tunnel running, smoke was injected inside the active SS1 room, and a camera recorded a slow-motion video, with a frame rate of 120 fps, to capture smoke being mixed with fresh air and being gradually removed from the room through the shear layer. The PIV laser equipment used was a Nd:YAG system, model Solo PIV III-15 Hz from New Wave Research. The laser was located 1.5m downstream of the model, creating a laser sheet parallel to the wind tunnel floor. This laser sheet was projected to the model at mid-height of the active room (22.5 cm). A smoke generator located downstream the model released high-density smoke that served as seed particles to be detected by the camera. In closed-circuit wind tunnels, placing a smoke generator downstream of the model results in a more uniform distribution of the particle seeds across the tunnel cross-section. The camera used was HiSense MkII model from Dantec Dynamics. The recorded images have a resolution of 1344x1024 pixels density and were shot at a frequency of 6 Hz. During the experiment, 60 pairs of frames were acquired over 10 s. Each pair consisted of two images that were captured with a 100 µs time interval. Each pair of images was then processed using the DynamicStudio software from Dantec Dynamics. The software cross-correlates sequential images to obtain a displacement of the seeding particles, creating a two-dimensional velocity field in the horizontal plane.

3.3.2. Full-scale measurements

The test chamber measurements were performed at the Cork Institute of Technology (CIT, Ireland). The full-scale test chamber simulated a single-opening room (SS1) located in an infinitely large façade. The interior dimensions of the chamber were 2.16 m × 3.32 m × 2.14 m (W × L × H). The single aperture was located in the narrower façade of the test chamber and had an area of 1 m². Figure 3.2(a) shows the setup used to produce the airflow for the experiments (hereafter referred to as the wind generator). The airflow was driven by a fan and channeled into a rectangular settling chamber with a duct section of 1.5 m height by 0.3 m width. Upstream of the settling chamber, a panel of honeycomb-shaped holes produced a uniform flow at the wind generator outlet (see Figure 3.2(b)).
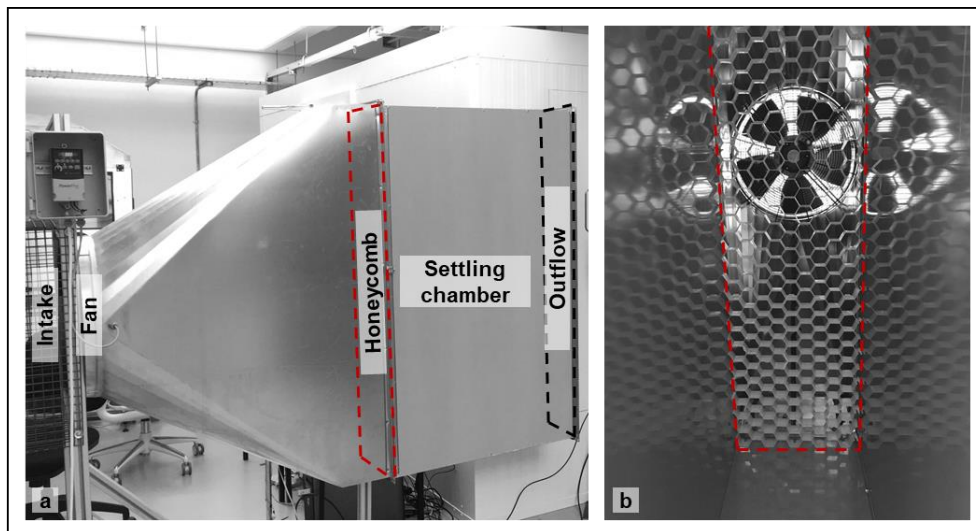
Figure 3.2 – (a) Outside view of the wind generator and its components; (b) Mesh of honeycomb-shaped holes located upstream the settling chamber.

The wind generator outlet was positioned as shown in Figure 3.3(a), parallel to the façade, and 0.2 m away from the opening of the test chamber. The airflow velocity and turbulence intensity were measured using omnidirectional anemometers. To ensure a uniform incident wind at the opening, the measurements were performed in three points along the height of the wind generator outlet (green dots in Figure 3.3(b)). Figure 3.3(c) and (d) show the experimental setup used inside the test chamber. The effective ventilation rate was obtained using the decay method (Eq.(3.18)) and CO_2 tracer gas. Inside the chamber, the CO_2 concentration was monitored using eight CO_2 sensors (shown as orange dots in the figure), divided into two groups of four sensors at ¼ and ¾ the height of the chamber. The background concentration was monitored by a CO_2

sensor located 3 m away from the chamber (not represented in Figure 3.3). CO_2 was injected into the middle of the chamber at ¼ of its height (red dots). During the pollutant injection, the chamber was completely sealed, including the opening (represented by the blue dashed line in Figure 3.3(c)), and a fan was used to assure well-mixed conditions. After achieving mixed conditions inside the chamber, the pollutant injection ceased, and the fan was turned off, the wind generator switched on, and the opening unsealed.
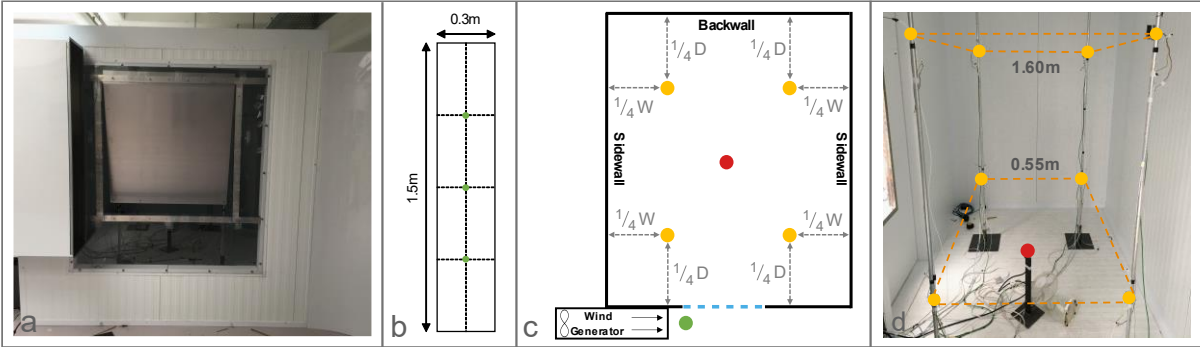
Figure 3.3 – Experimental apparatus used for the full-scale measurements: (a) – Position of the wind generator outlet relative to the single opening of the test cell; (b) – Location of the three anemometers that measured the wind velocity and its turbulent intensity at the outlet of the wind generator; (c) – Plan view of the sensor distribution inside the chamber; (d) – Perspective view (from the opening) of the sensor distribution by their height. (Green dots – anemometers; Orange dots – CO_2 concentration sensors; Red dot – CO_2 injection)

Figure 3.4 shows the eight SS1 window configurations that were tested in the full-scale measurements: one plain opening (or sash window) and seven window geometries. In configuration 1, two square opening areas were tested: a larger opening with an opening area, A_{op}, of 1 m^2 (not including the blue obstructions); and another smaller with $A_{op} = 0.5$ m^2 (shown in blue in the figure). The remaining configurations, 2–8, used the larger square opening with top-hung, side-hung, and bottom-hung windows tilted inwards or outwards. For the bottom-hung window (configuration 2), the opening area was calculated by adding the two triangular areas on the window sides with the rectangular area at the top. A tilt angle of $\gamma=14°$ was chosen across configurations 2 to 8 so that the opening area coincided with the smaller plain opening ($A_{op} = 0.5$ m^2).
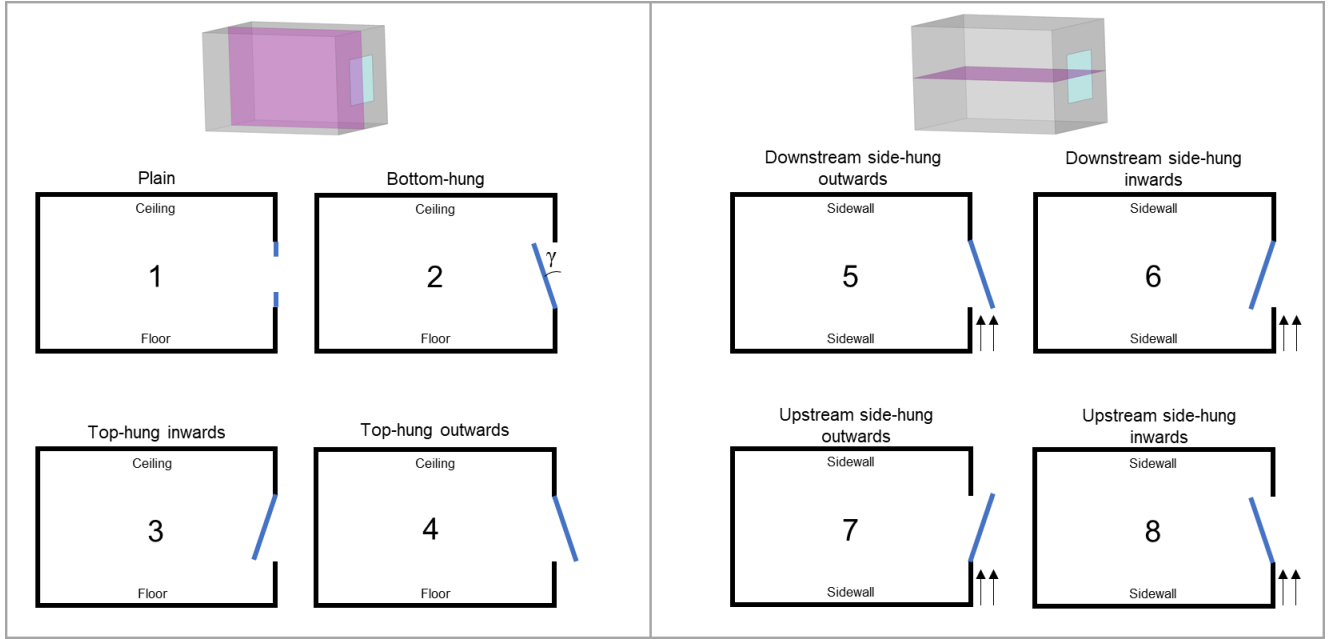
Figure 3.4 – Eight SS1 configurations tested. (Left: Lateral view of the test chamber considering a mid-depth cross section. Right: Top view of the test cell considering a mid-height cross section.)

3.4. Results

3.4.1. Wind tunnel experiments

3.4.1.1. U_L/U_{ref} ratio as a function of wind direction

Two HWA sensors measured the x and z components of the local wind velocity parallel to the façade for several wind incident angles. The magnitude of the local velocity was calculated using Eq.(3.19).

$$U_L = \sqrt{U_{L_x}^2 + U_{L_z}^2} \qquad (3.19)$$

To compare the measurements with literature, the local velocity data was normalized using the wind velocity at building height (U_{ref}). Figure 3.5 shows the variation of the ratio U_L/U_{ref} with the incoming wind angle and compares it with previous measurements from the literature [12,20]. The differences in the ratio U_L/U_{ref} along the wind angle between the different studies can be attributed to different building geometries and/or sensor positions relative to the building that were used in each measurement. In general, the shape of the curves is identical amongst

the different sources. These results indicate that the measured local velocities of this study agree well with the literature.
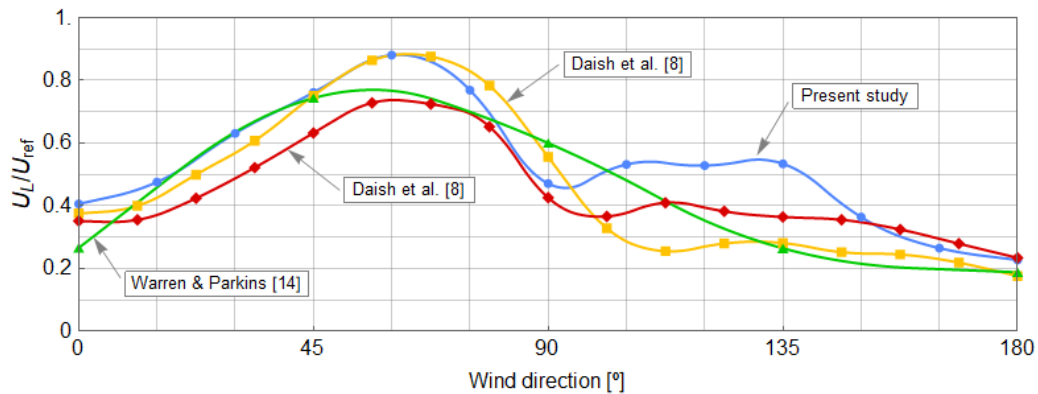
Figure 3.5 – Wind tunnel measurements of the local velocity relative to the reference velocity for different wind angles. Aspect ratios (W:H:L) of each building model with the opening facing the windward side (θ=0º): blue circles – 1.7:1:1.3; yellow squares – 4.8:1:2; red diamonds – 2.6:1:2; green triangles – 4.5:1:2.

3.4.1.2. Effective ventilation rates

The time variation of the CO_2 concentration in the room was similar across all measurements and displayed the typical shape of pollutant concentration decay in a ventilated space. Each measurement consisted of one mixing period with the pollutant being injected at a constant rate and one decay period when the pollutant injection stopped, as shown in Figure 3.6. Analysis of the logarithm of the CO_2 concentration profile reveals an initial period of pollutant mixing, resulting in an increase in CO_2 concentration inside the room (not shown in Figure 3.6). After this initial period, a good mixture of CO_2 is achieved inside the room as its concentration stabilizes for several seconds (green zone in Figure 3.6). Finally, the mixing period is halted when the pollutant injection stops, and the decay period begins with the decrease of the CO_2 concentration as a result of the non-polluted air that flows in. As expected, there is an intermediate phase during the decay period where the logarithm of the CO_2 concentration is an approximately linear function (blue zone in Figure 3.6). Using data from this linear period, the effective ventilate rate is calculated using the least-square method [5,26,52].
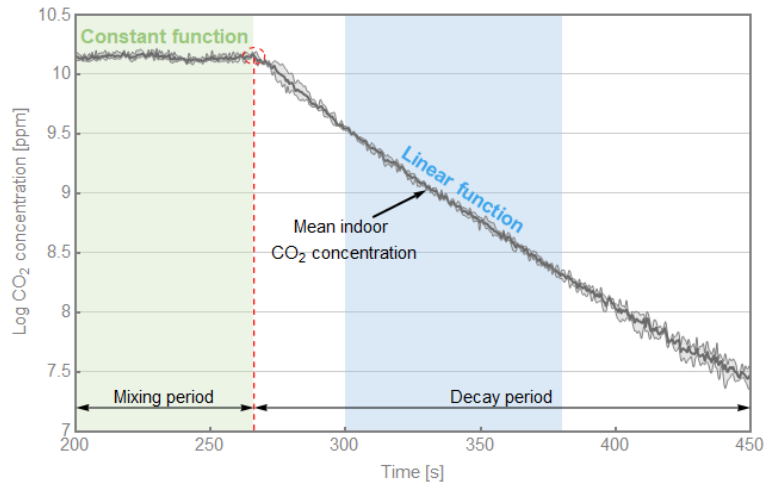
Figure 3.6 – Logarithm of the mean indoor CO_2 concentration during the mixing and decay periods (dark gray line) and its uncertainty (light gray bands) for the wind tunnel measurements.

Figure 3.7 shows the variation with wind direction of the effective ventilation rates, $Q_{w,eff}$, the effective flow number, F_{LE}, and their errors (shaded bands). The blue and red error bands denote the uncertainty of the measurements, defined as the standard deviation divided by the square root of the number of measurements [95]. The uncertainty of the effective flow number is higher than the effective ventilation rate because it depends on the uncertainty of both the effective ventilation rate and the local velocity measurements. The F_{LE} values were calculated using the opening area and the measured local velocity (see Chapter 3.4.1.1) using Eq.(3.2). Figure 3.7 shows that the effective flow number (blue line) depends on the wind incident angle, which may be due to several flow regimes that occur at different wind incident ranges. For wind angles in the range 0º–75º, the driving mechanism is wind shear with parallel to façade wind. In this range, a mean effective flow number of 0.043 was obtained, which is slightly higher than the existing values from the literature, 0.034–0.037, possibly because the wind tunnel experiments reported in the literature have adopted an infinitely large façade configuration (cf. Chapter 3.2.1). For an incident wind angle parallel to the opening plane (90º), the F_{LE} reaches a peak around 0.070, which may be explained by the development of an oscillating shear (due to flow separation at the leading edge of the building) that induces large fluctuations in the local velocity at the opening. Increasing the wind incident angle to 120º–150º is expected the presence of a single-vortex recirculation zone that induces shear wind at the opening, which explains the similarity of F_{LE} values when compared to the range 0º–75º. Finally, the range 165º–180º displays the highest values of F_{LE}. The existence of two oscillating shears at the leeward of the building causes periodic vortex shedding that generates large variations in the

local velocity [26], eventually reducing its mean value and increasing the effective flow number.

When compared with the effective flow number, the effective ventilation rate (red line) shows a smaller variation across the different wind angles. Still, two mild tendencies are observed for the effective ventilation rate. In the range 0º–90º, the ventilation rate tends to increase, while for wind angles between 90º–180º, the ventilation rate tends to decrease.
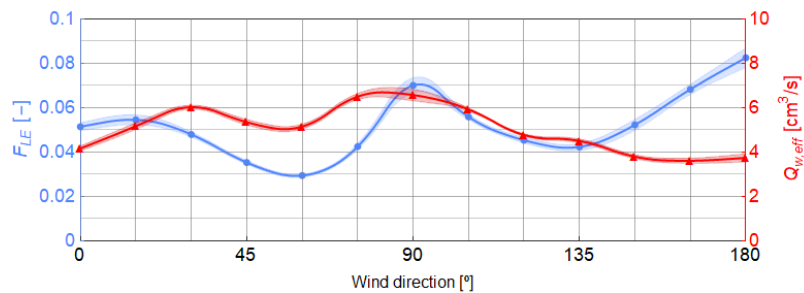
Figure 3.7 – Measured effective ventilation rate (red triangles) and calculated effective flow number (blue circles) for the SS1 reduced-scale model.

3.4.1.3. *Shear layer visualization*

Figure 3.8 shows the development of the shear layer at the opening of an SS1 room using smoke and PIV (45º incident wind angle). Figure 3.8(a) shows one frame of the slow-motion video that captured the SS1 shear ventilation using smoke. The figure shows the mixing that occurs in the shear layer between the fresh outdoor air and the indoor contaminated air (smoke). The smoke displays the limit of the shear layer (gray dashed line), with an increase in width along the opening. Figure 3.8(b) shows the results of the PIV measurements close to the façade and the opening, allowing for a direct comparison between the two visualization techniques. The two-dimensional velocity field was obtained from one pair of frames, and the results show an absence of outflow in the upstream edge of the opening with flow parallel to the façade and a gradual increase in the outflow close to the downstream edge of the opening. The flow pattern similarities with the smoke visualization (Figure 3.8(a)) confirm the presence of shear layer development.
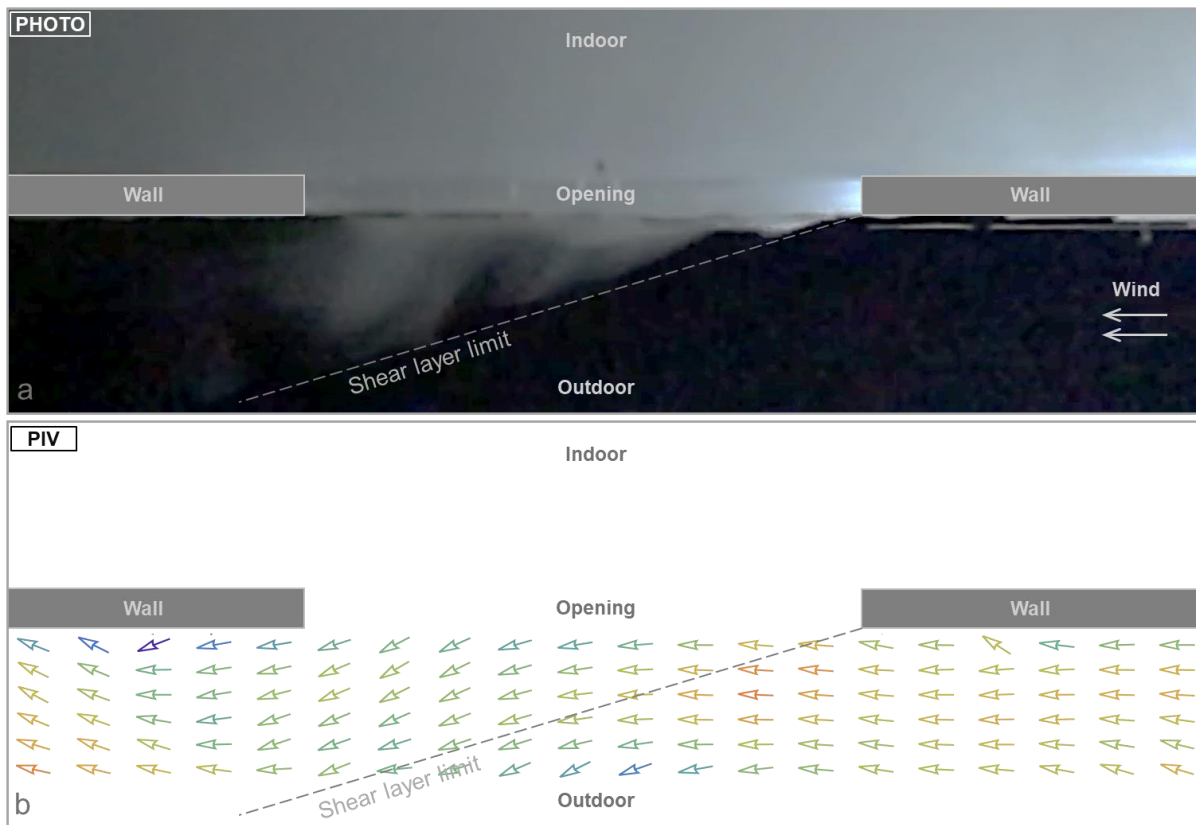
Figure 3.8 – Top view of the shear layer development along the opening: (a) smoke; (b) PIV.

3.4.2. Full-scale experiments

3.4.2.1. Validation

Figure 3.9 shows the air velocity and the turbulent intensity measurements of the wind profile in the outlet of the wind generator used in the full-scale experiment (cf. Chapter 3.3.2). Three different incoming air velocities were tested and characterized (1.1 m/s, 2.2 m/s, and 3.6 m/s). Each incoming air velocity displays small changes in magnitude along the height of the outlet, resulting in a nearly constant U_L velocity profile in the opening. The mean turbulent intensity of the wind profile is nearly independent of the incoming air velocity, with values ranging from 13% to 16%. This turbulent intensity is similar to the ABL of the WT (15%, cf. Chapter 3.3.1).
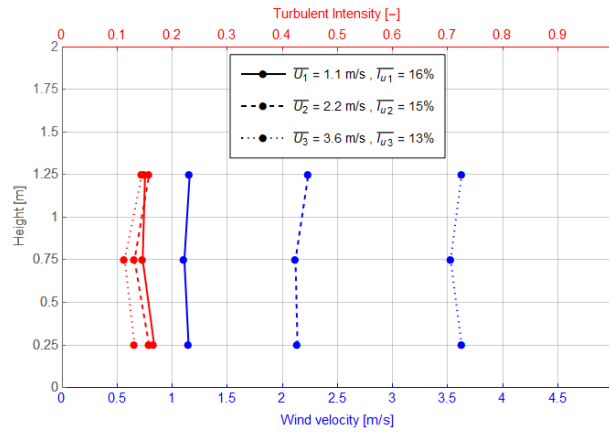
Figure 3.9 – Characterization of the wind profiles for three incoming air velocities: mean local velocity (blue) and turbulent intensity (red).

There is a need to verify that, for the case of the plain opening or sash window, the full-scale test chamber reproduces the SS1 shear driven flow observed in the WT. There were two steps in this verification. In step one, we confirmed, using smoke visualization, that, in the full-scale case, there was a shear layer developing along the opening. In the second step, we compared the F_{LE} values of the full-scale with the values obtained in the wind tunnel for the shear driven ventilation incoming wind angle range (0°–75°).

The full-scale experiment used 1 m^2 and 0.5 m^2 square plain openings (or sash windows) and a local velocity range of 1.1-3.6 m/s. Figure 3.10 shows the time variation of the CO_2 concentration inside the test chamber during the measurement of the 1 m^2 plain opening with 2.2 m/s wind. The similarities in the shape of the CO_2 concentration profile with Figure 3.6 are clear. The approach used in Chapter 3.4.1.2 is still valid for this measurement, and the effective ventilation rate was obtained using the least-square method during the linear period of the decay [5,26,52].
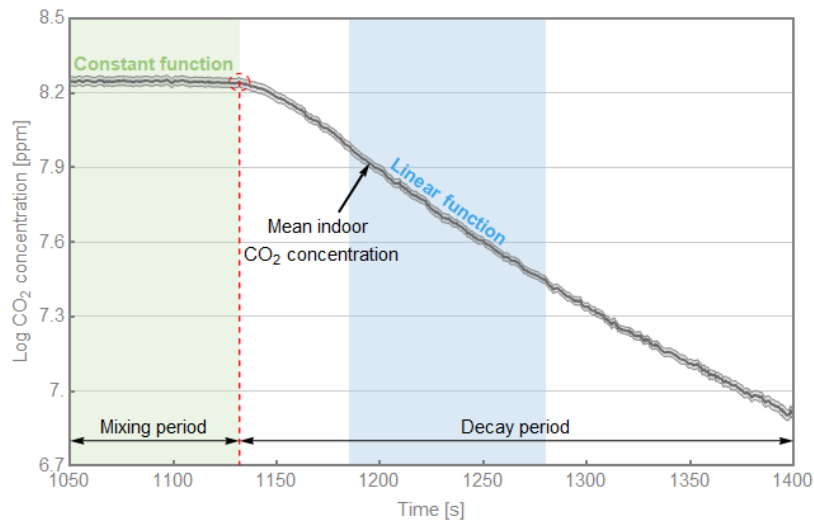
Figure 3.10 – Logarithm of the mean indoor CO_2 concentration during the mixing and decay periods (dark gray line), and its uncertainty (light gray bands) for the full-scale measurements.

The comparison of F_{LE} values between WT and full scale revealed good agreement. A mean F_{LE} of 0.036 was calculated for the full-scale experiment (obtained using Eq.(3.2)). The F_{LE} from the full-scale test chamber agrees well with the F_{LE} values reported in the literature (0.034–0.037). This value is 17% lower than the mean F_{LE} from the wind tunnel measurements for incident angles between 0° and 75° (0.043). As discussed in Chapter 3.4.1.2, this result may indicate that the full-scale measurement is closer to an infinitely large façade setup than to a reduced-scale setup as performed in the wind tunnel. Thus, the full-scale experiment was successfully validated to be used as a shear driven ventilation setup.

In addition to the comparison of values of F_{LE}, the influence of the parallel local velocity and the opening area in the effective flow number was assessed by testing three different local velocities (1.1 m/s, 2.2 m/s, and 3.6 m/s) for an opening area of 1 m^2. A second opening area of 0.5 m^2 was also used but only with a local velocity of 2.2 m/s. Table 3.3 shows the results of the F_{LE} calculations of the four cases tested. The results indicate that F_{LE} is independent of both the local velocity and opening area. The small variations in the F_{LE} across the four cases (0.033–0.038) were considered within the uncertainty of the measurements.

Table 3.3 – F_{LE} dependency on the opening area (A_{op}) and local velocity (U_L).

F_{LE}		A_{op}	
		1 m^2	0.5 m^2
	1.1 m/s	0.036	–
U_L	2.2 m/s	0.036	0.038
	3.6 m/s	0.033	–

3.4.2.2. *Effects of window geometry on F_{LE}*

The effects of the window configurations on the effective ventilation rate were measured using a local wind velocity (U_L) of 2.2 m/s. The effective flow number was calculated for each of the seven window configurations that were tested ($F_{LE_{window\ config}}$). To facilitate the comparison with the plain opening results (cf. Table 3.3), each $F_{LE_{window\ config}}$ was normalized using the mean F_{LE} value of the four plain opening cases, $\overline{F_{LE_{plain\ opening}}}$. The normalized effective flow number, $F_{LE}{}^*$, may is defined by:

$$F_{LE}{}^* = \frac{F_{LE_{window\ config}}}{\overline{F_{LE_{plain\ opening}}}} \tag{3.20}$$

Figure 3.11 shows the normalized effective number, $F_{LE}{}^*$, for each window configuration tested. The results varied from 0.77 for the downstream side-hung window tilted inwards (configuration 6) to 3.97 for both the downstream side-hung window tilted outwards and the upstream side-hung window tilted inwards (configurations 5 and 8, respectively). The window configuration 3 is equivalent to configuration 2. This top-hung inward opening configuration is usually not applied due to rain intrusion concerns.

The large variation of the $F_{LE}{}^*$ results indicates that, depending on the window configuration, the following airflow regimes occur:

58

- In configuration 1, the plain opening, the SS1 flow is driven by a shear layer, as discussed in Chapter 3.2.
- In configurations 2–4, the window limits the shear development since near the pivoting point, the window blocks the development of the shear. This disturbed shear eventually promotes mixing and increases the air exchange at the opening (when compared to configuration 1).
- Configurations 5 and 8 have similar ventilation mechanisms. Configuration 5 has an external wing wall that deflects the flow directly to the interior of the room, which increases the ventilation rate by a factor of 4 when compared to the plain opening (configuration 1). In configuration 8, the jet attaches to the window surface, a phenomenon known as the Coanda effect [96,97,98], and the flow is driven into the room, just like in configuration 5.
- Configuration 6 had the lowest ventilation rate of the eight configurations tested. The location of the window in this configuration blocks the region where the shear would be wider, decreasing the mixing and, consequently, the flow exchange.
- In configuration 7, the window channels the flow away from the aperture and creates a low-pressure zone between the downstream edge of the window and the aperture (outflow region). The inflow occurs along the bottom and top edges of the aperture.
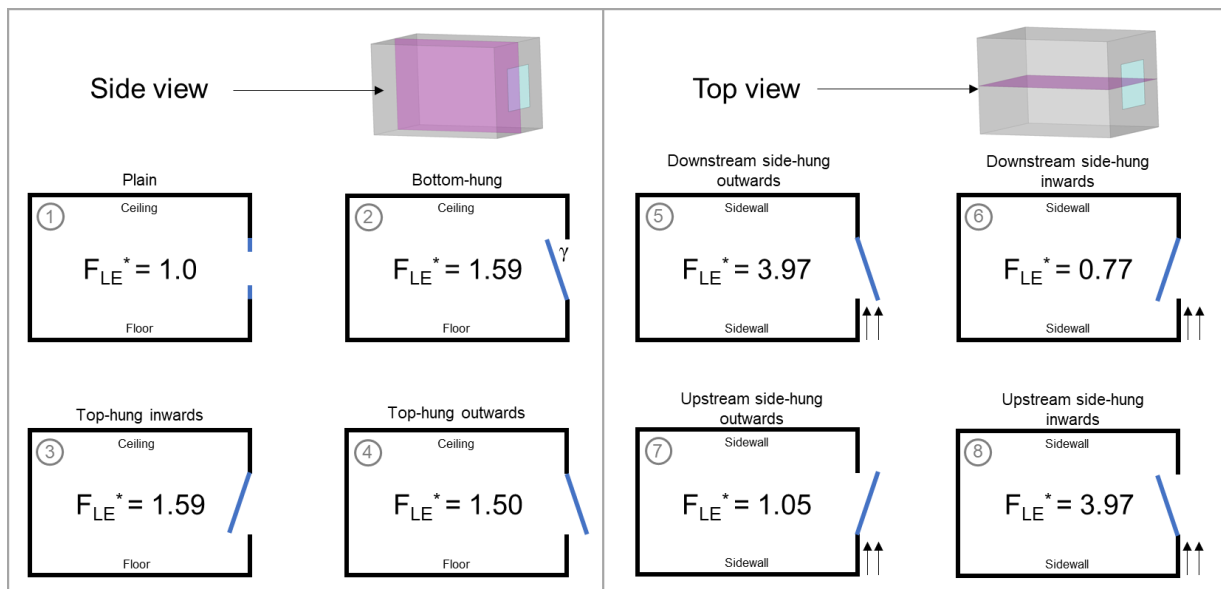
Figure 3.11 – Normalized effective flow number (F_{LE}^*) results for the eight SS1 configurations tested. (Left: Lateral view of the test chamber considering a mid-depth cross section. Right: Top view of the test cell considering a mid-height cross section.)

3.5. Discussion

A comparison between the plain opening F_{LE} values obtained in the two experiments performed in this work and the existing theoretical calculation based on shear layer turbulent mixing ([14], F_{LE} of 0.035) reveals a good agreement. The mean F_{LE} in the full-scale measurements (0.036) has a 3% deviation from the theoretical value. This result, along with the PIV and smoke visualizations shown in Figure 3.8, confirms that in large façades, the turbulent mixing shear layer is the driving mechanism for wind driven SS1 ventilation through plain openings. The WT measurements of shear ventilation resulted in a mean F_{LE} of 0.043, a value that is 20% higher than the theoretical calculation. This discrepancy may be due to the wide range of wind angles (0º–75º) used to calculate the mean F_{LE} for the WT. It is possible that in some orientations, the measured flow was not fully driven by shear.

The full-scale tests allowed for a detailed investigation of the interaction of different window geometries with the wind shear driven external flow. The range of measured F_{LE} values for different windows shows the large impact of the window configuration on the effective ventilation rate. The most effective window geometries deflect the wind flow into the room, while the least effective windows perform slightly worse than the plain opening (23% less flow). With the exception of case 1 (plain opening or sash window), all window geometries create pressure variations along the opening that deflect the flow. We can therefore conclude that these flows are driven by a combination of shear layer exchange and wind induced shear pressure along the opening. This should not be confused with the existing cases in the literature of SS1 flows driven by static pressure variation along the opening (these occur in cases with A_{op}/A_f of 10% or more). Clearly, one of the limitations of this study is the use of a single window aspect ratio. It can be expected that windows that have aspect ratios larger than three (height over width measured along the local wind direction) will have slightly different F_{LE} values. An additional limitation is the focus on wind driven flows. Whenever buoyancy is relevant, one can expect very interesting interactions between the two forces that definitely merit further work.

The F_{LE}^{*} values presented in the previous chapter showed that the effective SS1 NV rates can vary by a factor of 5, depending on the window configuration and local wind direction (in the façade plan). For all window configurations (except window 1), variations in wind incidence angle (measured along the building facade plan, β) have a large impact on the ventilation rate. Figure 3.12 shows the impact of the local wind angle for four typical window configurations (horizontal and vertical pivot, with the windows tilted inwards and outwards, shown in Figure

3.12(a)–(d)). Figure 3.12(e) shows significant variations in F_{LE}^* due to the local wind direction. Clearly, using a constant (F_{LE}) to predict SS1 NV may lead to significant modeling errors.
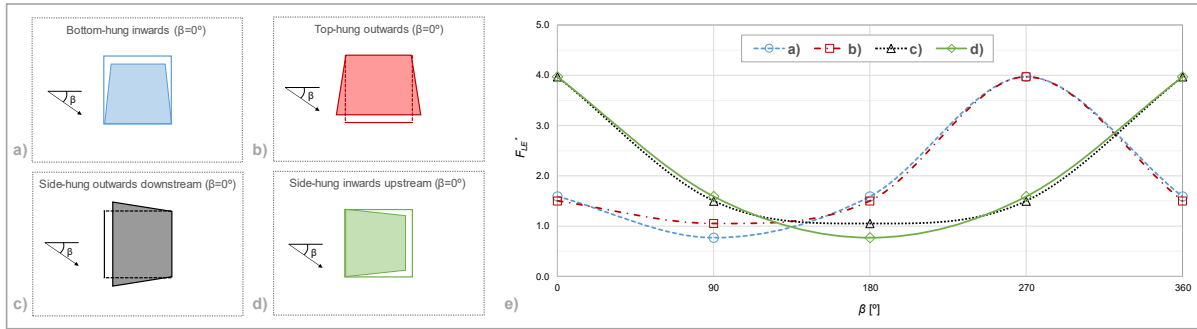
Figure 3.12 – (a)–(d): Front view of the window configuration; (e): Variation of the normalized flow number (F_{LE}^*) with the incident angle of the local wind (β) for each window considered.

The blue dashed line in Figure 3.12(e) corresponds to the configuration with the bottom-hung window tilted inwards when $\beta = 0°$. For $\beta = 0°/180°$, the resulting configuration (bottom-hung) leads to an F_{LE}^* value of 1.59 (same as configuration 2 in Figure 3.11). For $\beta = 90°$, the local wind flows downwards, which corresponds to a side-hung inwards downstream (equivalent to the window configuration 6 in Figure 3.11) and an F_{LE}^* value of 0.77. When $\beta = 270°$, the local wind flows upwards, matching the window configuration 8 ($F_{LE}^* = 3.97$). The analogy can be made for the three remaining lines in the figure. Comparison between the blue dashed and solid green lines show that the latter is a +90° phase-shift from the former. The same occurs for the red dash-dotted and black dotted lines. When comparing inwards (Figure 3.12(a) and (d)) with outwards opening windows (Figure 3.12(b) and (c)), it is clearly visible that, for small tilt angles ($\gamma = 14°$), the side to which the windows turn does not affect the ventilation rate. The inwards opening windows had an average F_{LE}^* of 2.40, slightly higher than the average obtained for outwards opening windows (2.38).

Clearly, for vertical or horizontally pivoted windows, F_{LE}^* is a function of β. However, the incident angle of the local wind, β, also depends on the reference wind incidence angle, θ, as discussed in Chapter 3.4.1.1. A simple correlation to predict wind driven SS1 NV flow, based on Eq.(3.2), is defined by:

$$Q_{w,eff} = F_{LE}^* A_{op} U_L \quad , \quad F_{LE}^* = f\big(\beta(\theta)\big) \tag{3.21}$$

The incident angle β is measured in the façade plane, while the incident angle θ is measured in the ground plane. For isolated buildings, designers must know how β varies with θ to accurately predict wind driven SS1 ventilation. Interestingly, estimating wind driven SS1 ventilation in low to mid-rise buildings surrounded by similar sized adjacent buildings organized into typical streets is simpler. This simplicity is due to the effect that the urban canyon has on the wind. Figure 3.13 shows the case of two SS1 rooms located in opposing facades of a building in a typical urban environment. In this environment, the streets confine the wind, creating two predominant wind directions [99,100]:

- Perpendicular wind occurs for the reference wind directions (θ) of 0º–60º, 120º–240º, and 300º–360º. These wind directions create a vertical vortex in the street canyon (see Figure 3.13(a)).
- Parallel wind occurs for reference wind directions of 75º–105º and 255º–285º [101]. These winds are channelled by the street canyon and therefore flow along the street direction (Figure 3.13(c)).
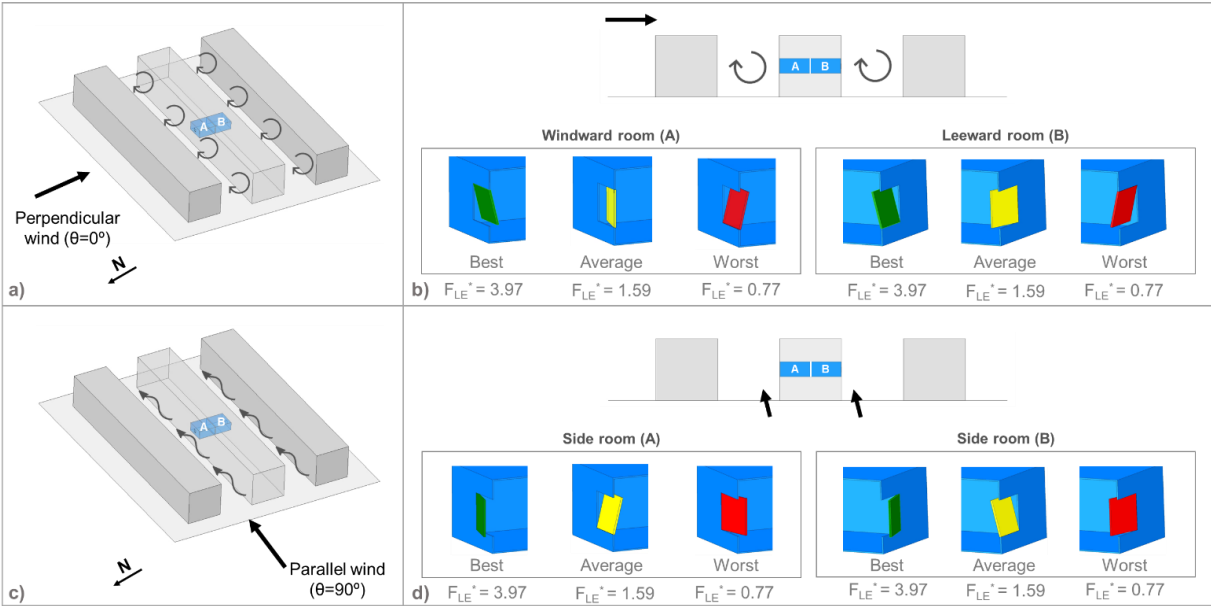
Figure 3.13 – (a) and (c): perspective view of a dense urban area with a prevailing wind perpendicular and parallel to the street canyon, respectively. (b) and (d): vertical view of a dense urban area (at the top) for perpendicular and parallel wind, respectively, and representation of the best, average and worst SS1 window configuration for each room.

Figure 3.13(b) and (d) show the best, average, and worst window configurations for each room orientation and wind regime in a typical urban street canyon. This information can be useful when designing SS1 wind driven ventilation systems in urban environments. Further, by using existing experimental studies of wind velocities in urban canyons, it is possible to estimate

typical ratios between average reference wind velocity (from the undisturbed wind field above the buildings) and average near façade velocity (U_L) in each case:

- Perpendicular wind: $\overline{U_{L_z}/U_{ref}} \approx 0.15$ [102].
- Parallel wind: $\overline{U_{L_x}/U_{ref}} \approx 0.3$ [103,104].

The reference wind velocity that is readily available in weather files is for open terrain, 10m height. For buildings with this height or taller, using this reference velocity is a suitable and increasingly conservative approach as the room height exceeds 10m. The effective SS1 wind driven airflow rate in urban environments can then be estimated using the following expressions (resulting coefficients shown in Table 3.4):

$$Q_{w,eff} = F_{LE_{window\ config}} A_{op} U_L \qquad (3.22)$$

$$Q_{w,eff} = F_{RE_{window\ config}} A_{op} U_{ref} \qquad (3.23)$$

Table 3.4 – Proposed coefficients for the simplified model to estimate SS1 effective flow in urban environments.

	Best window configuration	Worst window configuration
Perpendicular wind Windward/leeward rooms (A or B)	$F_{LE} = 0.143$ $F_{RE} = 0.021$	$F_{LE} = 0.028$ $F_{RE} = 0.004$
Parallel wind Side room (A or B)	$F_{LE} = 0.143$ $F_{RE} = 0.043$	$F_{LE} = 0.028$ $F_{RE} = 0.008$

3.6. Conclusions

This chapter presented an experimental study of the impact of typical window geometries on SS1 NV flows driven by wind shear parallel to the building façade. The experiments used two complementary setups, a wind tunnel test of a reduced-scale SS1 and a full-scale SS1 room subjected to artificial wind shear that was equipped with eight different windows.

The effective flow coefficient (F_{LE}) measured for the plain opening configuration in the full-scale experiment agrees with a recently published theoretical calculation (3% deviation). This agreement and the flow visualizations near the opening confirmed that wind driven SS1 flows in large facades are the result of a turbulent shear layer that develops in the opening plane. Results for seven window configurations show that the combination between window geometry and wind direction has a large impact on SS1 ventilation. For the same opened area, window configurations that direct the wind flow towards the room increase the flow by a factor of four (compared to a plain opening). In contrast, when the window configuration is unfavorable, the flow is reduced by up to 23%. The results of the experiments were incorporated into the most successful existing simplified SS1 model (Warren & Parkins), allowing for greatly increased precision when predicting wind driven SS1 flows.

This study identified the best window configurations for wind driven SS1 in dense urban environments. In this environment, the streets confine the wind, creating two predominant wind directions (parallel and perpendicular to the streets). By combining average results for measured wind velocities in street canyons with the measured window airflow performance, it was possible to propose simple correlations for wind driven SS1 in urban environments that are more precise than existing models.

4. PUMPING VENTILATION

4.1. Nomenclature

Symbols

α	power law coefficient [-]
ach	air changes per hour [-]
A_{eff}	effective opening area [m^2]
$C(t_j)$	CO_2 concentration at time, t_j [mg/m^3]
C_{bg}	background CO_2 concentration [mg/m^3]
$\overline{C}_{room}$	average CO_2 concentration [mg/m³]
C_μ	SST k-ω model empirical constant [-]
CFL	Courant–Friedrichs–Lewy number [-]
ε	turbulence dissipation rate [m^2/s^3]
ε_v	ventilation efficiency [-]
D	depth [m]
f_s	vortex shedding frequency [Hz]
H	height of the building [m]
I_u	turbulence intensity [-]
κ	von Kármán constant [-]
k	turbulent kinetic energy [m^2/s^2]
k_s	equivalent sand-grain roughness height [m]
L_s	distance between shear layers [m]
$\dot{m}_{released}$	CO_2 flow rate [mg/s]
n	total number of measured points during the decay process [-]
Q'	normalized ventilation rate [-]
Q_{bulk}	bulk ventilation rate [m³/s]

Q_{eff}	effective ventilation rate [m³/s]
Re	Reynolds number [-]
s	distance between the center points of two windows [m]
s'	non-dimensional window separation [-]
St	Strouhal number [-]
$St*$	wake Strouhal number [-]
t_j	elapsed time since the initial time of the decay curve [h]
TI	turbulence intensity [-]
u^*_{ABL}	friction velocity [m/s]
U	mean streamwise wind velocity [m/s]
$U(z)$	streamwise velocity at a given height, z [m/s]
U_∞	freestream velocity [m/s]
U_H	velocity at building's height [m/s]
U_{ref}	reference velocity [m/s]
U_s	velocity of the freestream flow at separation [m/s]
$\bar{V}$	mean horizontal velocity [m/s]
V_i	instantaneous horizontal velocity [m/s]
V_i'	deviation of the V_i from $\bar{V}$ [m/s]
V_{room}	volume of the active room [m³]
W	width [m]
ω	specific turbulence dissipation rate [s^{-1}]
y^+	dimensionless wall distance [-]
z	height to the ground [m]
z_0	aerodynamic roughness length [m]

Acronyms

2D	two-dimensional
3D	three-dimensional
ABL	atmospheric boundary layer
CFD	computational fluid dynamics
CO_2	carbon dioxide
CR	corner-ventilation
CV	cross-ventilation
DES	detached eddy simulation
DSGS	dynamic subgrid-scale
FIV	flow-induced vibrations
HWA	hot wire anemometry
LES	large eddy simulation
NITA	non-iterative time-advancement
NV	natural ventilation
PISO	pressure-implicit with splitting of operators
PIV	particle image velocimetry
RANS	Reynolds-averaged Navier-Stokes
SIMPLE	semi-implicit method for pressure-linked equations
SL	Smagorinsky-Lilly
SS1	single-sided ventilation with one-opening
SS2	single-sided ventilation with two openings
SST $k\text{-}\omega$	shear stress transport formulation of $k\text{-}\omega$ model
URANS	unsteady Reynolds-averaged Navier-Stokes
VIV	vortex-shedding vibrations
WT	wind tunnel

4.2. Introduction

Flow around bluff bodies is relevant to many engineering fields, such as building ventilation, structural vibration, bridges, wind turbines, transmission lines, chimneys, undersea pipelines and structures of offshore petroleum platforms [16,105,106,107,108]. In this type of flow, alternating vortex shedding generates periodic forces on the surface of the body. These forces induce vibrations, commonly known as, flow-induced vibrations (FIV) or vortex-induced vibrations (VIV). In the worst cases, FIV/VIV can result in structural failure, as shown in the infamous Tacoma Narrows bridge disaster in 1940 [105,109]. In recent applications, VIV is being used in wind and water current energy harvesting [110,111].

Figure 4.1 – Vortex shedding at different flow scales: (a) – vortex shedding at the cloud level as wind passes through a remote island [112]; (b) – vortex shedding at the wake region of a spanned cylinder [113]; (c) and (d) – smoke visualization of the oscillatory pumping ventilation mechanism (from this study).

One interesting feature of shear layer instability driven flows is that, for a given forcing velocity (wind or water current), the vortex shedding, and consequent surface forces occur at a fixed frequency (f_s). Strouhal [114] suggested a simple dimensional analysis of this oscillating flow mechanism. The analysis implies a proportionality between the freestream velocity and the velocity of the oscillation (normal to the shear layers). This velocity is obtained by multiplying the frequency, f_s, by the bluff body width (W). For a cube, there is only one length scale (i.e., width and depth, D, are the same), which would not, in general, be the case. The *Strouhal* number, *St*, is the ratio between the velocity of the oscillation and the freestream velocity (U_∞):

$$St = \frac{f_s \cdot W}{U_\infty} \quad .$$

(4.1)

As expected, pumping ventilation is an alternating flow with frequency f_s [6]. The *Strouhal* number depends on bluff body depth, *D*, and width, *W*, (hereafter referred to as aspect ratio, *D/W*), and flow regime [115]. In pursuit of a universal *Strouhal* number, Roshko [115] suggested an enhanced definition based on dimensional analysis of the similarity of the flow at the wake:

$$St^* = \frac{f_s \cdot L_s}{U_s} \quad , \tag{4.2}$$

where *St** is the wake *Strouhal* number, L_s is the distance that separates the two shear layers and U_s is the velocity of the freestream flow at separation [115] (see Figure 4.2). Roshko performed a wide range of measurements of different shaped bluff bodies under different flow regimes, obtaining an approximately constant *St** value of 0.16–0.17. Figure 4.2 illustrates the differences between the *Strouhal* number, *St*, and the wake *Strouhal* number, *St**. Despite the advantages of a universal *Strouhal* number (*St**), the complexity of the measurements increases substantially. Therefore, this chapter will only discuss *Strouhal* number (*St*), as introduced in Eq.(4.1).
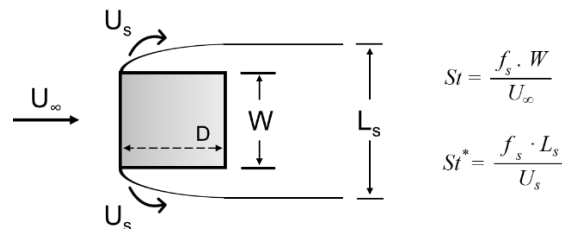
Figure 4.2 – Differences between St and St* definitions.

There are a limited number of experimental and numerical studies of the unstable interaction between shear layers as the main driving force of natural ventilation on buildings. Chu et al. [116] performed wind tunnel experiments on an isolated building with two openings in the same façade and varied the incident wind direction from 0° (openings located at the windward façade) to 180°. They showed that for incoming wind directions in the range 22.5°–45°, the ventilation rate is proportional to the time-averaged pressure difference. Further, for wind directions of 0° or between 67.5°–180°, the time-averaged pressure difference becomes negligible, and the

fluctuating pressure is the dominant driving force. A semi-empirical simplified model was proposed with a modification of the orifice equation to also include the fluctuating pressure. Daish et al. [16] performed wind tunnel experiments and identified pumping ventilation at the back and front façades. The experiments consisted of the measurement of the ventilation rate in an isolated and sheltered building with two planar openings. Different opening separations, s, were tested and the results showed that the measured ventilation rate is proportional to s, and pumping oscillations occurred with a St number of 0.11.

King et al. [117] compared, using LES and a lattice-Boltzmann method, the ventilation rates of a surrounded cross-ventilated room, when the flow is perpendicular and parallel to the openings. A higher ventilation rate for a parallel flow indicates that the vortex shedding of the upstream bodies generates turbulent eddies that promotes ventilation. No further information regarding the shedding frequency nor St number was provided. Kobayashi et. al [118] performed a CFD study of a three-dimensional cubic model with two plain apertures using LES. The study includes three cases of pumping ventilation with variable apertures separation, s'. The results show a linear increase in the ventilation rate with window separation (in contrast with the $s'^{1/2}$ variation proposed by [16]).

A recent numerical study [119] performed two-dimensional (2D) URANS simulations that were based on the experimental setup of [16]. This study analyzed how ventilation flowrates and vortex shedding frequencies varies with four aperture separations, seven different incident wind velocities and four aspect ratios. Results show a linear correlation between the ventilation rate and the separation of the apertures, while the ventilation rate show a linear increase with D/W from 0.4 to 0.8 and a linear decrease with D/W ranging from 0.8 to 2. For wind speeds below 5m/s, the ventilation rate increases with the incident velocity, however the study predicts that for wind speeds above 5m/s the ventilation rate would not further increase. This 2D study found that the frequency of the vortex shedding varied non-linearly with the wind velocity, which gives a $Strouhal$ number that varied from 0.095 (for a wind velocity of 1 m/s) to 0.038 (for a wind velocity of 7 m/s), contrasting with the St number of 0.11, presented by [16]. Another recent numerical study [120] performed a 3D URANS simulation of one floor of an infinitely tall building with two apertures at the front and back façades (according to the authors, a semi-2D geometry). In this study, the vortex shedding frequency varied linearly with the incident wind velocity, resulting in a $Strouhal$ number of 0.15. The ventilation rate for the case with the apertures located at the back façade is twice the ventilation rate of the case with apertures at the front façade. The ventilation rate increased with aperture separation, however as only two

different separations were used, no conclusive relation between these variables may be obtained. A third study by the same authors [121] performed 3D URANS simulations of one floor of two infinitely tall buildings with the goal of assessing how the ventilation rate varied with the distance between the target building and another building upstream, in a tandem configuration. Results showed a quadratic relation between ventilation rate and the distance between the two buildings, with a maximum ventilation rate when the distance is twice the depth of each building. Shedding frequencies were obtained downstream of each building and a *Strouhal* number was calculated. In both buildings, the *St* number was always the same for each distance case ($St \approx 0.10$–0.12), except when the buildings were connected (i.e., distance is zero), with a $St \approx 0.06$. The former *St* number is the lowest presumably because the length of the body doubled (cf. Eq.(4.1)). According to [119,120,121], 2D (and semi-2D) simulations of pumping ventilation are unable to capture several flow features:

- The 3D structure of the pumping ventilation flow mechanism present in buildings;
- The effect of the vertical component of the wake region caused by the rooftop of the building;
- The effect of the atmospheric boundary layer.

In addition to the need for an 3D experimental setup there is also an open question regarding the capability of URANS to simulate pumping ventilation. Although steady RANS may be a suitable choice for natural ventilation flows in single-sided one-opening (SS1), cross-ventilation (CV), and corner-ventilation (CR) strategies [12,44,66,122], previous studies [46,123,124] indicate that, as expected, steady RANS may not be a suitable approach for flows driven by unsteady shear, such as [125,126,127]. Recent studies proved that unsteady turbulence models, such as URANS, DES and LES, are reliable to correctly predict the shedding frequency of the vortices [125,126,127,128,129,130]. In the existing literature there are no validated numerical studies of pumping ventilation.

The present study addresses three existing research gaps in the area of pumping ventilation. There is no high-quality experimental dataset of pumping ventilation flow that uses a building model with partially open windows, analyzed using state of the art experimental methods. There are no studies that evaluate the capability of commonly used numerical simulation approaches (LES and URANS) to predict pumping ventilation. Finally, there are no previous studies that have analyzed the impact of window separation in the ventilation effectiveness of 3D pumping ventilation.

To address these research gaps, this chapter presents experimental and numerical 3D simulations of pumping ventilation that were performed with focus on the leeward side of a cubic building. The wind tunnel experiments use a large-scale model, 1/20 scale, that can simulate partially open windows (bottom-hung). Inclusion of realistic windows is essential since most buildings do not use planar openings (holes in the façade); instead, in practice a partially opened and tilted (top, bottom or side-hung) window is the most common NV configuration [69,70]. Airflow measurements are used to investigate the impact of window separation on the ventilation rate of a typical SS2 room that is induced by pumping ventilation. Flow visualization clearly identified the pumping ventilation cycle, whereas the velocity measurements captured the shedding frequency of the vortices. The numerical simulations used the unsteady turbulence models, URANS and LES, to predict the shedding frequency, pumping ventilation airflow rates and its ventilation effectiveness.

This chapter continues with a brief literature review of vortex shedding by bluff bodies (Chapter 4.3). Chapter 4.4 describes the wind tunnel experiments and Chapter 4.5 describes the experimental results. Chapter 4.6 gives an overview of the computational settings used and the numerical results. Finally, Chapter 4.8 summarizes the main conclusions.
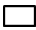
4.3. Brief review of existing studies of vortex shedding by bluff bodies
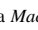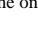
Table 4.1 provides a summary of the *Strouhal* number (*St*) obtained in experimental and validated numerical simulations, for different-shaped isolated buildings in turbulent flow conditions [25]. The studies, listed in Table 4.1, are divided into two-dimensional (2D) and three-dimensional (3D) vortex shedding.

The *St* number measured in 2D vortex shedding varies between 0.07 and 0.21. Square cylinders always have the same *St* number of 0.13 [131,132,133]. Rectangular cylinders with *D/W* < 1 display *St* number, based on *W*, between 0.13–0.15 [133]. Rectangular cylinders with *D/W* > 1 have a complex behavior, since some discontinuity steps are obtained, as shown in Figure 4.3 by the blue and red dashed lines. For 1 < *D/W* ≤ 2.5, the *St* values decreases, with increasing *D/W*, from 0.12 to 0.07 [131,132,133]. Between 2.5 < *D/W* < 3 there is a discontinuity step, where *St* varies from 0.07 to 0.17, as reported in different studies [131,133,134]. For 3 ≤ *D/W* ≤ 8, *St* decreases from 0.17 to 0.07 [131,133]. After, another discontinuity step appears at 8 < *D/W* < 10 [133]. For 10 ≤ *D/W* ≤ 25, *St* slowly decreases, with increasing *D/W*, from 0.19 to 0.16 [133]. Circular cylinders show the highest *St* number, reaching a value of 0.21 [115], because its rounded shape narrows the distance between shear layers (when compared with square shaped bluff bodies) and, as a consequence, rises the shedding frequency (cf. Eq.(4.1)). As Eq.(4.1) only takes into consideration the width of the body, the *St* number will increase, as discussed by [115].

Studies of 3D vortex shedding use building-like geometries and, comparatively to the 2D vortex shedding, the range of *St* number is lower, 0.09–0.15, and can be divided as follows. Square-shaped geometries have a *St* number ranging between 0.09 and 0.10 [126,129,135,136]. Rectangular-shaped geometries show a *St* number of 0.09–0.12 [16,125,128]. The only triangular-shaped geometry found in literature had a *St* number of 0.097 [137]. With the particular case of a cross-shaped geometry, the *St* number was 0.15 [130].

Table 4.1 – Strouhal number of different-shaped isolated geometries under turbulent regimes.

Ref.	Methodology	Vortex shedding phenomenon	Geometry	D/W	Re	St
[131]	WC, WT	2D	▭, ▢	1	$5.0\times10^3 - 2.0\times10^4$	0.13
				2		0.09
				3		0.17
				4		0.13
[132]	WT	2D	▢	1	$3.5\times10^4 - 3.4\times10^5$	0.13
					$3.7\times10^5 - 4.1\times10^5$	0.18 [1]
[133]	WC, WT	2D	▭, ▢	0.04 – 1	$7.2\times10^2 - 8.1\times10^4$	0.15 – 0.13 [2]
				1.11 – 2.5		0.12 – 0.07 [2]
				3 – 8		0.17 – 0.07 [2]
				10 – 25		0.19 – 0.16 [2]
[25]	WT	2D	◯	1	$1.0\times10^3 - 8.0\times10^3$	0.21
[125]	CFD (DES)	3D	▭	0.33	8.2×10^4	0.09 – 0.12
[126]	CFD (LES)	3D	▢	1	2.4×10^4	0.10
[128]	CFD (URANS & LES)	3D	▭	0.67	$1.8\times10^5 - 7.2\times10^5$	0.11 [3]
[129]	CFD (DES & LES)	3D	▢	1	2.4×10^4	0.09 – 0.12
[130]	CFD (DES)	3D	✚	1	5.0×10^4	0.15
[16]	WT	3D	▭	0.4	$1.9\times10^5 - 2.4\times10^5$	0.11
[135]	WT	3D	▢	1	$2.1\times10^4 - 4.4\times10^4$	0.09 – 0.10
[136]	WT	3D	▢	1	5.78×10^4	0.10
[137]	WT	3D	△	1	1.0×10^5	0.097

WT = wind tunnel experiment, WC = water channel experiment, CFD = computational fluid dynamics, URANS = unsteady Reynolds-averaged numerical simulation, LES = large eddy simulation, DES = detached eddy simulation, 2D = two-dimensional phenomenon, 3D = three-dimensional phenomenon, ▭ = rectangular geometry, ▢ = square geometry, ◯ = circular geometry, △ = triangular geometry, ✚ = cross geometry. [1] wind tunnel velocities with a *Mach* number above 0.8. [2] *St* decreases when the *D/W* ratio increases. [3] Although the *St* number was the same throughout all the CFD models tested, LES was the only model to accurately predict a power spectrum similar to the experimental one.
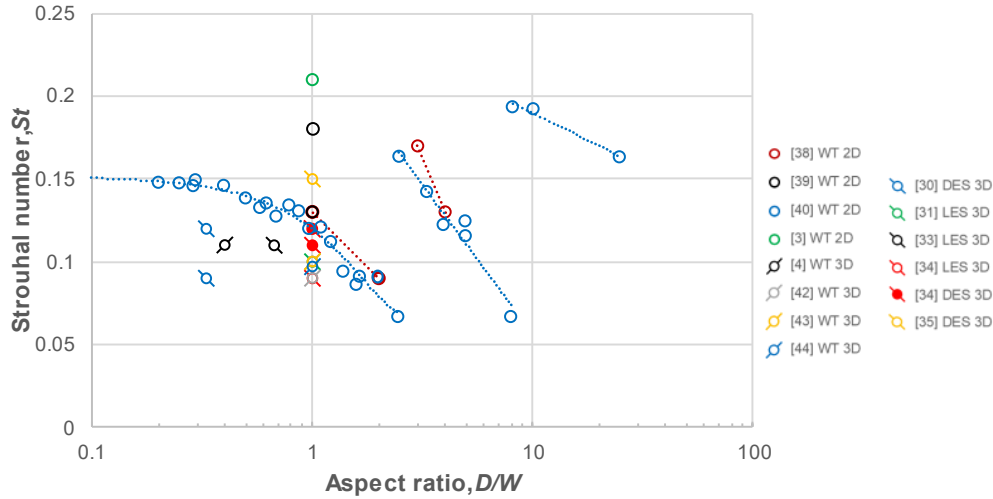
Figure 4.3 – Strouhal number data from existing experimental and numerical studies and its variation with the aspect ratio.

4.4. Experimental setup

This chapter describes the wind tunnel experiments, the airflow and velocity measurement systems. Ventilation rates were measured using tracer gas, while the flow velocity was measured using a hot wire anemometer (HWA) and particle image velocimetry (PIV).

4.4.1. Wind tunnel and model description

The experiments were performed in the atmospheric closed-circuit boundary layer wind tunnel of Gävle University (HiG, Sweden). The wind tunnel, shown in Figure 4.4, has a test section of 3m (width) by 1.5 m (height) and 11 m (length). The wind tunnel has an adjustable air velocity that can vary between 0.5 m/s and 27 m/s. The internal air temperature is controlled by a dedicated heating and cooling system, allowing for isothermal measurement conditions. To generate a turbulent atmospheric boundary layer (ABL) profile, a set of five equally spaced triangular spires was placed upstream of the test section, as shown in Figure 4.4(a). In addition, parallelepiped shaped surface roughness elements with different dimensions and distribution densities could be positioned on the wind tunnel floor. The incident wind velocity profile can be characterized by the following power-law:

$$\frac{U(z)}{U_H} = \left(\frac{z}{H}\right)^{\alpha} \; , \tag{4.3}$$

where $U(z)$ is the streamwise velocity at a given height [m/s], U_H is the velocity at building's height (≈ 3.5 m/s), z is the height to the wind tunnel floor [m], H is the height of the building (=45 cm) and α is the power law coefficient (=0.26), which represents a roughness equivalent to residential suburbs and small towns [89]. Figure 4.4(b) shows the measured wind velocity and turbulence intensity (TI) profiles of the boundary layer, as well as the predicted wind profile using Eq.(4.3).

The three-story model used for the wind tunnel experiments was a 1/20 scaled building (see Figure 4.4(c)). The model was formed by three floors with 0.15 m height each: two closed rooms at the top and bottom floors; and one active room in the middle floor with two openings at the leeward façade. The active room has Plexiglas walls with 4 mm thickness, while the closed top and bottom rooms are wooden boxes. The two bottom-hung square Plexiglas windows were positioned at mid-height of the room, having sides of length 0.075 m, and were tilted by 14 degrees to the interior of the room. Further, for experimental case labeling and analysis purposes, this chapter will adopt the non-dimensional window separation definition, *s'*, proposed in [16]:

$$ s' = \frac{s}{W} \ , \tag{4.4} $$

where *s* is the distance between the center points of the windows. Measurements were performed on the active middle floor for three different window separations (*s'*): 0.25, 0.50 and 0.75.
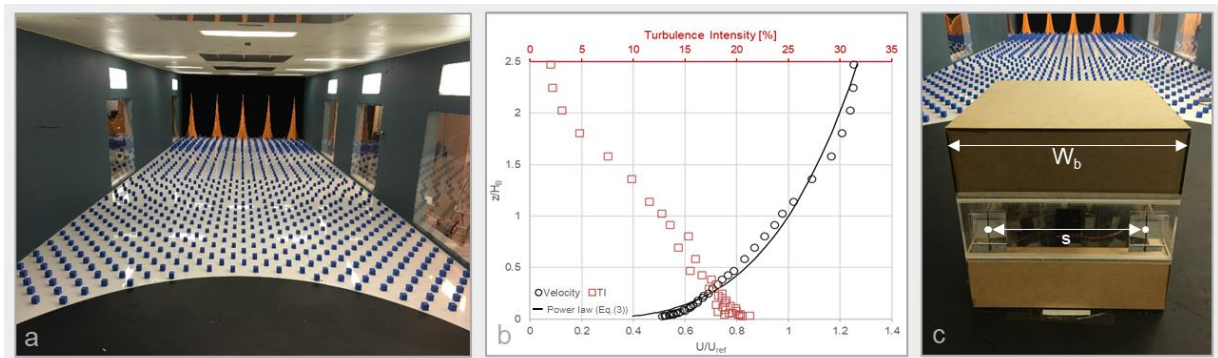
Figure 4.4 – (a) Distribution of spires and roughness elements within the wind tunnel; (b) measured wind velocity (black circles) and turbulence intensity (red squares) profiles of the wind tunnel boundary layer and power law wind profile (black line) predicted by Eq.(4.3); (c) building model with two bottom-hung windows at the leeward façade.

4.4.2. Ventilation rates

Carbon dioxide (CO_2) was used as a tracer gas, injected in the model room using a vertical rod with holes in various directions to achieve well-mixed conditions (Figure 4.5). A sampling grid with 15 evenly spaced points in a horizontal plane was used to measure the CO_2 concentration levels inside the room at mid-height, with a sampling frequency of 20 Hz. The background CO_2 concentration inside the wind tunnel was also measured. Ventilation rates were obtained using a multi-point decay method. From the time variation of the CO_2 concentration during the decay, the effective ventilation rate was calculated using Eq.(4.5) [52]:

$$Q_{eff} = \frac{(\sum_{J=1}^{n} t_j) \cdot \sum_{j=1}^{n} ln[C(t_j)\text{-}C_{bg}] - n \cdot \sum_{j=1}^{n} t_j \cdot ln[C(t_j)\text{-}C_{bg}]}{n \cdot \sum_{j=1}^{n} t_j^2 - (\sum_{j=1}^{n} t_j)^2} \times \frac{V_{room}}{3600} \tag{4.5}$$

where Q_{eff} is the effective ventilation rate [m³/s], t_j is the elapsed time since the initial time of the decay curve [h] and $C(t_j)$ the CO_2 concentration at that time [mg/m³], n is the total number of measured points during the decay process, C_{bg} is the background CO_2 concentration [mg/m³], and V_{room} is the volume of the active room [m³].
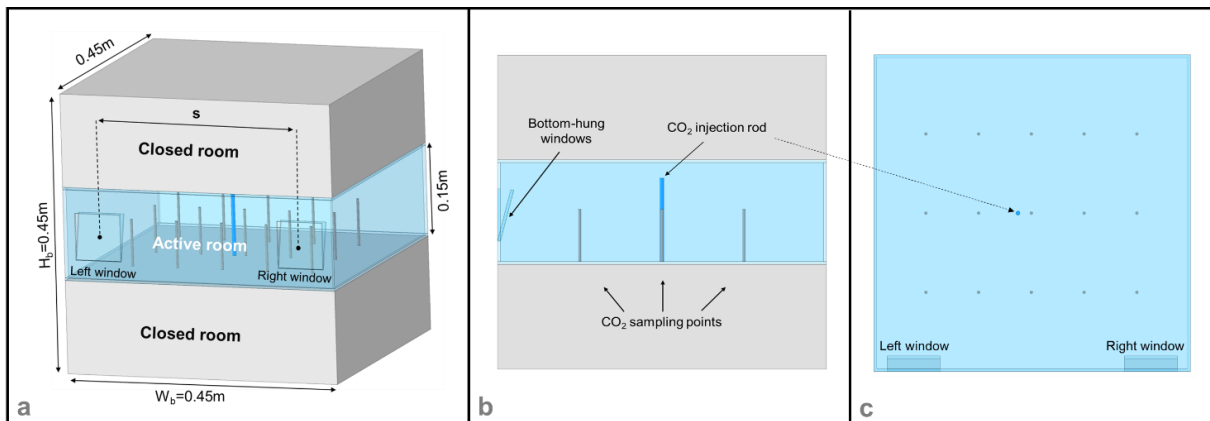
Figure 4.5 – Setup of the scaled building model used during the wind tunnel measurements: (a) – dimensions of the model; (b) – elevation view of the model; (c) – distribution in plan view of the CO_2 sampling and injection points.

4.4.3. Velocity measurements

4.4.3.1. Hot wire anemometer measurements

With the goal of analyzing the oscillatory mechanism of vortex shedding, velocity measurements were made using a constant-temperature hot wire anemometer, HWA, (Multichannel CTA 54N82) with a single fiber-film probe (DANTEC 55R01). The wire of the probe was positioned vertically to measure the velocity in the horizontal plane [94]. The probe was located at the mid-height of the room, in the vicinity of one of its trailing corners (see Figure 4.6). Measurements were performed in isothermal conditions, in periods of 60 seconds, with a sampling frequency of 1 kHz. HWA measurements focused on the magnitude of the air velocity in the horizontal plan, parallel to the wind tunnel floor surface. To detect the velocity oscillations induced by the vortices the analysis focuses on the deviation of the instantaneous horizontal velocity from the mean horizontal velocity, V_i', defined as:

$$V_i' = V_i - \overline{V} \ , \tag{4.6}$$

where V_i is the instantaneous horizontal velocity measured from the HWA [m/s] and $\overline{V}$ is the mean horizontal velocity over the time of the experiment [m/s].

4.4.3.2. PIV measurements

PIV was used to measure the 2D velocity flow field on the leeward side of the building. The area of these measurements was the trailing corners of the building model (where the vortex is created). The vortex shedding frequency is independent of the window separation [16,120]. Therefore, PIV measurements were only performed for window separation, s', of 0.75. Figure 4.6(a) shows the HWA and PIV equipment setup inside the wind tunnel. Figure 4.6(b) shows the area of interest considered for the PIV experiment and the horizontal position of the HWA.
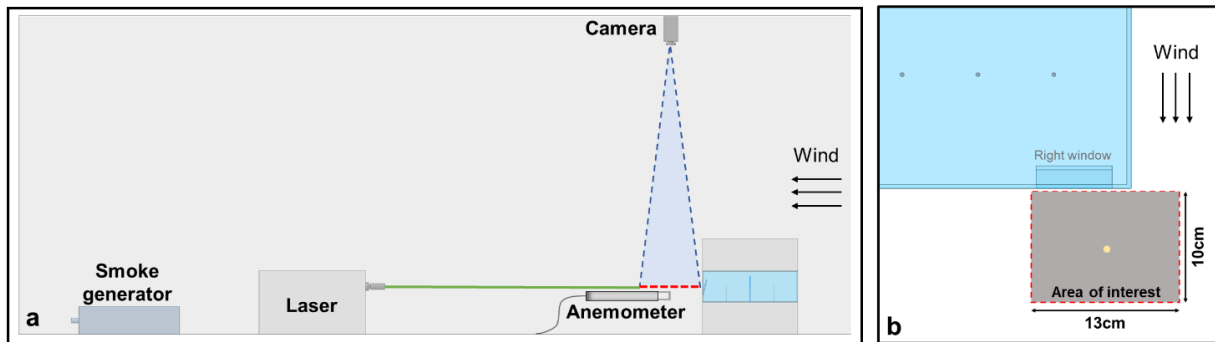
Figure 4.6 – Wind tunnel velocity measurements setup: (a) – vertical position of the anemometer and the distribution of the PIV equipment inside the wind tunnel (vertical view); (b) –position of the anemometer (yellow dot) and dimensions of the area of interest considered in the PIV measurements (horizontal view).

The PIV laser equipment used was a Nd:YAG system, model Solo PIV III-15Hz New Wave Research. The laser was located 1.5 m downstream of the model, creating a laser sheet parallel to the wind tunnel floor. The camera used was HiSense MkII model from Dantec Dynamics. The recorded images have a resolution of 1344x1024 pixels density and were shot at a frequency of 6 Hz. During the experiment, 60 pairs of frames were acquired over 10 s. Each pair consisted of two images that were shot with a 100 µs time interval. A smoke generator located downstream the model released high-density smoke that served as seed particles to be detected by the camera. This study used a closed-circuit wind tunnel. In this type of wind tunnel, placing the smoke generator downstream of the model results in a more uniform distribution of the particle seeds across the tunnel cross-section. Each pair of images captured by the camera was processed using the DynamicStudio software from Dantec Dynamics. The software cross-correlates sequential images to obtain a displacement of the seeding particles, creating a two-dimensional velocity field in a horizontal plane.

4.5. Experimental results

4.5.1. Smoke visualization

With the wind tunnel running, smoke was injected inside the active model room to visualize pumping ventilation. Figure 4.7 shows three moments of the pumping ventilation cycle. In Figure 4.7(a) air flows into the left window and flows out of the right window and into the vortex that will be released. Figure 4.7(b) shows the transition period between the formation of the right and left vortices. Finally, Figure 4.7(c) shows the left vortex in formation, with a high-pressure zone close to the right window (inflow) and a low-pressure zone at the left window

(outflow). The vortex is feed with room air during the low-pressure phase and is detached and released from the back of the building during the high-pressure phase.
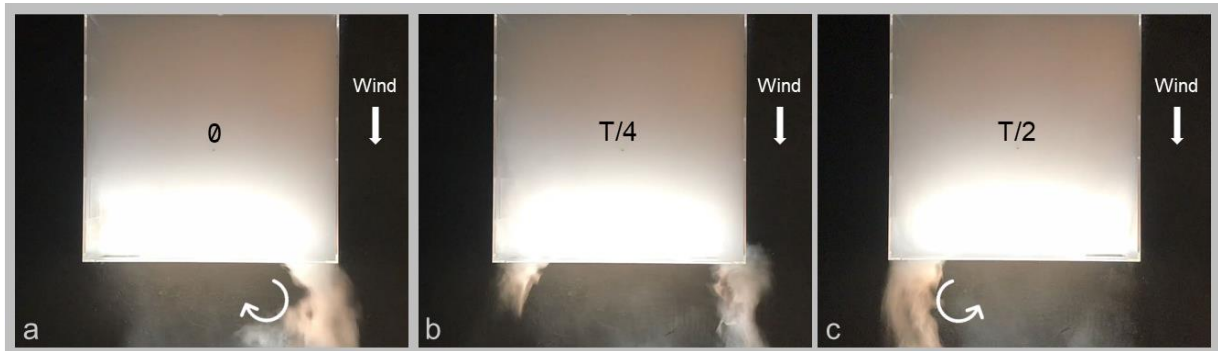
Figure 4.7 – Top view of the oscillatory driving mechanism for pumping ventilation using smoke (s'=0.75): (a) formation of a right vortex – air flows from the left to the right window; (b) no vortices – transition period between the right and left vortices; (c) formation of the left vortex – air flows from the right to the left window.

4.5.2. Effective ventilation rate

The time variation of the CO_2 concentration profile is similar across all the measured cases and displays the typical shape of pollutant concentration decay in a ventilated space. Figure 4.8(a) shows the background and the interior mean CO_2 concentrations during pumping ventilation measurement for the case with a separation of 0.50.

Analysis of the CO_2 concentration profile reveals an initial period of pollutant injection and mixing, resulting in an increase in CO_2 concentration inside the room. In the next period the concentration stabilizes while CO_2 is still being injected at a constant rate. Finally, in the last period the pollutant injection stops, and the concentration decays as a result of the non-polluted air that flows in. As expected, the logarithm of the CO_2 concentration in the decay period is an approximately linear function, as shown in Figure 4.8(b).
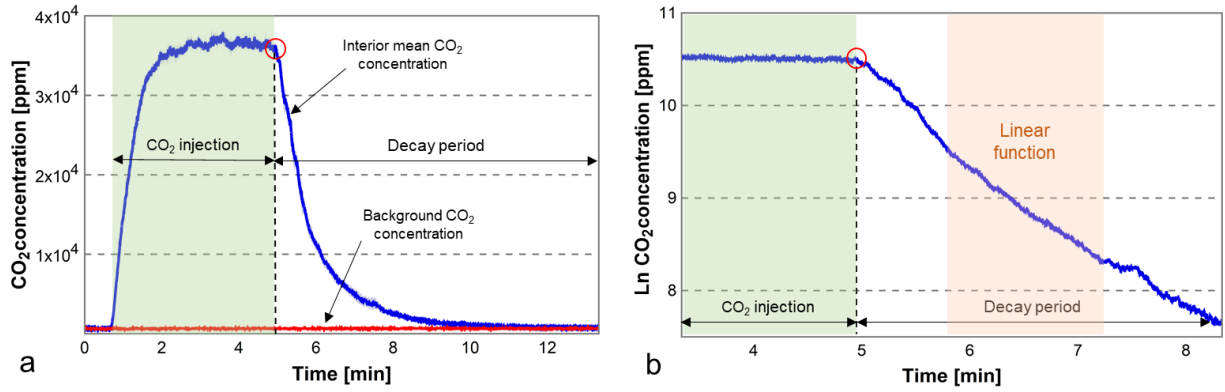
Figure 4.8 – (a) Interior mean and background CO_2 concentration profiles during a measurement; (b) Logarithm of the interior mean CO_2 concentration and the linear period during the decay.

The flow rate analysis presented in this chapter uses the following normalized ventilation rate definition (Q'):

$$Q' = \frac{Q_{eff}}{U_{ref} \cdot A_{eff}} \quad , \tag{4.7}$$

where Q_{eff} is the measured effective ventilation rate [m^3/s]; and U_{ref} is the reference velocity (the air velocity at building-top height, 45 cm, $U_H \approx 3.5$ m/s). Here A_{eff} is the effective opening area [m^2], defined by:

$$A_{eff} = \frac{(A_1 \cdot A_2)}{\left(A_1{}^2 + A_2{}^2\right)^{1/2}} \quad , \tag{4.8}$$

where A_1 and A_2 are the areas of each bottom hung inward opening windows [m^2]. These areas are calculated by adding the two triangular areas on the window sides with the rectangular area at the top. For the model used the A_{eff} is 20 cm^2.

The variation of the non-dimensional ventilation rate, Q', with the window separation, s', calculated using Eqs.(4.7) and (4.8) is shown in Figure 4.9. The measured normalized ventilation rate, Q', ranged between 0.67 and 0.95. The normalized ventilation rate, Q', increases linearly with the separation, s', with a Pearson squared correlation coefficient of 0.99. This linear variation is in-line with the numerical results from [118] but is different from the $s'^{1/2}$ variation of airflow rate with separation, proposed by [16].
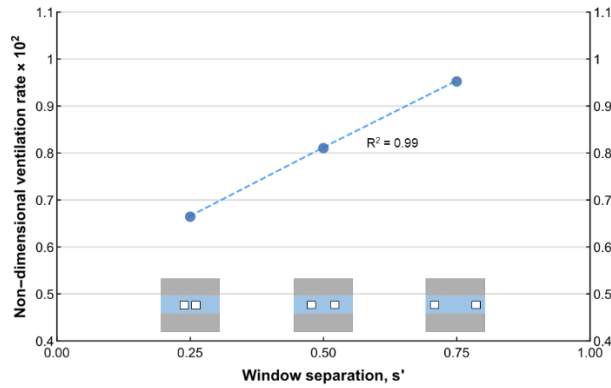
Figure 4.9 – The three measured ventilation rates with a linear fit and its correlation coefficient, R^2.

4.5.3. Velocity measurements

The PIV measurements confirm the conclusions of the smoke observations presented in Chapter 4.5.1. To allow for a direct comparison, Figure 4.10 shows three frames of the PIV measurements in the area of interest behind the right window in the same sequence as Figure 4.7.
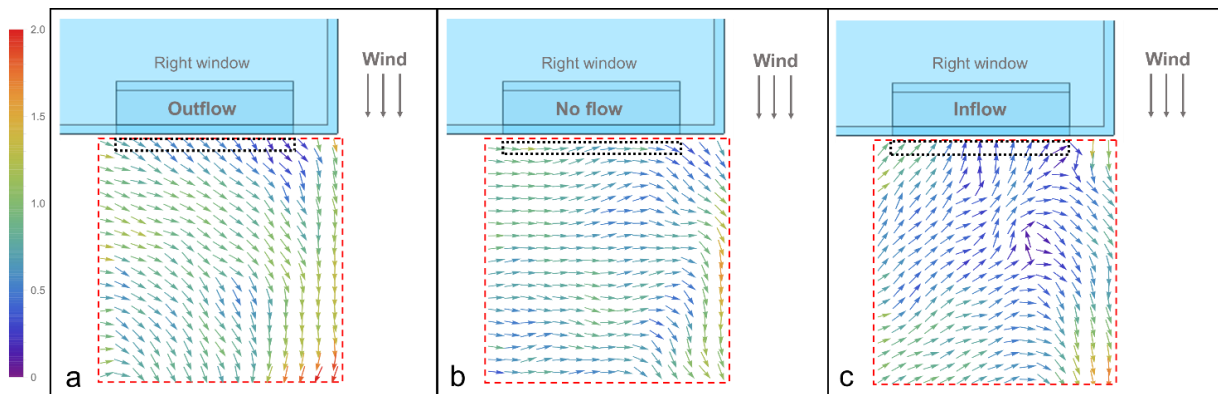
Figure 4.10 – Horizontal velocity flow field from PIV measurement. (a) – outflow through the right window; (b) – transition period where no significant flow exists; (c) – inflow through the right window.

The PIV data had to be processed to allow direct comparison with the HWA data. The PIV velocity profile shown in Figure 4.11 was created by averaging, in each time step, the normal velocity values in the line of data points that is adjacent to the window (the points inside the black dotted rectangle shown in Figure 4.10). The resulting average normal velocity is plotted in Figure 4.11(b). Comparing this PIV velocity profile with the HWA velocity profile obtained using the method described in Chapter 4.4.3.1 (Figure 4.11(a)), reveals significant similarities, as expected.

82
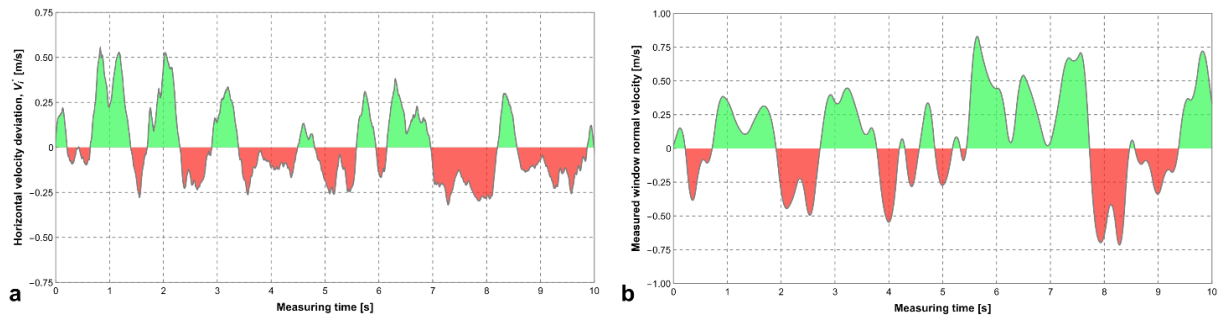
Figure 4.11 – Velocity measurements: (a) – horizontal velocity deviation (HWA); (b) – Window normal velocity (PIV).

4.5.4. Frequency of vortex shedding

To obtain the vortex shedding frequency (f_s) we used two methods:

- From smoke visualization, f_s was obtained by counting the number of outflows in each window during a 25 s visualization period.
- From the HWA and PIV, f_s was obtained by counting the number of inflection points during 10s measurement periods.

Table 4.2 shows the experimentally determined shedding frequencies with the corresponding *Strouhal* (from Eq.(4.1)). In the calculation, U_∞ was considered equal to the wind velocity at building height [16]. Given the similarities of the measured results (presented in Table 4.2), obtained using three independent methods and their agreement with literature (cf. Table 4.1), we can conclude that, for square shaped buildings all three methods are adequate. In this context we decided to use the average value of all the experimental measurements to reduce overall error. The average shedding frequency obtained was 0.79 Hz and the average *Strouhal* number is 0.101.

Table 4.2 – Measured values of shedding frequency (f_s) and Strouhal number (St).

	f_s [Hz]	St [-]
Smoke	0.72	0.093
HWA	0.80	0.103
PIV	0.84	0.108
Experimental	**0.79**	**0.101**

4.6. Numerical simulations: LES vs URANS

4.6.1. Computational domain and mesh

The numerical simulations used a commercial software package [138]. The simulation model had the same scale as the wind tunnel model and the computational domain has the dimensions recommended by the CFD best practice guidelines [139]. The top of the domain was 5H above the top of the model and the side boundaries. The inlet was set at a distance 3H upstream of the building to avoid streamwise gradients in the artificial ABL profile [140]. Finally, an outlet was located 15H from the back of the model. As shown in Figure 4.12(a), the total dimensions of the domain are 4.95(W) x 8.55(L) x 2.70(H) m^3.

The computational grids used in both LES and URANS simulations were based on a mixture of different cell geometries (see Figure 4.12(b), non-tetrahedral mesh). The mesh mixed prismatic, polyhedral and hexahedral cells while avoiding the highly skewed cells of tetrahedral meshes. The LES mesh had a minimum cell volume of 6.0×10^{-12} m^3 and a maximum cell volume of 2.1×10^{-3} m^3. With more than 45000 cells in the cross section of each window and hundreds of thousands of cells in the downstream vicinity of the model, the pumping mechanism was properly resolved at the windows, as well as the unstable development of the shear layers that drives the flow. The cells growth rate (cell size increases with distance from wall) was imposed to be less than 1.2. The total number of cells for each LES simulation was around 1.7 million. The LES approach used in this study does not use a near wall treatment and, therefore, must use a very fine grid near the external building surfaces. For LES, Georgiadis et al. [141] recommended that the first grid cell should be inside the viscous sublayer (dimensionless wall distance, $y^+ < 1$). Previous LES applications in wind engineering studies have adopted less stringent requirements in order to keep simulation time within feasible limits (with an average y^+ of 5 in [124], and 2.3 in [142]). In this study, the mean value of y^+ for the first cell was 0.9 for the back façade and 1.7 at the front, side, and top façades. Even with this optimized grid, each LES simulation took, approximately, 4 weeks in a 16-core workstation running a parallel version of ANSYS Fluent 19.2 [138].

The URANS simulations used two different meshes labeled normal and refined. The normal meshes have a minimum cell volume of 5.6×10^{-9} m^3, a maximum cell volume of 4.1×10^{-3} m^3 and more than 150 cells in the cross section of each window, with a growth rate imposed to be less than 1.2. The number of cells for each normal mesh case is around 375,000 cells. The refined meshes had a minimum volume of 3.5×10^{-11} m^3, a maximum of 3.1×10^{-3} m^3 and more

than 350 cells in the cross section of each window. The number of cells for each URANS case was around 876,000 cells.
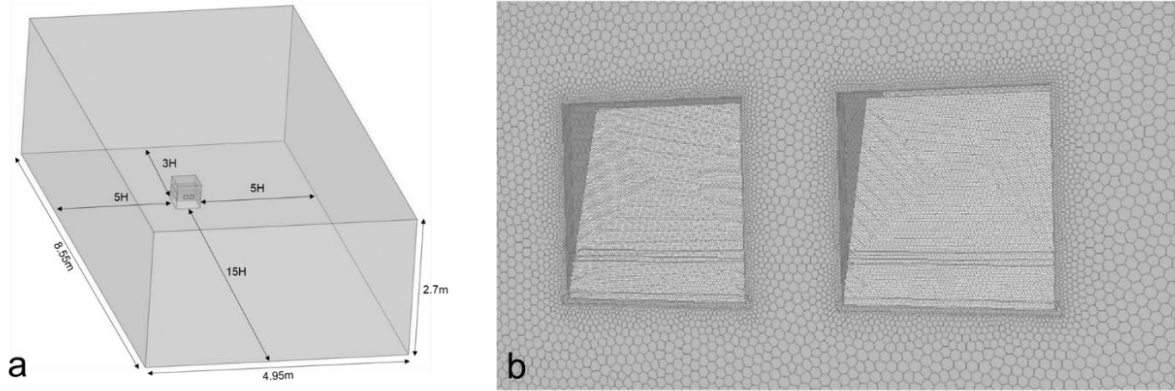
Figure 4.12 – (a) Domain dimensions; (b) Close view of the window's mesh for a separation s'=0.25.

4.6.2. Boundary conditions

The inlet boundary conditions were based on the measured ABL profile from the wind tunnel experiments, particularly the mean streamwise wind velocity, U, and its turbulence intensity, I_u. The inlet mean wind profile was constructed based on the log-law equation (Eq.(4.9)) [47], where u^*_{ABL} is the friction velocity, κ is the von Kármán constant with a value of 0.42 and z is the height above the ground. The aerodynamic roughness length, z_0, was determined by fitting the measured mean velocity profile with the logarithmic profile given in Eq.(4.9), resulting in $z_0 = 0.004$. The turbulent kinetic energy, k, is given by Eq.(4.10) and was obtained using the mean wind velocity and the streamwise turbulence intensity. Although, the parameter a in Eq.(4.10) normally ranges between 0.5 and 1.5, a value of 1.0 was chosen since it was considered the streamwise turbulent fluctuation of the wind was the same order of magnitude as the sum of both the transversal and vertical velocity fluctuations [46,143,144]. The dissipation rate, ε, was calculated through Eq.(4.11) [47] and, for the SST k-ω turbulence model, the specific dissipation rate, ω, is given by Eq.(4.12) [143], where the C_μ is a model empirical constant set to 0.09. For the LES simulations, an artificial time-dependent inlet condition was set to introduce periodic perturbations on the mean wind velocity profile; the vortex method was chosen with a number of vortices of 190 [49].

$$U(z) = \frac{u^*_{ABL}}{\kappa} \ln\left(\frac{z + z_0}{z_0}\right) \tag{4.9}$$

$$k(z) = a(U(z)I_u(z))^2 \tag{4.10}$$

$$\varepsilon(z) = \frac{(u^*_{ABL})^3}{\kappa(z + z_0)} \tag{4.11}$$

$$\omega(z) = \frac{\varepsilon(z)}{C_\mu k(z)} \tag{4.12}$$

The outlet plane had a zero static pressure boundary condition. Both the sides and top boundaries were set to have a zero normal velocity condition and zero normal gradients to the remaining flow variables. The model surfaces and the ground of the domain were defined as stationary smooth walls with the no-slip velocity condition; the equivalent sand-grain roughness height, k_s, was set to 0 m; and a zero-diffusive flux condition for the pollutant species was imposed. During the simulations, a constant volumetric source of CO_2 pollutant was set within the measured room with a steady flux of 8.2×10^{-5} kg/(m^3.s).

As suggested by [46], a preliminary simulation was performed to compare the incident wind profile at the building location with the imposed wind profile at the inlet using Eqs.(4.9)-(4.12). Figure 4.13(a) compares the wind tunnel boundary layer, that follows a power-law, with the inlet log-law wind profile. Figure 4.13(a) also shows that the structure of the incident wind profiles from LES and URANS are preserved within an empty domain. Figure 4.13(b) provides a schematic view of the computational domain with indication of where the vertical incident profiles were measured.
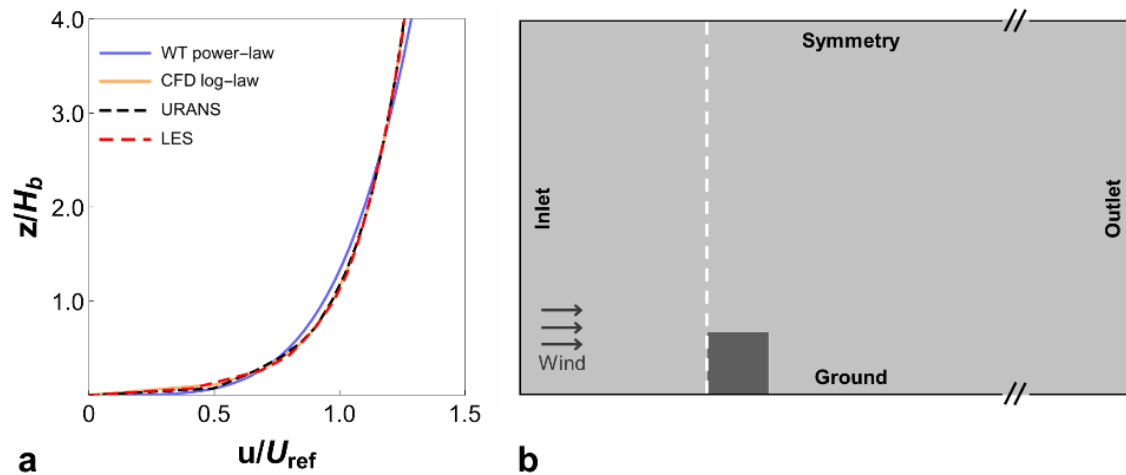
Figure 4.13 – Comparison of the experimental wind profile (power-law) and the imposed inlet wind profile (log-law) with the incident mean wind profiles of URANS and LES: a – normalized wind profiles; b – elevation view of the computational domain with the dashed line (white) indicating where vertical incident profiles were measured. (building shown only for illustrative purposes.)

4.6.3. Numerical methods

The LES simulations used the Smagorinsky-Lilly (SL) turbulence model with a dynamic subgrid-scale (DSGS) model for the filtering operation [145]. This combination of models was recently used to validate SS2 natural ventilation flows [146]. For the velocity-pressure coupling, the Pressure-Implicit with Splitting of Operators (PISO) scheme was used in combination with the Non-Iterative Time-Advancement (NITA) scheme. The convection terms had a bounded central differencing scheme and the pressure and CO_2 terms have a second order discretization schemes. A bounded second order implicit scheme was set as the transient formulation. The time step size 5×10^{-4} s, results in a maximum Courant–Friedrichs–Lewy (CFL) number that is always lower than one. The simulations ran for 200,000 timesteps, resulting in total simulation period of 100 s, more than 40 times the flow-through time (time it takes the flow to go through the entire computational domain). The minimum values for the scaled residuals were identical for the three LES simulations and were 10^{-6} for momentum and 10^{-5} for continuity and CO_2.

The URANS simulations use the SST k-ω turbulence model. This model was chosen due to its capacity to predict shedding frequencies, shown in a recent study [121]. The SIMPLE method was set to solve the velocity-pressure coupling equations. Both the turbulent kinetic energy and specific dissipation rate terms used a second-order discretization scheme. The remaining settings were similar to LES, however the number of timesteps was always higher than 400,000,

resulting in over 200 s of simulation period. The increase in the number of timesteps was due to the fact that URANS needed more time to reach full mixing and stabilized levels of CO_2 within the room (see chapter 4.6.4.2). The minimum values for the scaled residuals were 10^{-8} for momentum, 10^{-7} for k and ω, and 10^{-6} for continuity and CO_2.

4.6.4. CFD results

4.6.4.1. Shedding frequency

This study used two methods to obtain the shedding frequency:

- the vortices were observed in a post-processed animation of a horizontal plane at half height at the leeward of the active room;
- the shedding frequency was inferred using the bulk airflow time variation at one of the windows by counting the number of inflection points during the simulation.

Both methods produced the same shedding frequency results (f_s,). Figure 4.14 compares the measured and simulated profiles in terms of their general shape. Figure 4.14(a) shows the measured PIV non-dimensional velocity profile, while Figure 4.14(b) and (c) show the non-dimensional bulk airflow rate through one of the windows of the model during the last 10 simulation seconds of LES and URANS, respectively. The non-dimensional profiles were obtained dividing each profile by its maximum absolute value. The green and red zones show when there is inflow or outflow through the window. Comparing the three graphs in Figure 4.14, the measured and LES profiles have a similar shape. In contrast, URANS clearly cannot predict the unsteady velocity fluctuations induced by the shear layer instability at the back of the model. This is qualitative indication that URANS is not a suitable simulation approach for 3D pumping ventilation.
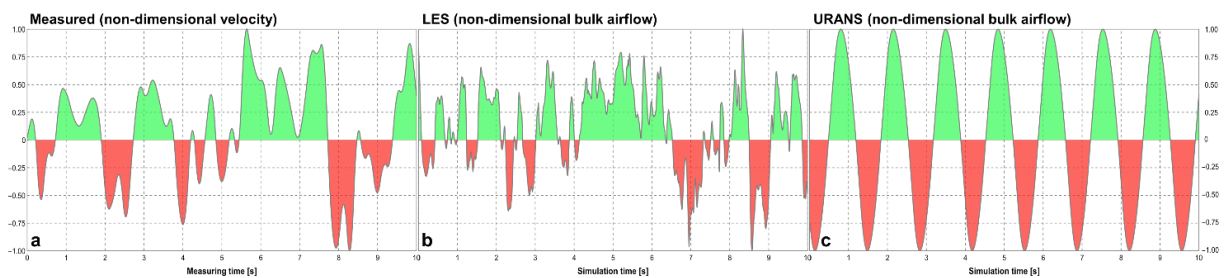
Figure 4.14 – Comparison between non-dimensional profiles from experimental and the numerical simulations: a – PIV; b – LES; c – URANS.

The average simulated shedding frequencies, f_s, and the corresponding *Strouhal* number are shown in Table 4.3. The results show both URANS and LES are able to predict the shedding frequency and are in agreement with the experimental measurements (5% error).

Table 4.3 – Comparison of the average of both the simulated shedding frequencies (f_s) and Strouhal numbers (St) with the literature and the average from the experimental results.

	f_s [Hz]	St [-]
Literature review		0.09–0.12
WT (PIV and HWA)	0.79	0.101
URANS	0.75	0.096
LES	0.74	0.095

In addition, the flow pattern of both LES and URANS was compared with the PIV velocity measurements. For the same area of interest used in PIV measurements, Figure 4.15 shows the flow patterns for the three moments of the pumping ventilation cycle. The results demonstrate that LES is able to accurately reproduce the velocity fluctuations at the window, while URANS reveals limitations in capturing the air exchange over the ventilation cycle.
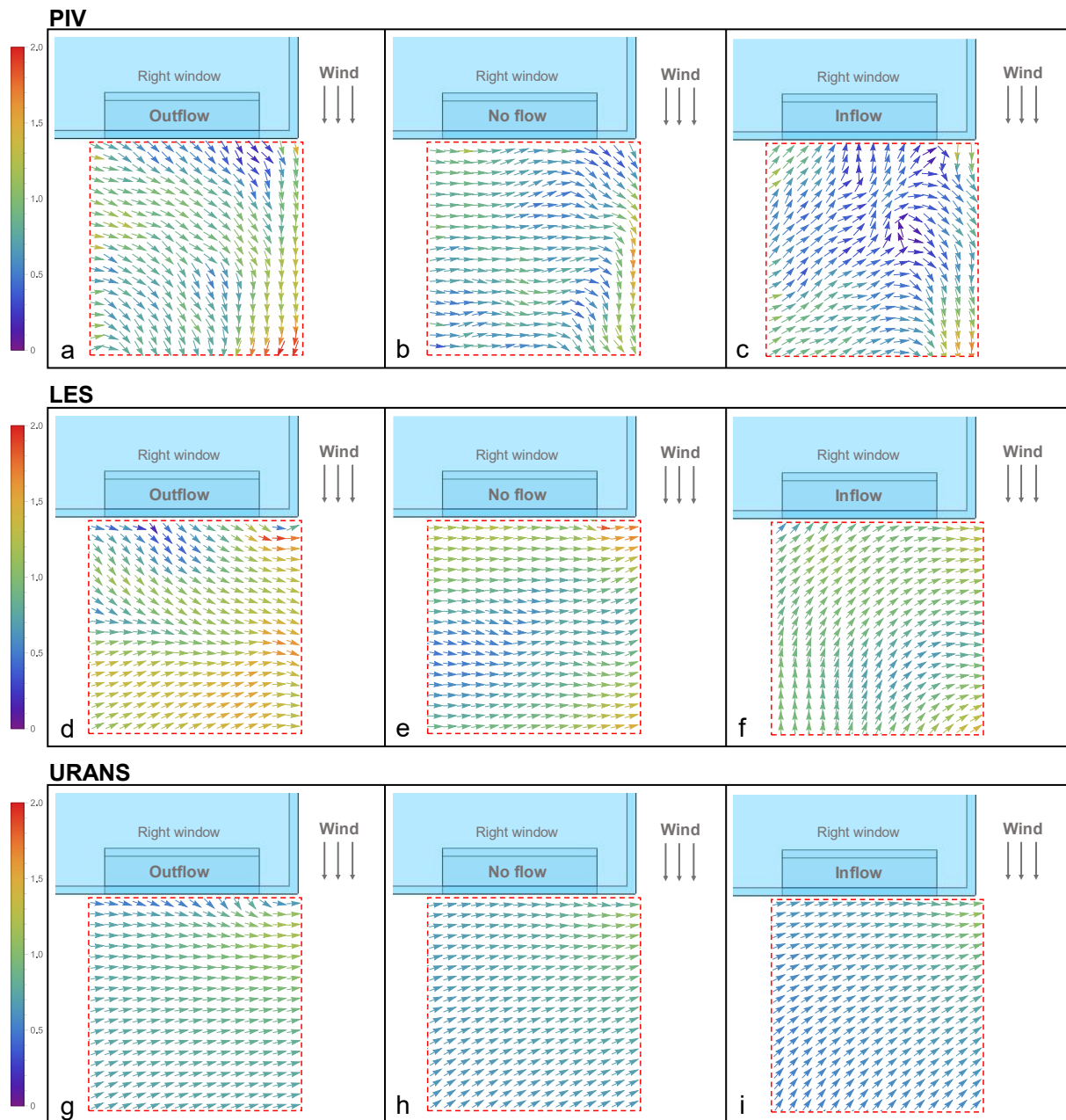
Figure 4.15 – Horizontal velocity flow field of the pumping ventilation cycle from: PIV measurement (a, b and c); LES (d, e and f); and URANS (g, h and i).

4.6.4.2. Effective and bulk ventilation rate

The effective ventilation rate was predicted using constant uniform pollutant release rate in the room [52]. Once full mixing and stabilized CO_2 concentrations were achieved in each simulation, the effective ventilation rate was calculated using simple tracer gas mass balance equation (Eq.(4.13)) [51]:

$$Q_{eff} = \frac{\dot{m}_{released}}{\overline{C}_{room}} \tag{4.13}$$

where Q_{eff} is the effective ventilation rate [m³/s], $\dot{m}_{released}$ is the constant CO_2 flow rate [mg/s] released during the simulation, $\overline{C}_{room}$ is the average CO_2 concentration level [mg/m³] measured in the same location of the sampling points of the wind tunnel measurements. Each simulation was stopped after the predicted interior mean CO_2 concentration had stabilized for several simulation seconds. Typical running times were 100 and 200 simulation seconds for LES and URANS, respectively, and the average predicted effective air change rates were 67.5 air changes per hour [ach]. Figure 4.16, shows a comparison between the simulated and measured effective ventilation rates.
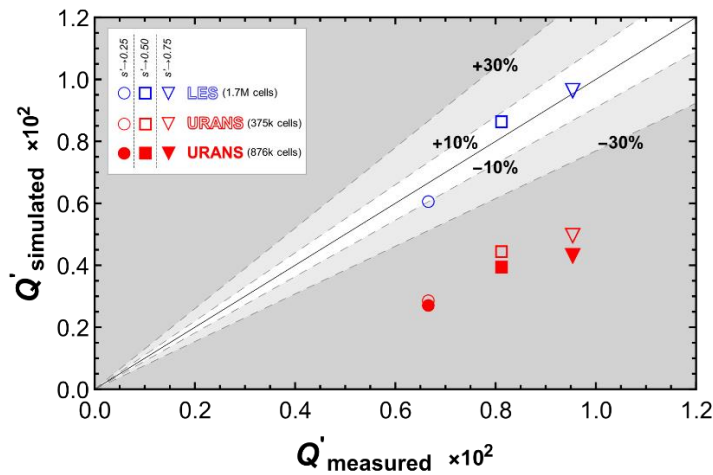
Figure 4.16 – Comparison of non-dimensional effective ventilation rate between wind tunnel experimental measurements and the numerical simulations: LES (blue) and the two URANS meshes (red).

LES simulation results for the three simulated cases show an error of 10% or less. For the cases $s'=0.25$, $s'=0.50$ and $s'=0.75$ the errors were -8%, +6% and -1%, respectively. Although URANS was able to predict the trend of increased ventilation rate with increased s', it was unable to predict the magnitude of the ventilation rate. URANS persistently underpredicts the ventilation rate by more than 40% in both meshes used (as suggested by Figure 4.15(g) and (i)).

$$\varepsilon_v = \frac{Q_{eff}}{Q_{bulk}} \tag{4.14}$$

91

The LES simulations were also used to calculate the ventilation efficiency (ε_v) for the three window separations used (Eq.(4.14)). The bulk ventilation rate is the total airflow through the windows, measured in control surfaces in each window. The results show that pumping ventilation airflow has a ventilation efficiency that ranges between 0.60 and 0.75 (see Table 4.4). As expected, the window geometry with higher separation (0.75) has higher ventilation efficiency.

Table 4.4 – Variation of the ventilation efficiency of pumping ventilation with window separation.

Window separation, s'	Ventilation efficiency, ε_v
0.25	0.60
0.50	0.60
0.75	0.75

4.7. Discussion

The wind tunnel measurements presented in this study show that, for the three cases studied, the effective ventilation rate increases linearly with the window separation (s'). This result is different from the other existing wind tunnel based study that proposed a $s'^{1/2}$ increase [16]. When analyzing this difference, one should note that the experimental setup used in the present study is superior to the setup in [16]: it uses a bigger model (1/20 scale versus 1/70) with partially open windows and 15 uniformly spaced CO_2 sampling points (versus 2 [16]). It is also important to note that there are only four 3D studies of pumping ventilation: two experimental ([16] and the present study), and two validated LES studies ([118] and the present study). Currently, three of the four existing 3D studies point towards a linear dependence.

The experimental and LES numerical results of this study indicate that window separation does not affect the vortex shedding. This result is a direct manifestation of the large momentum flux discrepancy that exists in these flows: the momentum flux of the pumping ventilation flow is several orders of magnitude lower than the main external wind flow. Therefore, vortex shedding, and its frequency, depend only on the geometry of the building, the resulting shear layer separation and the upstream flow velocity, as indicated in Eqs.(4.1) and (4.2). In spite of its relative weakness, observation of dynamic smoke removal and CO_2 concentration variation in the room shows that pumping ventilation occurs in the whole room (and not merely to the regions near the windows).

The results of this chapter may still be valid for any large room that occupies the full width of a small and isolated building, ventilated by two windows with a variable separation between each other. However, the room may not occupy the full depth of the building, as long as the windows face the leeward side.

This study used steady incoming wind. The expected impact of wind gusts aligned with the mean wind, i.e., normal to the front façade of the building, is to increase the wind generated pressure and vortex shedding frequency. As a result, the pumping ventilation flowrate is also expected to increase. For wind gusts that are not aligned with the mean wind flow direction the scenario is less clear and more research is needed. Other limitations in this study include the geometry (only one type of window and building shape) and the limited number of CFD approaches used, in particular the exclusion of hybrid RANS-LES models (or detached eddy simulation, DES).

4.8. Conclusions

The present study presents a detailed experimental dataset of pumping ventilation flow. The average vortex shedding frequency was measured using three independent methods (smoke visualization, HWA and PIV). As shown in Figure 4.11, 3D pumping ventilation is unstable but displays a periodic behavior over several oscillation cycles. The measured average oscillation frequency implies a *Strouhal* number of 0.10, a value in-line with existing experimental and numerical studies. The experimental results confirm that pumping ventilation flowrate increases with window separation. Further, this study revealed an approximately linear relation between effective flowrate and window separation (Figure 4.9).

This study also evaluated the capability of commonly used numerical simulation approaches (LES and URANS) to predict pumping ventilation. The simulated *Strouhal* numbers were in agreement with the experimental measurements (5% error). However, observation of Figure 4.14 reveals that while LES is able to simulate the inherent instability of the flow, URANS fails to capture this fundamental feature. Further, LES is able to predict the effective flow rates with a mean absolute error of 5%. The validated LES simulations allowed for an analysis of the impact of window separation in the ventilation effectiveness, revealing a ventilation efficiency of 0.60 that increases to 0.75 in the case with higher window separation. URANS consistently underpredicts the effective flow rates (errors of 40% or more, shown in Figure 4.16). In light of these results the authors conclude that LES may be a suitable simulation approach for pumping ventilation. In contrast, the results of this study show that URANS is an inadequate approach to study pumping ventilation.

5. CORNER VENTILATION

5.1. Nomenclature

Symbols

$\overline{\Delta p}$	mean pressure difference [Pa]
$\left|\overline{\Delta C_p}\right|$	steady (mean) pressure coefficient difference [-]
$\Delta C_{p_{amp}}$	unsteady (amplitude of fluctuations) pressure coefficient difference [-]
$\Delta C_{p_{rms}}$	unsteady (root mean square of the fluctuations) pressure coefficient difference [-]
α	power law coefficient [-]
α_υ	model constant of LES_{IQ} [-]
θ	deviation from the perfect wind alignment [º]
θ_{CR2}	limit wind incident angle for CR2 pumping ventilation [º]
θ_{SS2}	limit wind incident angle for SS2 pumping ventilation [º]
ε	turbulent dissipation rate [m^2/s^3]
ε_v	ventilation efficiency [-]
$\varepsilon_{v_{cv}}$	ventilation efficiency for CR2 CV flows [-]
ε_{v_p}	ventilation efficiency for CR2 pumping flows [-]
κ	von Kármán constant [-]
ρ	air density [kg/m^3]
υ	molecular viscosity [kg/m.s]
$\upsilon_{t,SGS}$	turbulent viscosity [kg/m.s]
A_{eff}	effective opening area [m^2]
$C(t_j)$	CO_2 concentration at time t_j [mg/m^3]
C_{bg}	background CO_2 concentration [mg/m^3]
C_d	discharge coefficient [-]

$\overline{C_p}$	steady (mean) pressure coefficient [-]
$C_{p_{rms}}$	unsteady (root mean square of the fluctuations) pressure coefficient [-]
D	depth [m]
FAC1.3	deviation by a factor of 1.3 [-]
FAC2	deviation by a factor of two [-]
FB	fractional bias [-]
H	height [m]
H_B	height of the building [m]
I_u	turbulence intensity [-]
$I_u(z)$	turbulence intensity at a given height, z [-]
k	turbulent kinetic energy [m^2/s^2]
k_s	equivalent sand-grain roughness height [m]
LES_{IQ}	mesh quality index for LES [-]
MPE	Mean percentage error [-]
n	total number of measured points or model constant of LES$_{IQ}$ [-]
NMSE	Normalized mean square error [-]
$\bar{p}$	mean static pressure [Pa]
p_{rms}	root mean square of the static pressure fluctuations [Pa]
Q_{bulk}	bulk ventilation rate [m³/s]
Q_{eff}	effective ventilation rate [m³/s]
Q_{bulk}'	normalized effective ventilation rate [-]
Q_{eff}'	normalized effective ventilation rate [-]
$Q_{eff\,CR2}'$	normalized effective ventilation rate for CR2 rooms [-]
Re	Reynolds number [-]
s	distance between the geometric center points of the windows [m]
s'	dimensionless window separation [-]

t_j	elapsed time since the initial time of the decay curve [h]
u^*_{ABL}	friction velocity [m/s]
U	mean streamwise wind velocity [m/s]
$U(z)$	wind velocity at a given height, z [m/s]
U_H	velocity at building's height [m/s]
U_{ref}	reference wind velocity [m/s]
V_{room}	volume of the active room [m^3]
W	width [m]
z	height to the ground [m]
z_0	aerodynamic roughness length [m]

Acronyms

3D	three-dimensional
ABL	atmospheric boundary layer
CFD	computational fluid dynamics
CFL	Courant–Friedrichs–Lewy
CO$_2$	carbon dioxide
CR	corner ventilation
CR2	corner ventilation with two openings
CV	cross-ventilation
DSGS	dynamic subgrid-scale
LES	large eddy simulation
NITA	non-iterative time-advancement
NV	natural ventilation
PISO	pressure-implicit with splitting of operators
SL	Smagorinsky-Lilly

SS   single sided ventilation

SS2   single sided ventilation with two openings

URANS   unsteady Reynolds-averaged Navier-Stokes

WT   wind tunnel

5.2. Introduction

In the service industry, individual corner offices are often a symbol of career achievement [147]. These rooms are also special in terms of daylighting and natural ventilation (NV) capabilities due to the possibility for natural light and fresh outdoor air ingress through two perpendicular facades. This chapter presents the first experimental and numerical simulation study of NV in corner rooms, an NV flow geometry that is commonly referred to as corner ventilation (CR) [148].

NV can be driven by wind, stack (buoyancy), or a combination of both. Buoyancy is, typically, the most important driving force in dense urban environments. In contrast, for isolated buildings located in wind exposed locations, even a moderate wind can overcome buoyancy forces. This propensity for wind dominated flows can be seen by considering a room with an average indoor temperature 8 °C higher than outdoors and a generous 3m height difference between inflow and outflow openings. For this configuration, buoyancy generates a flow driving pressure of 1 Pa, a value that is exceeded by a rather low incoming wind speed of 2 m/s [6].

This chapter focuses on wind driven NV of isolated rectangular buildings with CR2 and SS2 rooms. Isolated buildings exposed to wind create flow separation over a substantial part of the leeward building surfaces. This flow separation creates a wake region surrounded by shear layers [23] whose unstable interaction generates a Karman vortex street [25] and drives alternating natural ventilation pumping airflow [6]. Pumping ventilation is a 3D flow mechanism that has been studied in atmospheric boundary layer (ABL) wind tunnels (WT) [16,26].

So far, pumping ventilation has been observed in SS2 rooms (see Figure 5.1(a) and (b)), and it can be expected that, for incoming wind aligned with the room corner, it may also occur in CR rooms. In addition to this possibility, there is also an interesting question about the sensitivity of pumping ventilation to the incoming wind angle. Natural wind continuously varies in intensity and direction, in contrast with the artificial wind used in WTs that has steady velocity

and direction. In this context, it is important to investigate the occurrence of pumping ventilation for wind angles that are not perfectly perpendicular to the façades or building corners. If pumping ventilation was to require a perfectly aligned incoming wind, then there would be very limited applications of this flow driving mechanism outside the WT.

Figure 5.1(c) illustrates a possible building floor configuration with multiple SS2 and CR2 rooms where pumping ventilation may occur for, at least, the four cardinal and four intercardinal incoming wind directions. The possibility that will be explored in this chapter is that pumping occurs in CR2 rooms and, further, for each of the two room geometries (SS2 or CR2), pumping also occurs for an incoming wind angle range of $\pm\theta$, where θ is the deviation from perfect alignment (perpendicular to façade wind for SS2 rooms, i.e., green lines in Figure 5.1(c), and wind aligned with the corner of the building for the CR2 rooms, i.e., blue lines). Beyond this transition angle, the flow is expected to change to a CV-like flow, already observed in SS2 ventilation [16]. In SS2 rooms, whenever there is a steady static pressure difference between the openings, the flow will travel between the openings in a "cross-sided" ventilation pattern. This experimental evidence indicates that the traditional airflow regime classification discussed above is limited; reality is blurrier and CV-like airflow behavior can occur in SS2 rooms and even more clearly in CR2 rooms as air flows unidirectionally from inflow to outflow openings.
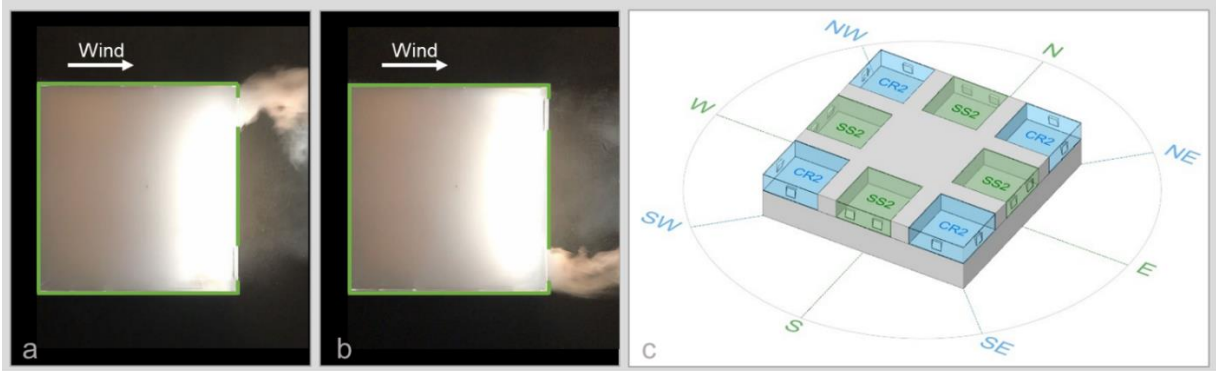
Figure 5.1 – (a) and (b): Oscillatory pumping mechanism in a SS2 cubic building; (c): Building model with multiple CR2 and SS2 rooms.

Existing research that is relevant for the work presented in this chapter ranges from simplified models of SS ventilation that incorporate the effects of unsteady wind generated pressure to WT studies of pumping ventilation. Chu et al. [116] proposed a simplified model to predict airflow rates in SS2 flows that considers the effects of fluctuating pressure through a

modification of the orifice equation. The model development was based on WT experiments of an isolated single room building exposed to variable incoming wind direction from 0º (openings located at the windward façade) to 180º. Results show that, for wind directions of 0º or between 67.5º–180º, the time-averaged pressure difference is negligible, and the fluctuating pressure dominates. Daish et al. [16] performed WT measurement of the ventilation rate in a single isolated room with two planar openings (SS2). This work identified pumping ventilation and shear layer instability as a new NV flow driving mechanism, and a simplified model to predict the ventilation rate of SS2 flows was proposed. The model was based on the steady and unsteady pressure components, with those components re-expressed in terms of available independent parameters, such as opening separation and incoming wind angle. King et al. [117] performed computational fluid dynamics (CFD) using large eddy simulation (LES) and a lattice-Boltzmann method to study the CV flow driven by wind perpendicular or parallel to the ventilation openings, and pumping mechanism was found in the latter. Kobayashi et. al [118] used LES to study the ventilation rate of a 3D cubic model with SS2 and CV configurations. A simplified model was suggested, based on the orifice equation, which predicts the ventilation rate of SS2 and CV with less than 30% error. The authors of this paper [26] presented a comprehensive WT study of pumping, using smoke visualization, hot wire anemometry, and particle image velocimetry, in a three-story building with partially opened windows. Results of numerical simulations of the WT experiments showed that URANS is unsuitable to simulate pumping ventilation, while LES may be a suitable simulation methodology. There are no existing studies of CR ventilation and only a limited number of studies of pumping NV. Still, Corner NV is discussed in the recently revised ANSI/ASHRAE Standard 62.1-2019 [148].

This chapter addresses several research questions in corner and pumping ventilation by presenting the first experimental observations of pumping ventilation in corner rooms and the first study of the incoming wind angle limits of pumping ventilation. Using a combination of WT measurements and numerical simulations, it is developed a simple formula-based model that can predict the CR2 effective ventilation rate from wind induced pressures and opening sizes. The proposed model is suitable for integration in building dynamic thermal simulation tools such as EnergyPlus [58]. This chapter has the following four objectives:

1. Determine the range of incoming wind angles for which NV pumping occurs in SS2 and CR2 rooms of wind exposed rectangular buildings.
2. Measure the effective NV flowrate in CR2 rooms of wind exposed buildings for 16 incoming wind directions.
3. Investigate the role of steady and unsteady wind generated pressures in CR2 rooms.
4. Develop a simplified model to predict effective airflow in CR2 rooms that can use pressure data from LES simulations or WT measurements.

The WT experiments use a relatively large-scale, 1/20, building model that allows for the inclusion of partially open windows (bottom-hung). Smoke was used to visualize the alternating pumping ventilation airflow. Effective airflow measurements were performed to investigate the impact of wind direction on the pumping ventilation flow in SS2 and CR2 rooms. Validated numerical LES external airflow simulations were used to predict wind generated pressures that are used in the simplified model. This chapter continues with a description of the WT experiments in Chapter 5.3. Chapter 5.4 describes the LES numerical simulation models used. Chapters 5.5 and 5.6 present the results of the WT experiments and the numerical simulations, respectively. Chapter 5.7 presents a simplified model for CR2 that is based on the aperture equation. Finally, Chapter 5.8 summarizes the main conclusions.

5.3. Wind tunnel experiments

The wind tunnel experiments performed had three interrelated objectives. The first was to obtain the first experimental observations of pumping ventilation in CR2 rooms. The second was to obtain the range of incoming wind angles for which NV pumping occurs in SS2 and CR2 rooms of a wind exposed rectangular building. The third was to measure the effective NV flowrate in CR2 rooms for a large set of incoming wind directions.

5.3.1. Experimental facility

The experiments were performed in the Gävle University (HiG, Sweden) closed-circuit WT. This facility has a test section with 3 m (width) and 1.5 m (height) and adjustable air velocity (from 0.5 m/s to 27 m/s). The WT air temperature is controlled by a dedicated air handling unit with heating and cooling capacity that ensures isothermal measurement conditions. The tunnel uses a scaled representation of the atmospheric boundary layer (ABL, Figure 5.2(a)). The ABL profile is created by two sets of obstructions/roughness at the upstream region of the test section

(cf. Figure 5.2(a)). The resulting incident wind velocity profile follows closely the power-law shown in Eq.(5.1), where: $U(z)$ is the streamwise velocity at a given height [m/s], H_B is the height of the building relative to the WT floor (=45 cm), U_{H_B} is the velocity at building height ($\approx$3.5 m/s), z is the height to the WT floor [m], and α is the power law coefficient (=0.26, the typical roughness of residential suburbs and small towns [89]). Figure 5.2(b) shows the measured wind velocity and turbulence intensity (I_u) profiles of the ABL, as well as the power-law wind profile predicted using Eq.(5.1):

$$\frac{U(z)}{U_{H_B}} = \left(\frac{z}{H_B}\right)^{\alpha} \qquad (5.1)$$
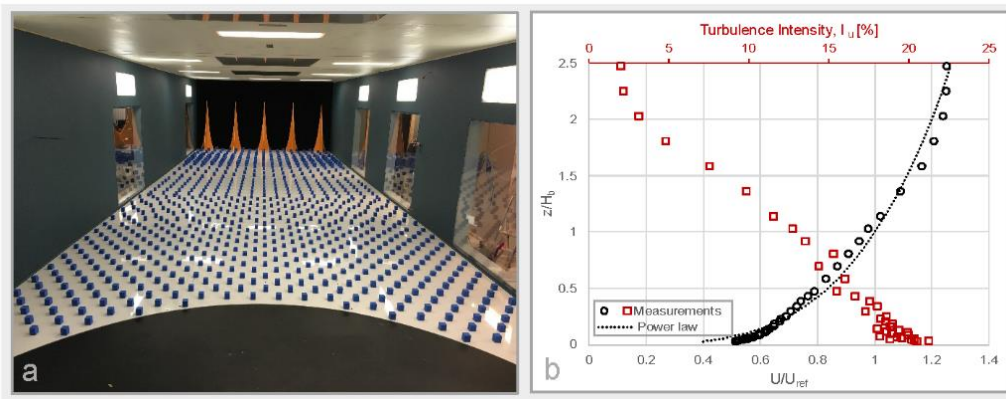
Figure 5.2 – (a) Setup of the roughness elements in the upstream zone of the WT; (b) measurements of the WT ABL profile and the fitting power-law for the velocity profile, predicted by Eq.(5.1) (black circles – measured wind velocity; red square – measured turbulence intensity; black dashed line – power-law wind profile).

The turbulent intensity in a real ABL usually varies from 30%–40% at ground level to 5%–8% at gradient height (height above the ground where the friction due to the urban environment has a negligible effect on the wind speed) [90,91,92]. In Figure 5.2(b), one may observe that the turbulent intensity across the plain opening is around 15%, which agrees well with the typical values of a real ABL.

5.3.2. Building models

The experiments used two 1/20 scale three-story building models for CR2 and SS2 analysis. Both models included the same ventilated model room with CO_2 injection and sampling capabilities. This room had a floor to ceiling height of 0.15 m and is placed in the middle floor

of each model, occupying an entire floor of the SS2 building and a fraction of the middle floor area of the CR2 building (cf. Figure 5.3). The active room had 4 mm thickness Plexiglass walls and the remaining components of the building models used opaque wooden boxes. Each bottom-hung window (also made of Plexiglass) had dimensions 0.075 m height by 0.075 m width and was positioned at mid-height of the active room, tilted 14º inwards. The models had the following characteristics:

- CR2 building: narrow (rectangular) building with a CR2 room (see Figure 5.3(a)) with one opening in each of the perpendicular façades. The total model dimensions of the CR2 building were 0.75 m(W) × 0.60 m(D) × 0.45 m(H);
- SS2 building: cubic building, with a 0.45 m side and an SS2 room, shown in Figure 5.3(b).

For the SS2 building, the dimensionless window separation, *s'*, was defined as [16,26]:

$$s' = \frac{s}{W} \quad ,$$
(5.2)

where *s* is the distance between the geometric center points of the windows [m], and *W* is the width of the SS2 building [m]. This SS2 study used a window separation of ½.
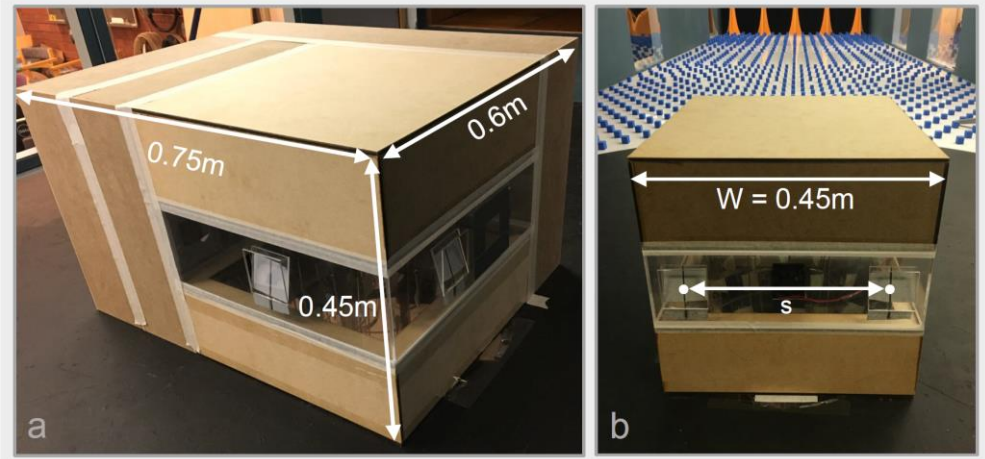
Figure 5.3 – Configuration of the models tested: (a) CR2 building; (b) SS2 building.

5.3.3. Smoke visualization

Previous studies [16,26] showed that smoke visualization can be used to identify the main flow features of pumping ventilation. All experiments began with wind aligned with the building corner for the CR2 building (blue dashed lines in Figure 5.4(a)) or perpendicular to the façade for the SS2 building (green dashed lines in Figure 5.4(b)). In the CR2 experiments, smoke was used to visualize pumping ventilation for wind aligned with the room corner and then determine the transition angle (red dashed lines in Figure 5.4(a)). In the SS2 experiments, smoke visualization was used to determine the incoming wind angle that marks the transition between pumping and cross-sided ventilation (red dashed lines in Figure 5.4(b)). In each experiment, the active room in the model was filled with smoke with the WT running and the resulting flow pattern was observed. After the model exhausted all the smoke, a +1° degree rotation was applied to the base and the experiment repeated until the observed airflow pattern transitioned from pumping to cross-sided ventilation (for SS2) and CV-like flow (for CR2). The transition criterion was then the absence of an oscillatory pumping flow. The last wind angle that displayed pumping flow was labelled θ_{SS2} (for SS2) and θ_{CR2} (for CR2). This procedure was also performed in the opposite rotation direction using decrements of -1°. Figure 5.4(c) illustrates the hypothetical pumping ventilation potential on the building model suggested in Figure 5.1(c), depending on the values of θ_{CR2} and θ_{SS2}.
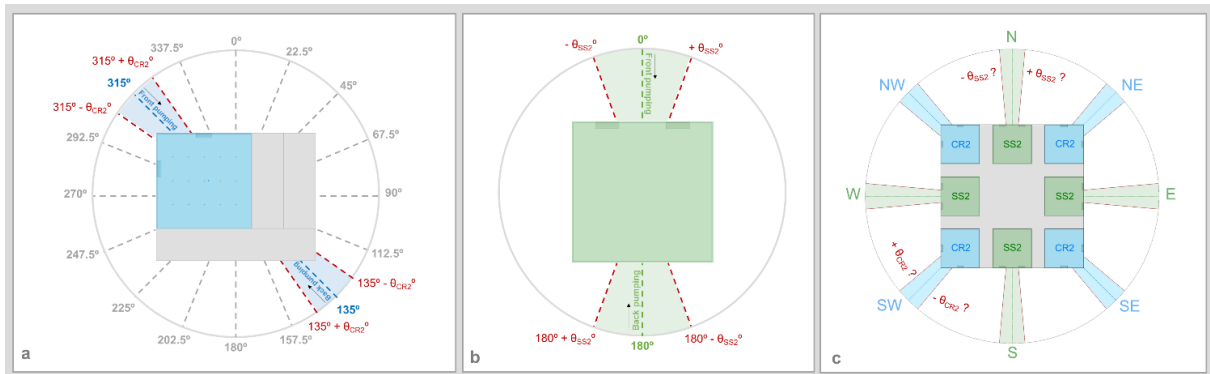
Figure 5.4 – (a) CR2 pumping potential based on θ_{CR2} (blue region); (b) SS2 pumping potential based on θ_{SS2} (green region); (c) Hypothetical pumping ventilation potential depending on θ_{CR2} and θ_{SS2}.

5.3.4. Measurement of effective ventilation rate

Effective ventilation rates were measured for both the CR2 and SS2 rooms. Using a tracer gas decay method, effective ventilation rates were measured for the following wind directions:

- sixteen regularly spaced wind angles for the CR2 room (from 0º to 337.5º with 22.5º intervals, as shown by the grey and blue dashed lines in Figure 5.4(a));
- and two wind angles, 0º and 180º (as shown by the green dashed lines in Figure 5.4(b)), where front and back SS2 pumping occurred.

In each measurement, carbon dioxide (CO_2) was injected in the active room of the model using a vertical rod with holes in various directions to ensure well-mixed conditions (see Figure 5.5). The CO_2 sampling system consisted of a grid of 15 evenly spaced CO_2 sampling points in the room at mid-height (sampling frequency of 20 Hz). The CO_2 concentration inside the WT was also measured. The effective ventilation rates were calculated using the time variation of the CO_2 concentration during the decay, that occurs after CO_2 injection is turned off, through Eq.(5.3) [5,26,52]:

$$Q_{eff} = \frac{(\sum_{j=1}^{n} t_j) \cdot \sum_{j=1}^{n} ln[C(t_j)-C_{bg}] - n \cdot \sum_{j=1}^{n} t_j \cdot ln[C(t_j)-C_{bg}]}{n \cdot \sum_{j=1}^{n} t_j^2 - (\sum_{j=1}^{n} t_j)^2} \times \frac{V_{room}}{3600} \qquad (5.3)$$

where Q_{eff} is the effective ventilation rate [m³/s], t_j is the elapsed time since the initial time of the decay curve [h] and $C(t_j)$ the CO_2 concentration at that time [mg/m³], n is the total number of measured points during the decay process, C_{bg} is the background CO_2 concentration, i.e., the CO_2 concentration inside the WT [mg/m³], and V_{room} is the volume of the active room [m³]. The setup used for the SS2 building was very similar to the abovementioned and its full description may be found in [26].
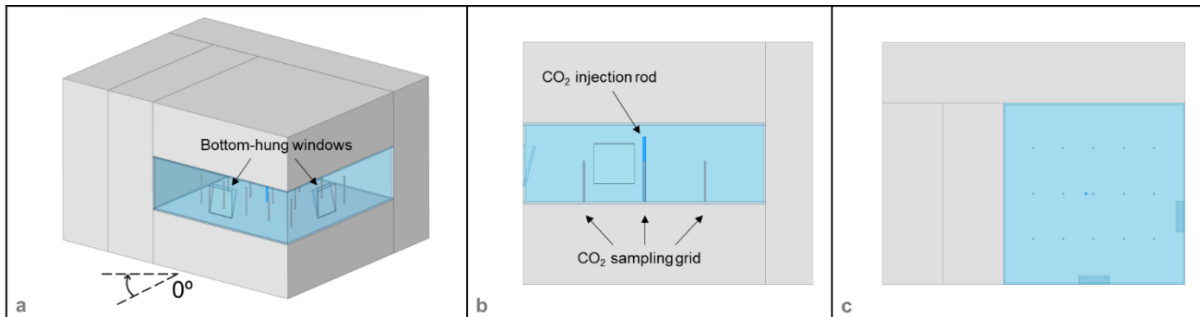
Figure 5.5 – Ventilation rate measurement setup of the CR2 building model: (a) the CR2 model; (b) CO2 sampling system and the injection point; (c) plan view of the active room including the sampling and CO2 injection points.

5.4. Large eddy simulations (LES)

This chapter presents the LES simulation models that will be used to predict steady and unsteady wind induced pressures in the ventilation openings of the two building models.

5.4.1. Computational domain and mesh

The numerical simulations were performed in the commercial software package ANSYS Fluent 19.2 [138] using CFD best practice guidelines [46,139]. Two computational models were constructed with the exact dimensions of each building model. The top and downstream boundaries of the computational domain were located at 5H and 15H away from the model, respectively (where H is the building height, [139]). The upstream boundary was set at a distance of 3H from the building to avoid streamwise gradients in the artificial ABL profile [46]. The domain of the CR2 building had 5.6 (W) $\times$ 8.6 (L) $\times$ 2.7 (H) m^3 (see Figure 5.6(a)), while the domain of the SS2 building had 4.95 (W) $\times$ 8.55 (L) $\times$ 2.70 (H) m^3. Both simulation geometries had a directional blockage ratio below 17% [46]. Due to convergence problems and increased truncation error [139], the use of tetrahedral meshes has been discouraged by CFD best practice guidelines. Consequently, the simulation model used a combination of cell geometries: prismatic; polyhedral; and hexahedral cells (see Figure 5.6(b)). The cells growth rate is set to less than 1.2. The CR2 and SS2 simulation domains had approximately 1.5 and 1.2 million cells, respectively. To reproduce the use of the active model as the middle floor during WT experiments, the simulated wind pressures were monitored at mid-height of each side wall of the building. Table 5.1 shows the wind incidence angles that were simulated for each building model.

Table 5.1 – Wind incident angles for the CR2 and SS2 buildings.

Active room	Wind angles
CR2	0º, 22.5º, …, 157.5º (22.5º increments)
SS2	0º
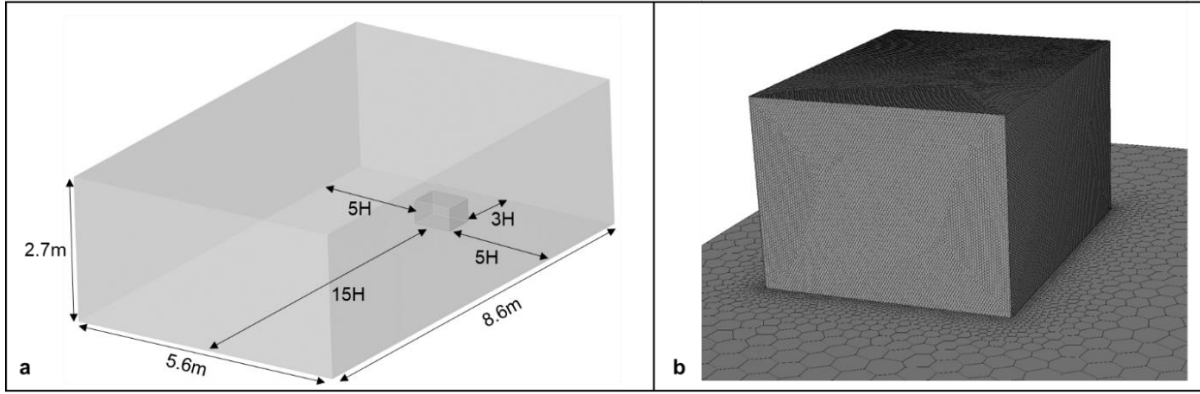
Figure 5.6 – (a) Domain dimensions for CR2 building model; (b) Closer view of the non-tetrahedral mesh at the façades.

The quality of the mesh was assessed using the LES$_{IQ}$ index [149]. This index assesses the fraction of the total turbulent kinetic energy that is resolved by the LES mesh:

$$LES_{IQ} = \frac{1}{1 + \alpha_v \left(\dfrac{v_{t,SGS} + v}{v} \right)^n} \tag{5.4}$$

where $v_{t,SGS}$ is the turbulent viscosity [kg/m.s], v is the molecular viscosity [kg/m.s], and the model constants (α_v, n) have values of 0.05 and 0.53. According to [149], an average LES$_{IQ}$ percentage of 75%-85% is an indicator of a good mesh resolution. For the simulations used in this chapter, the LES$_{IQ}$ volume average is 93%, with 99% of the computational domain above the 75% LES$_{IQ}$ threshold. LES models that include the near-wall region have the additional requirement of resolving 80% of the turbulent kinetic energy close to the walls [150]. Figure 5.7(a) and (b) show the 12 vertical locations close to walls of the CR2 simulation model where the LES$_{IQ}$ values were evaluated. The LES$_{IQ}$ results of each vertical line are shown in Figure 5.7(b), as well as the average of the 12 vertical lines (purple solid line). The average LES$_{IQ}$ above 80% indicates that the mesh used has adequate resolution near the walls.
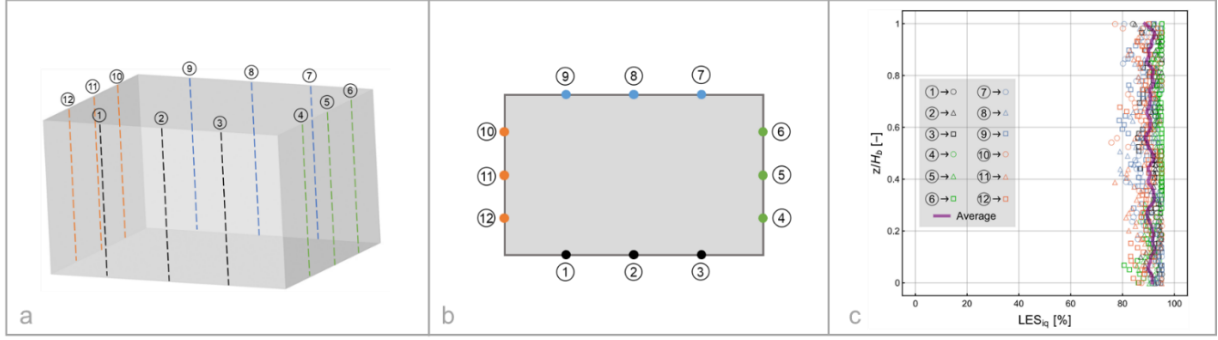
Figure 5.7 – (a) CR2 building model with the vertical lines where LES$_{IQ}$ near walls was assessed; (b) plan view of the CR2 building model; (c) LES$_{IQ}$ results for each vertical line and their average (purple solid line).

5.4.2. Boundary conditions

The inlet boundary conditions were fine-tuned to reproduce the ABL profile of the WT, particularly the mean streamwise wind velocity (U) and turbulence intensity (I_u). The inlet mean wind profile was based on the log-law equation (Eq.(5.5)) [47], where u^{*}_{ABL} is the friction velocity, κ is the von Kármán constant with a value of 0.42 and z is the height above the ground. The aerodynamic roughness length, z_0, is determined fitting the measured mean velocity profile with the logarithmic profile (Eq.(5.5), $z_0 = 0.004$). The turbulent kinetic energy, k, was obtained using the mean wind velocity and the streamwise turbulence intensity (Eq.(5.6)). The parameter a was set to 1.0, implying that the streamwise turbulent fluctuation of the wind is at the same order of magnitude of the sum of both the transversal and vertical turbulent fluctuations [26,143,144]. The turbulent dissipation rate, ε, is calculated using Eq.(5.7) [26,47]. LES simulations require an artificial time-dependent inlet condition to introduce periodic perturbations on the mean wind velocity profile. In the present case, these perturbations were generated using the vortex method, with 190 vortices [49,151].

$$U(z) = \frac{u^{*}_{ABL}}{\kappa} \ln\left(\frac{z + z_0}{z_0}\right) \tag{5.5}$$

$$k(z) = a \left(U(z)\, I_u(z)\right)^2 \tag{5.6}$$

$$\varepsilon(z) = \frac{\left(u^{*}_{ABL}\right)^3}{\kappa\,(z + z_0)} \tag{5.7}$$

The downstream boundary used a zero static pressure boundary condition. Both the lateral and top boundaries were set to have a zero normal velocity condition and zero normal gradients for the remaining flow variables. The model surfaces and the ground of the domain were defined as stationary smooth walls with the no-slip condition and a roughness height set to zero ($k_s = 0$ m). Following the suggestion in [46], a preliminary simulation was performed to compare the incident wind profile at the building location with the imposed wind profile at the inlet (defined by Eqs.(5.5)-(5.7)).

Figure 5.8(a) shows a comparison between the log-law wind profile imposed at the inlet with the incident wind profiles for the CR2 and SS2 computational domains. These results show that the structure of the incident wind profiles is preserved within the empty domains. Figure 5.8(b) provides a schematic view of the computational domain with a white vertical dashed line indicating where the incident profiles were obtained.
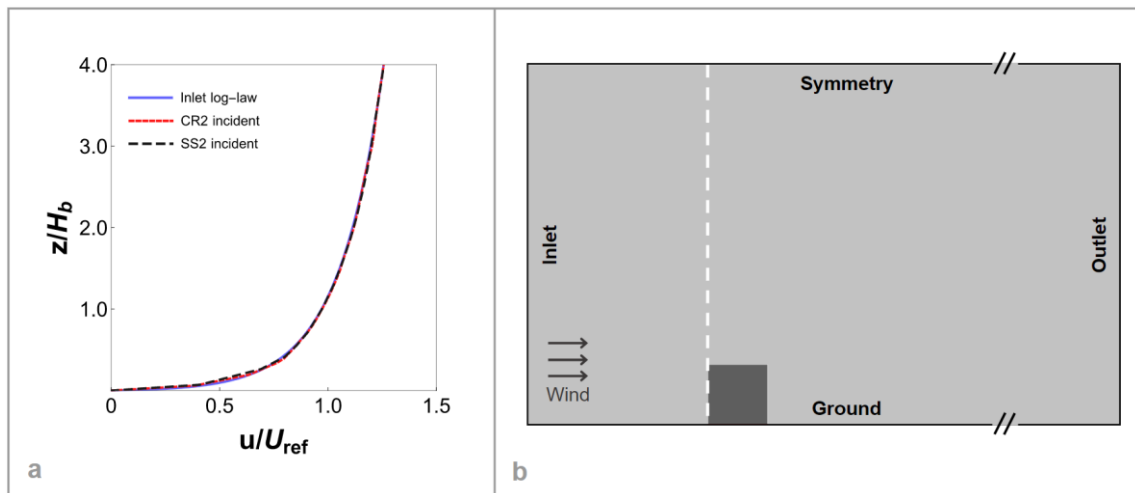
Figure 5.8 – (a) Comparison of the imposed inlet wind profile (log-law) with the incident mean wind profiles of CR2 and SS2 domains; (b) elevation view of the computational domain with the dashed line (white) indicating where vertical incident profiles were measured. (building shown for illustrative purposes only).

5.4.3. Numerical methods

The LES numerical simulations used the Smagorinsky-Lilly (SL) dynamic subgrid-scale (DSGS) closure method for the small-scale filtering operation [152], an approach that was recently validated for pumping SS2 NV flows [26,146]. The velocity-pressure coupling was performed using the Pressure-Implicit with Splitting of Operators (PISO) method in combination with Non-Iterative Time-Advancement (NITA). The convection terms used a bounded central differencing scheme while the pressure term used second-order discretization

schemes. A bounded second-order implicit scheme was set as the transient formulation. The simulation time step was 1×10^{-3} s, resulting in a maximum Courant–Friedrichs–Lewy (CFL) number that was lower than one in 98% of the domain. In each time step, the minimum values of the scaled residuals were less than 10^{-5} for momentum and 10^{-4} for continuity. The simulations ran for 60 000 timesteps, resulting in a total simulation real-time of 60 s (more than 24 times the domain flow-through time). Only the second half of the simulation period (30-60 s) was used in the analysis and statistical sampling.

5.4.4. Validation

The capability of the LES simulations to predict the steady and unsteady components of pressure coefficients in the walls of scaled building models was investigated using experimental data from [153,154,155], for square cylinders. The dimensions of the simulated square cylinder were 0.05 m × 0.05 m × 0.9 m (width × length × height). The computational domain had a square test section of 0.9 m with a length of 4.9 m. The square cylinder was centered along the width of the domain and positioned 1.35 m from the inlet plane. The air velocity at the inlet was constant with a value that matches the Reynolds number of the experiment (Re = 2×10^4). The boundaries of the top, bottom, and sides of the computational domain were set with the no-slip condition. At mid-height of each wall of the square cylinder, thirty equally distributed sampling points monitored the pressure over the active simulation period of 30 s. The initialization period of the simulation was 5 s. For the remaining simulation period (25 s), the steady $(\overline{C_p})$ and unsteady $(C_{p_{rms}})$ components of static pressure were converted into pressure coefficients using Eqs.(5.8)-(5.9):

$$\overline{C_p} = \frac{\overline{p}}{1/2 \, \rho \, U_{ref}^2} \tag{5.8}$$

$$C_{p_{rms}} = \frac{p_{rms}}{1/2 \, \rho \, U_{ref}^2} \tag{5.9}$$

where $\overline{p}$ is the mean static pressure over the simulation [Pa], p_{rms} is the root mean square of the pressure fluctuations [Pa], ρ is the air density (1.187 [kg/m^3]), U_{ref} is the reference velocity

[m/s], which for the validation case is equal to the inlet velocity. A comparison between the LES pressure coefficients and the experiments is shown in Figure 5.9.
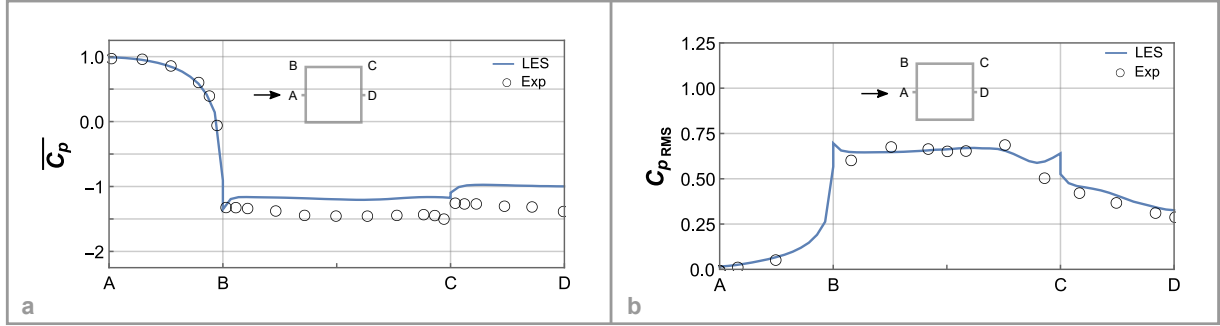
Figure 5.9 – Comparison of the simulated pressure coefficients of a square cylinder with previous experiments: (a) steady component; (b) unsteady component.

The accuracy of the simulations was evaluated using five validation metrics, previously used by [5,49,156]. Deviation from the experimental values by a factor of two (FAC2):

$$FAC2 = \frac{N}{n} = \frac{1}{n}\sum_{i=1}^{n} N_i \quad with \quad N_i = \begin{cases} 1 & for \quad 0.5 \leq \dfrac{P_i}{O_i} \leq 2 \\ 0 & else \end{cases} \tag{5.10}$$

Deviation from the experimental values by a factor of 1.3 (FAC1.3):

$$FAC1.3 = \frac{N}{n} = \frac{1}{n}\sum_{i=1}^{n} N_i \quad with \quad N_i = \begin{cases} 1 & for \quad 0.77 \leq \dfrac{P_i}{O_i} \leq 1.3 \\ 0 & else \end{cases} \tag{5.11}$$

Fractional bias (FB):

$$FB = \frac{\langle O \rangle - \langle P \rangle}{0.5(\langle O \rangle + \langle P \rangle)} \tag{5.12}$$

Normalized mean square error (NMSE):

$$NMSE = \frac{\langle (O - P)^2 \rangle}{\langle O \rangle \langle P \rangle} \tag{5.13}$$

Mean percentage error (MPE):

$$MPE = \frac{100\%}{n} \sum_{i=1}^{n} \frac{|P_i - O_i|}{O_{max} - O_{min}} \tag{5.14}$$

where P_i are the predicted pressure coefficients (from the LES simulations), O_i is the measured pressure coefficient, O_{max} is the maximum measured pressure coefficient, O_{min} is the minimum measured pressure coefficient and n is the total number of measuring points in the experiments. In these expressions, angular brackets denote an average over all data points.

Table 5.2 shows the results of the validation metrics for both the steady ($\overline{C_p}$) and unsteady ($C_{p_{rms}}$) components of the pressure coefficients in the points shown in Figure 5.9. FB and NMSE were not reported for the steady component of the pressure coefficients ($\overline{C_p}$) because these metrics are not appropriate for datasets with positive and negative values [156]. The metrics confirm the qualitative picture shown in Figure 5.9: the predicted pressure coefficients are in good agreement with the experimental values.

Table 5.2 – Results of the validation metrics for the $\overline{C_p}$ and $C_{p_{rms}}$.

	FAC2 [-]	FAC1.3 [-]	FB [-]	NMSE [-]	MPE [%]
$\overline{C_p}$	0.96	0.83	-	-	7.6
$C_{p_{rms}}$	1	0.92	-0.03	0.00	3.9
Ideal values	1	1	0	0	0

5.5. Experimental results

5.5.1. Occurrence of pumping flow

CR2 pumping ventilation was clearly observed in the WT tests. Figure 5.10 shows a room on the leeward side that is ventilated in CR2 pumping, with incoming wind aligned with the building corner (opposite to the room):

- Figure 5.10(a) air flows into the right window and flows out of the left window and into the vortex that will be released.
- Figure 5.10(b) shows the transition period between the formation of the left and right vortices.
- Figure 5.10(c) shows the right vortex in formation, with a high-pressure zone close to the left window (inflow) and a low-pressure zone at the right window (outflow).

Observations also show that the vortex is fed with room air during the low-pressure phase and is cut and released from the back of the bluff body during the high-pressure phase. CR2 pumping with the windows facing the leeward side of the building will be hereafter referred to as back CR2 pumping. As in previous SS2 studies [16,26], we have also been able to observe pumping for CR2 rooms with windward facing windows (front CR2 pumping). Figure 5.10 also shows that the model used had a total of three openable windows; tests with the three windows opened also showed the occurrence of pumping but will not be analyzed in this chapter.
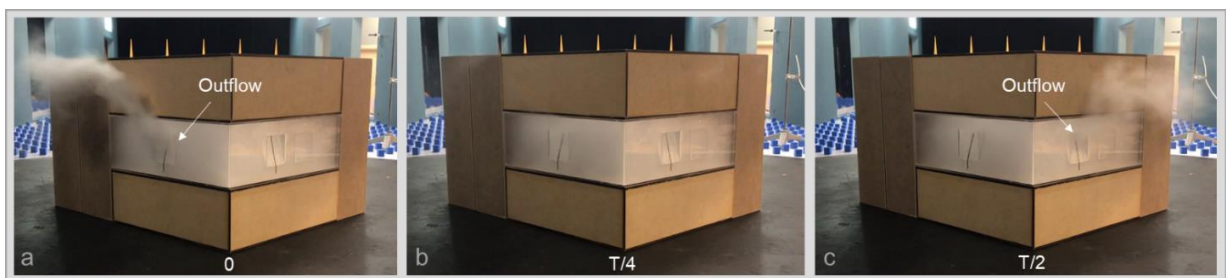
Figure 5.10 – Leeward view of back CR2 pumping ventilation using a smoke visualization technique: (a) formation of a left vortex – air flows from the right to the left window; (b) no vortices – transition period between the left and right vortices; (c) formation of the right vortex – air flows from the left to the right window.

5.5.2. Incoming wind angle limits of pumping

The procedure described in Chapter 5.3.3 was used to identify the incoming wind angle limits for occurrence of CR2 and SS2 pumping ventilation. The analysis showed that the limits are similar for front and back pumping:

- For CR2, the last wind angle for which pumping still occurred was $\theta_{CR2} = \pm\,9^{\circ}\,(\pm\,0.5^{\circ})$.
- For SS2, the last wind angle for which pumping still occurred was $\theta_{SS2} = \pm\,19^{\circ}\,(\pm\,0.5^{\circ})$.

Figure 5.11(a) and (b) show the angle range for the occurrence of pumping ventilation in CR2 and SS2 rooms in isolated buildings. The implication of these results for an isolated building with CR2 and SS2 rooms in all facades, shown in Figure 5.11(c), are quite striking. For this type of building, pumping ventilation occurs in, at least, two rooms in nearly 2/3 (62%) of the incoming wind directions. Therefore, we can conclude that for isolated buildings with SS and CR rooms with two or more openings the recently discovered (2016) [6,16,26] pumping ventilation is a relevant wind driven NV.
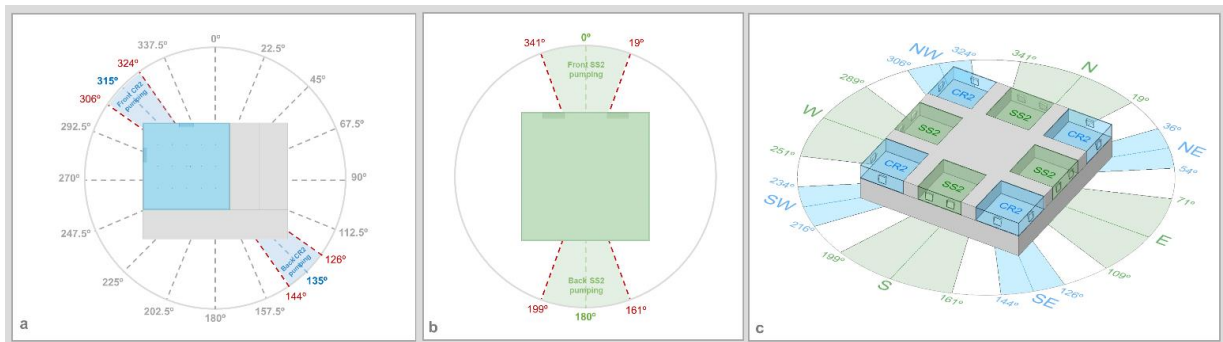
Figure 5.11 – Limits of the pumping ventilation mechanism for the: (a) CR2 building; (b) SS2 building; (c) suggested building model with distributed CR2 and SS2 rooms.

5.5.3. Measured effective ventilation rate

The time variation of the CO_2 concentration profile was similar across all measurements and displayed the typical shape of pollutant concentration decay in a ventilated space, shown in Figure 5.12. The dark gray line represents the mean measured indoor CO_2 concentration and the light gray bands the uncertainty of the measurements, defined as the standard deviation divided by the square root of the number of measurements [95]. Analysis of the logarithm of the CO_2 concentration profile reveals an initial period of pollutant mixing, resulting in an increase in CO_2 concentration inside the room (not shown in Figure 5.12). After this initial period, the constant CO_2 injection rate results in a well-mixed pollutant with a steady average CO_2 concentration (green zone in Figure 5.12). Once CO_2 injection stops, the average concentration decays as a result of non-polluted air inflow through the ventilation openings. During the decay, there is an intermediate period where the logarithm of the CO_2 concentration

114

is approximately linear (blue zone in Figure 5.12). Using data from this linear period, the effective ventilate rate is calculated using the least-square method [5,26,52].
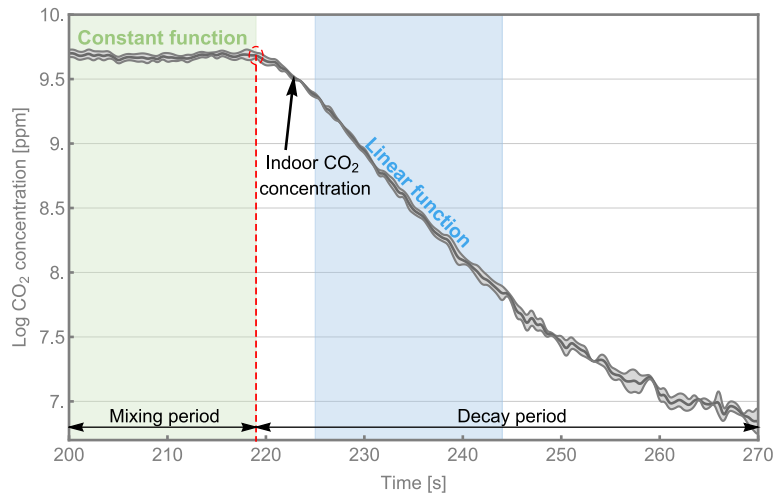
Figure 5.12 – Logarithm of the mean indoor CO_2 concentration during the mixing and decay periods (dark gray line) and its uncertainty (light gray bands) for the wind tunnel measurements.

The effective ventilation rates presented below are normalized using the following expression (Q_{eff}'):

$$Q_{eff}' = \frac{Q_{eff}}{U_{ref} \cdot A_{eff}} \tag{5.15}$$

where Q_{eff} is the measured ventilation rate [m^3/s] and U_{ref} is the reference velocity (in this case, the air velocity at building height) [m/s]. A_{eff} is the effective opening area [m^2], defined by:

$$A_{eff} = \frac{(A_1 \cdot A_2)}{\left(A_1^2 + A_2^2\right)^{1/2}} \tag{5.16}$$

where A_1 and A_2 are the areas of the two bottom-hung inward opening windows [m^2]. These areas are calculated by adding the two triangular areas on the window sides and the rectangular area at the top. For the models used the A_{eff} is 20 cm^2. Figure 5.13 shows the mean normalized effective ventilation rate (black dashed line) and the uncertainty of the measurements (light

gray bands) for the sixteen wind directions tested for the CR2 building. The combination of these results with the flow visualization (discussed in Chapters 5.5.1 and 5.5.2) reveals several regions and points of interest in the data:

- The front and back CR2 pumping angles, 135º and 315º, have a similar flowrate.
- The wake region, 90º to 180º, has the lowest average flowrate, with several points that are lower than the two pumping points.
- The remaining regions display higher flowrates, characteristic of the CV flows that can occur in CR2 rooms.
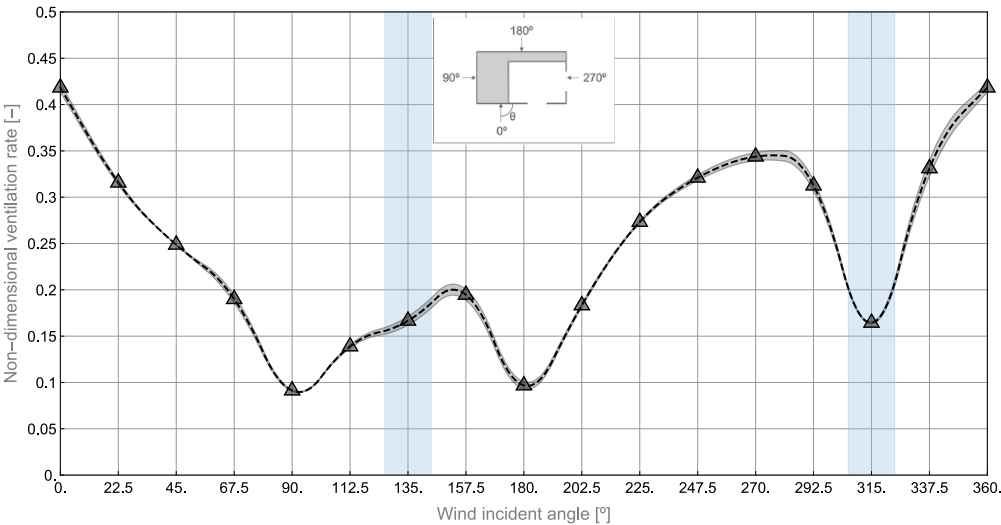
Figure 5.13 – Variation of the mean non-dimensional ventilation rate (black dashed line) and its uncertainty (light gray bands) with several wind incident angles for the CR2 room.

Table 5.3 compares the normalized effective ventilation flowrates measured in SS2 and CR2 pumping flows. For the same window geometry, room size and building height, CR2 pumping has roughly twice the ventilation rate of SS2 pumping. In addition, the effective ventilation rate of front SS2 pumping (wind angle of 0º) is 25% higher than the back SS2 pumping (180º).

Table 5.3 – Comparison of normalized effective ventilation rates of CR2 and SS2 pumping.

	SS2		CR2	
	Front pumping	Back pumping	Front pumping	Back pumping
Wind incident angle [º]	0	180	315	135
Normalized effective ventilation rate [-]	0.0725	0.0581	0.119	0.118

5.6. LES results

The steady and unsteady pressure coefficients predicted by the LES simulations can be used to investigate the role of these pressure components in driving the flows of different incoming wind angles. It can be expected that incoming wind angles that generate pumping ventilation will have a negligible steady pressure difference and relevant unsteady pressure differences between the two openings.

In this analysis, we divided the pressure coefficient difference into its steady (mean) and unsteady (amplitude of the fluctuations) components according to these definitions:

$$\left|\overline{\Delta C_p}\right| = \frac{\left|\overline{\Delta p}\right|}{\frac{1}{2} \rho \, U_{ref}^2} \tag{5.17}$$

$$\Delta C_{p_{amp}} = \sqrt{2} \times \Delta C_{p_{rms}} \tag{5.18}$$

where $\overline{\Delta p}$ is the mean pressure difference across the two apertures [Pa], $\left|\overline{\Delta C_p}\right|$ is the steady pressure coefficient difference [-], and $\Delta C_{p_{amp}}$ is the unsteady pressure coefficient difference [-]. Figure 5.14 shows the value of these two pressure coefficient components for the CR2 ventilation model. This figure also compares the simulated pressure coefficients with the measured CR2 non-dimensional ventilation rate (discussed in Chapter 5.5.3) for 16 wind angles. As expected, for both the back and front CR2 pumping angles (135º and 315º, respectively), the steady component reaches its lowest values, and the unsteady component is slightly higher than the steady component. In the 90º-180º region, results also show that both pressure components have a similar reduced magnitude, which drives the lowest CR2 ventilation rates. For the remaining wind directions, the steady component is significantly higher than the unsteady, leading to higher CR2 cross-ventilation flows. For these wind angles, the similarity in the plotted shapes of the steady component and the mean CR2 ventilation rates is a clear indication that steady pressure is the dominant driving mechanism of CR2 ventilation.
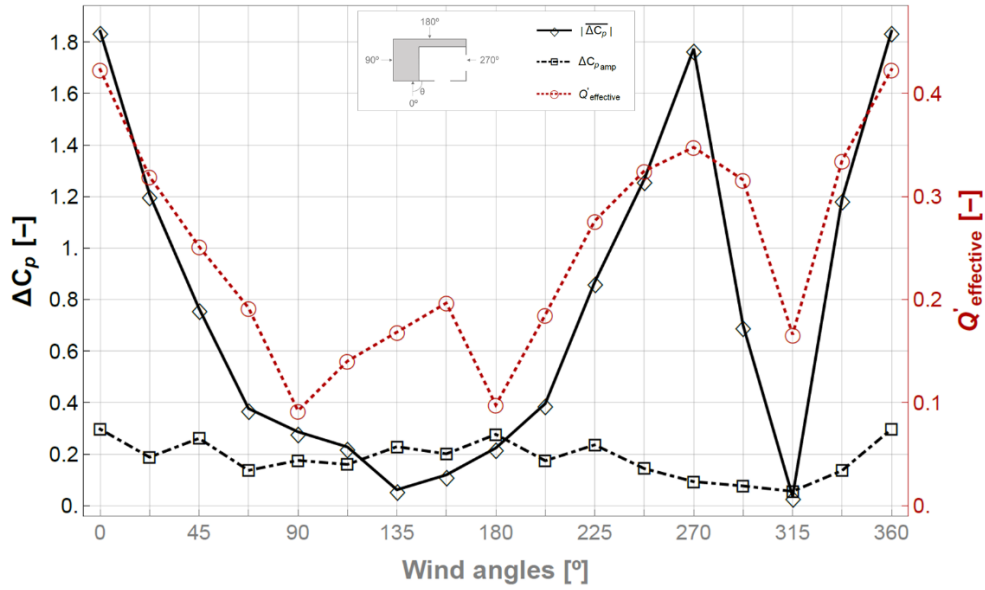
Figure 5.14 – Comparison of the steady and unsteady components of the pressure coefficients and their relation with the CR2 normalized ventilation rate.

Table 5.4 compares the steady and unsteady pressure components of CR2 and SS2 pumping ventilation. As expected, when pumping ventilation occurs the steady component becomes almost negligible, the unsteady component is higher than the steady component, and the unsteady pressure coefficient is the driving mechanism.

Table 5.4 – Relative magnitude of the steady and unsteady pressure components of CR2 and SS2 pumping.

	SS2		CR2	
	Front pumping	Back pumping	Front pumping	Back pumping
$\left|\overline{\Delta C_p}\right|$	~ 0	~ 0	0.04	0.06
$\Delta C_{p_{amp}}$	0.04	0.15	0.06	0.23
$\Delta C_{p_{amp}}\big/\left|\overline{\Delta C_p}\right|$			> 1	

5.7. Application of the aperture equation to predict effective CR2 flow

The previous chapter showed that pumping ventilation is driven by the unsteady component of wind generated pressure. For the incoming wind directions where pumping does not occur, the flow is driven by static pressure difference. With this insight, it is straightforward to develop an aperture equation-based model that can predict effective CR2 ventilation rates from steady and unsteady pressure coefficient data. One difficulty of implementing this model relates to the different flow patterns that occur in CV and pumping. CV flows tend to have a partial short circuit between inflow and outflow openings. This jet region is surrounded by recirculation regions that occupy most of the room volume [157]. In contrast, the periodic motion of pumping flows travels between the openings and creates an alternating cross sided sweep of the room [16,26]. This chapter presents an application of the aperture equation to predict effective CR2 flow. This model will be developed using the effective flows measured in the WT experiments (Chapter 5.5.3) and the simulated pressure coefficients from LES simulations (Chapter 5.6). The proposed simplified model uses the well-known aperture equation [158]:

$$Q_{bulk} = A_{eff} \times C_d \times \sqrt{\frac{2\Delta p}{\rho}} \tag{5.19}$$

where Δp is the static pressure difference between apertures [Pa], and C_d is the discharge coefficient [-], which was considered to be 0.6 [158]. To normalize Eq.(5.19) and introduce pressure coefficients, we use Eq.(5.15) and $\Delta C_p = \frac{\Delta p}{1/2\rho U_{ref}^2}$, obtaining:

$$Q_{bulk}' = \frac{Q_{bulk}}{U_{ref} \times A_{eff}} = C_d \times \sqrt{\Delta C_p} \tag{5.20}$$

where ΔC_p is the pressure coefficient difference between the two ventilation apertures [-]. The aperture equation predicts wind-driven bulk flow. To predict effective flow, we introduce a ventilation efficiency (ε_v), obtaining the following expression:

$$Q_{eff}{}' = \varepsilon_v \times C_d \times \sqrt{\Delta C_p} \qquad (5.21)$$

Finally, we divided Eq.(5.21) to propose two versions of this expression to reflect the pressure component (steady or unsteady) that drives the CR2 pumping and non-pumping flows:

$$Q_{eff}{}' = \varepsilon_{v_{cv}} \times C_d \times \sqrt{\left|\overline{\Delta C_p}\right|} \qquad (5.22)$$

$$Q_{eff}{}' = \varepsilon_{v_p} \times C_d \times \sqrt{\Delta C_{p_{amp}}} \qquad (5.23)$$

where $\varepsilon_{v_{cv}}$ is the efficiency for CR2 CV flows and ε_{v_p} is the efficiency for CR2 pumping flows. As the analysis of the LES results suggested, Eq.(5.23) was used to determine the pumping efficiency of the CR2 pumping flows (see Table 5.5), while Eq.(5.22) determined the CV efficiency of the CR2 non-pumping flows (see Table 5.6). For each pumping flow geometry (front or back), the efficiency of the unsteady pressure of front CR2 pumping flows is twice the efficiency of back CR2 pumping flows. The averaged CR2 pumping efficiency is 75% higher than the averaged CR2 non-pumping efficiency. The results presented in Table 5.5 show a significant problem in the front pumping CR2 efficiency, which is larger than one. A possible explanation for this number may be an underestimation of the $\Delta C_{p_{amp}}$ predicted by the LES or a discharge coefficient that may differ (from the considered constant value of 0.6) for highly unsteady flows.

Table 5.5 – Unsteady pressure efficiencies of CR2 pumping flows.

	CR2	
	Front pumping	Back pumping
ε_{v_p}	1.18	0.59
$\overline{\varepsilon_{v_p}}$	0.89	

Table 5.6 – Steady pressure efficiencies of CR2 non-pumping flows and its mean.

	Wind angle													
	0º	22.5º	45º	67.5º	90º	112.5º	157.5º	180º	202.5º	225º	247.5º	270º	292.5º	337.5º
$\varepsilon_{v_{cv}}$	0.52	0.48	0.48	0.52	0.29	0.49	0.95	0.35	0.49	0.49	0.48	0.44	0.63	0.51
$\overline{\varepsilon_{v_{cv}}}$	0.51													

Using the average of the pressure efficiencies predicted in the previous tables, we propose a CR2 simplified model that depends on the wind incident angle (which affects the driving ventilation mechanism) and may be expressed as:

$$Q_{eff}{'}_{CR2} = \begin{cases} \overline{\varepsilon_{v_p}} \times C_d \times \sqrt{\Delta C_{p_{amp}}} & if \quad \theta=135º,315º \\ \\ \overline{\varepsilon_{v_{cv}}} \times C_d \times \sqrt{\left|\overline{\Delta C_p}\right|} & all\ other\ angles \end{cases} \tag{5.24}$$

Figure 5.15 shows a comparison between the measured airflow and the simplified model predictions. In the regions shown in blue (back and front CR2 pumping) the unsteady pressures are used. To estimate the error of the proposed model, five error indicators (Eqs.(5.10)–(5.14)) were used. Table 5.7 shows very encouraging results as the proposed model had a mean percentage error of 10.2%.
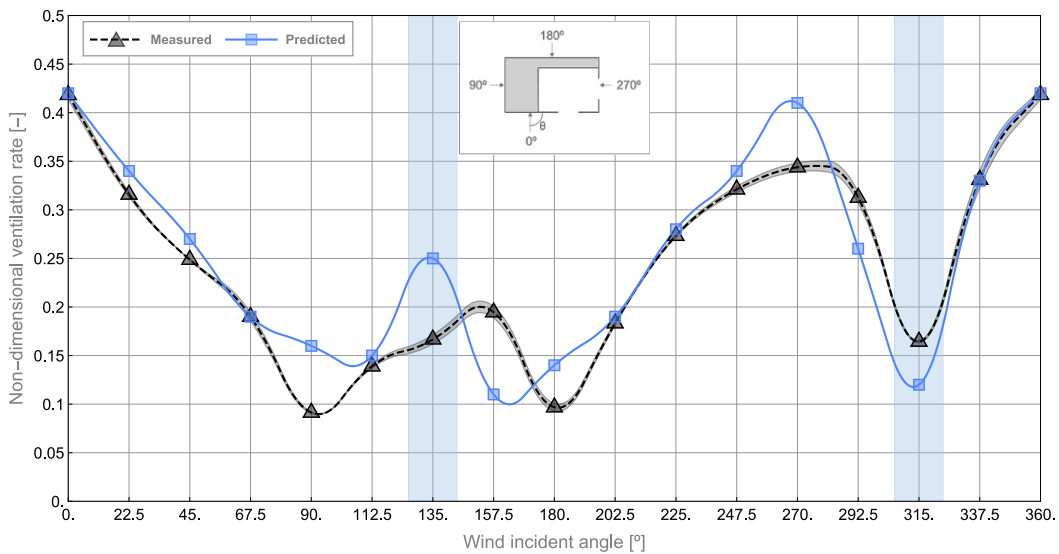

Figure 5.15 – Non-dimensional CR2 ventilation rate: Predicted versus measured.

Table 5.7 – Error estimation of the proposed CR2 simplified model.

	FAC2 [-]	FAC1.3 [-]	FB [-]	NMSE [-]	MPE [%]
$Q_{eff}^{'}$	1	0.69	-0.03	0.03	10.2
Ideal values	1	1	0	0	0

5.8. Conclusions

This chapter presents an experimental and numerical study of single sided and corner ventilation of rooms in a rectangular building exposed to wind. Tracer gas measurements of effective airflow were performed in an atmospheric boundary layer wind tunnel using two rectangular three-story building models (1/20 scale) with a naturally ventilated middle floor. Smoke visualization was used to investigate the transition between unsteady pumping ventilation to the steady cross-ventilation. Three-dimensional computational fluid dynamics large eddy simulations were performed to obtain wind generated pressures in the ventilation openings and to investigate the role of the pressure components (steady and unsteady) in the ventilation mechanism of rooms with single sided and corner window configurations.

Experimental results confirmed the existence of corner pumping ventilation (CR2) at the front and back of the model and showed that pumping ventilation occurs in a range of incoming wind angles: ±19° for single sided; and ±9° for corner rooms. As a result, an isolated rectangular building with single sided and corner rooms can have pumping ventilation in 62% of incoming wind directions. CR2 effective flow measurements were performed for sixteen wind angles revealing that back and front CR2 pumping have similar effective flowrates. Overall, the wake region showed the lowest flowrates, with the remaining regions displaying higher flowrates that are typical of CV flows. The measured SS2 pumping flowrates are approximately half of the CR2 pumping flowrates.

LES simulation results show that the transition from pumping to cross-ventilation occurs when the steady pressure becomes higher than the unsteady component. Clearly, pumping is driven by unsteady pressure while CV (for CR2) and cross-sided (for SS2) ventilation are driven by steady pressure. Results from the effective flow measurements and the simulated pressure coefficients were used to develop a simple model that highlights the role of steady and unsteady pressure and predicts pumping and CV in CR2 ventilation with engineering precision. The developed pressure based simplified model for corner ventilation can predict effective airflow from external wind generated pressures with an average error below 10.2%.

6. GENERAL CONCLUSIONS

Natural ventilation (NV) may have a positive impact on buildings and their occupants, in terms of its capacity to provide fresh air, improve indoor air quality (by removing odors and other pollutants), and keep occupants thermally comfortable, eventually requiring almost no energy. Understanding this trend, designers have become increasingly interested in the use of natural ventilation systems in buildings. However, different NV configurations can be very challenging to predict and/or model. The work developed in this thesis focused on the understanding and modelling of four NV systems: night cooling ventilation (NVC), single sided ventilation with one opening (SS1), pumping ventilation (SS2 and CR2) and corner ventilation (CR2).

Chapter 2 presented the first full-scale measurement of cooling load reduction due to night cooling (NVC) in a large service building. The measurements were performed in a large atrium of an office building in a warm climate. The results confirmed that NVC could provide a measurable reduction in cooling energy demand of service buildings with exposed internal mass. Comparison of the measured daytime cooling load of days with similar weather and variable use of the NVC system in the previous night (on or off) showed that the NVC system reduced the CF cooling load by 27%. The combination of two simulation tools (EnergyPlus and CFD) used in this study could predict the cooling load reduction, internal air temperatures and bulk NVC airflow rates with average errors of 1.7%, 11.2% and 14.1%, respectively. This study allowed for a better understanding of the expected cooling energy demand reduction that NVC systems can achieve. In addition, the results indicated that the precision of existing simulation tools was adequate to assess expected energy savings and feasibility of NVC systems during the building design phase.

Chapter 3 presented the first experimental study of the impact of typical window geometries on SS1 NV flows driven by wind shear parallel to the building façade. Flow visualizations near the plain opening confirmed that wind driven SS1 flows in large facades are the result of a turbulent shear layer that develops in the opening plane. Results for seven commonly used window configurations showed that the combination between window geometry and wind direction has a large impact on SS1 ventilation (may vary by a factor of 5). The results of the experiments were incorporated into the most successful existing simplified SS1 model (Warren & Parkins), allowing for greatly increased precision when predicting wind driven SS1 flows. This chapter also identified the best window configurations for wind driven SS1 in dense urban environments. By combining average results for measured wind velocities in street canyons

with the measured window airflow performance, it was possible to propose simple correlations for wind driven SS1 in urban environments that are more precise than existing models.

Chapter 4 presented a detailed experimental dataset of pumping ventilation flow. The average vortex shedding frequency was measured using three independent methods (smoke visualization, HWA and PIV). The measured average oscillation frequency implies a *Strouhal* number of 0.10, a value in-line with existing experimental and numerical studies. The experimental results confirmed that pumping ventilation flowrate increases with window separation. Further, this study revealed an approximately linear relation between effective flowrate and window separation. This chapter also evaluated the capability of commonly used numerical simulation approaches (LES and URANS) to predict pumping ventilation. LES showed to be a suitable simulation approach for pumping ventilation with a mean absolute error of 5%, while URANS results underestimated the ventilation rates by more than 40%, showing its inadequacy to proper study pumping ventilation.

Chapter 5 presented an experimental and numerical study of single sided and corner ventilation of rooms in a rectangular building exposed to wind. Smoke visualization allowed to confirm the existence of CR2 pumping ventilation (at the front and back of the model) when the wind was aligned with the building corner, and the transition between unsteady pumping ventilation to the steady cross-ventilation (CR2) or cross-sided (SS2). Experimental results showed that pumping ventilation occurs in a range of incoming wind angles: ± 19º for single sided; and ± 9º for corner rooms. As a result, an isolated rectangular building with single sided and corner rooms can have pumping ventilation in 62% of incoming wind directions. LES simulations were performed to investigate the role of the pressure components (steady and unsteady) in the ventilation mechanism of rooms with single sided and corner window configurations. LES simulation results show that the transition from pumping to cross-ventilation occurs when the steady pressure becomes higher than the unsteady component. Clearly, pumping is driven by unsteady pressure while CV (for CR2) and cross-sided (for SS2) ventilation are driven by steady pressure. Results from the effective flow measurements and the simulated pressure coefficients were used to develop a simple model that highlights the role of steady and unsteady pressure and predicts pumping and cross-ventilation in CR2 ventilated rooms with engineering precision.

The developments presented in this thesis open many questions that merit future research. The most relevant of these is the effect of buoyancy in the flows studied in chapters 3–5. Buoyancy forces are present wherever human activity occurs, and wind is generally limited in the dense

urban environments that are becoming more prevalent. In this scenario, one can expect very interesting interactions between wind and buoyancy that will present a significant challenge for future research.

7. REFERENCES

[1] Ürge-Vorsatz D, Cabeza LF, Serrano S, Barreneche C, Petrichenko K. Heating and cooling energy trends and drivers in buildings. Renew Sustain Energy Rev 2015;41:85–98. https://doi.org/10.1016/j.rser.2014.08.039.

[2] Luke Troup, Robert Phillips, Matthew J. Eckelman, David Fannon, Effect of window-to-wall ratio on measured energy consumption in US office buildings, Energy and Buildings, Volume 203, 2019, 109434, ISSN 0378-7788, https://doi.org/10.1016/j.enbuild.2019.109434

[3] da Graça, Guilherme Carrilho, Daniel P. Albuquerque, and Maria M. Lerer. "Ventilative cooling design for a large office building."

[4] O' Donovan A, O' Sullivan PD, Murphy MD. Predicting air temperatures in a naturally ventilated nearly zero energy building: Calibration, validation, analysis and approaches. Appl Energy 2019;250:991–1010. https://doi.org/10.1016/j.apenergy.2019.04.082.

[5] Daniel P. Albuquerque, Nuno Mateus, Marta Avantaggiato, Guilherme Carrilho da Graça, Full-scale measurement and validated simulation of cooling load reduction due to nighttime natural ventilation of a large atrium, Energy and Buildings, Volume 224, 2020, 110233, ISSN 0378-7788, https://doi.org/10.1016/j.enbuild.2020.110233.

[6] Carrilho da Graça G, Linden P.F., Ten questions about natural ventilation of non-domestic buildings. Build Environ 2016; 107:263–73. https://doi.org/10.1016/j.buildenv.2016.08.007.

[7] Allocca C, Chen Q, Glicksman LR. Design analysis of single-sided natural ventilation. Energy Build 2003; 35:785–95. https://doi.org/10.1016/S0378-7788(02)00239-6.

[8] Givoni B. Performance and applicability of passive and low-energy cooling systems. Energy Build 1991;17:177–99. https://doi.org/10.1016/0378-7788(91)90106-D.

[9] Dnyandip K. Bhamare, Manish K. Rathod, Jyotirmay Banerjee, Passive cooling techniques for building and their applicability in different climatic zones—The state of

art, Energy and Buildings, Volume 198, 2019, Pages 467-490, ISSN 0378-7788, https://doi.org/10.1016/j.enbuild.2019.06.023.

[10] G Carrilho da Graça, Q Chen, L.R Glicksman, L.K Norford, Simulation of wind-driven ventilative cooling systems for an apartment building in Beijing and Shanghai, Energy and Buildings, Volume 34, Issue 1, 2002, Pages 1-11, ISSN 0378-7788, https://doi.org/10.1016/S0378-7788(01)00083-4.

[11] Artmann N, Manz H, Heiselberg P. Climatic potential for passive cooling of buildings by night-time ventilation in Europe. Appl Energy 2007;84:187–201. https://doi.org/10.1016/j.apenergy.2006.05.004.

[12] P.F. Linden, K. Adams, E. Arens, D. Banks, S. Brunswick, G. Carrilho da Graca, N. Daish, S. Dutton, M. Fountain, B. Fisk, R. Gerard, F. Gillan, G. Gross, P. Haves, M. Hill, A. Honnekeri, M. Hovanec, T. Lawton, M. Pigman, P. Switenki, G. Szakats, R. Thomas, Y. Zhai, H. Zhang, Natural ventilation for energy savings in California commercial buildings, Final Proj. Report, Calif. Energy Comm. June. 516 Pp. (2016). http://www.escholarship.org/uc/item/4cd386s7.

[13] T.S. Larsen, P. Heiselberg, Single-sided natural ventilation driven by wind pressure and temperature difference, Energy and Buildings. 40 (2008) 1031–1040. https://doi.org/10.1016/j.enbuild.2006.07.012.

[14] G. Carrilho da Graça, A technical note on simplified modeling of turbulent mixing in wind-driven single sided ventilation. Building and Environment. 131, 12–15 (2018). https://doi.org/10.1016/j.buildenv.2018.01.014

[15] F. Haghighat, J. Rao, P. Fazio, The influence of turbulent wind on air change rates—a modelling approach, Building and Environment. 26 (1991) 95–109. https://doi.org/https://doi.org/10.1016/0360-1323(91)90017-6.

[16] N.C. Daish, G. Carrilho da Graça, P.F. Linden, D. Banks, Impact of aperture separation on wind-driven single-sided natural ventilation, Building and Environment, Volume 108, 2016, Pages 122-134, ISSN 0360-1323, https://doi.org/10.1016/j.buildenv.2016.08.015

[17]   Daniel Albuquerque, Guilherme Carrilho da Graça, Use of building thermal and CFD simulation in the design of a large office building in Lisbon, Proceedings of BS2015: 14th Conference of International Building Performance Simulation Association, Hyderabad, India, Dec. 7-9, 2015.

[18]   Carrilho da Graça G, Linden P F, Haves P. Design and testing of a control strategy for a large, naturally ventilated office building. Building Services Engineering Research and Technology. 2004; 25(3): 223-239. https://doi.org/10.1191/0143624404bt107oa.

[19]   P.R. Warren, Ventilation through openings on one wall only. Heat Transfer in Buildings, Proceedings of ICHMT Seminar (1977), Hemisphere. New York, EE. UU

[20]   P.R. Warren, L.M. Parkins, Single-sided ventilation through open windows, Conference Proceedings, Thermal Performance of the Exterior Envelopes of Buildings, Florida, ASHRAE SP 49 (1985), pp. 209-228

[21]   T. Yamanaka, H. Kotani, K. Iwamoto, M. Kato, Natural, wind-forced ventilation caused by turbulence in a room with a single opening, International Journal of Ventilation. 5 (2006) 179–187. https://doi.org/10.1080/14733315.2006.11683735.

[22]   Dimotakis, Paul E., Two-dimensional shear-layer entrainment. AIAA journal 24.11 (1986): 1791-1796.

[23]   D.W. Etheridge, M. Sandberg, Building ventilation: theory and measurement, John Wiley & Sons Chichester, 1996.

[24]   F.H. Abernathy, R.E. Kronauer, The formation of vortex streets, J. Fluid Mech. 13 (1962) 1–20. doi:10.1017/S0022112062000452.

[25]   A. Roshko, On the development of turbulent wakes from vortex streets, (1954).

[26]   Daniel P. Albuquerque, Mats Sandberg, P.F. Linden, Guilherme Carrilho da Graça, Experimental and numerical investigation of pumping ventilation on the leeward side of a cubic building, Building and Environment, Volume 179, 2020, 106897, ISSN 0360-1323, https://doi.org/10.1016/j.buildenv.2020.106897

[27]   Ebrahim Solgi, Zahra Hamedani, Ruwan Fernando, Henry Skates, Nnamdi Ezekiel Orji, A literature review of night ventilation strategies in buildings, Energy and

Buildings, Volume 173, 2018, Pages 337-352, ISSN 0378-7788, https://doi.org/10.1016/j.enbuild.2018.05.052.

[28]   Blondeau P, Spérandio M, Allard F. Night ventilation for building cooling in summer. Sol Energy 1997;61:327–35. https://doi.org/10.1016/S0038-092X(97)00076-5.

[29]   Jared Landsman, Gail Brager, Mona Doctor-Pingel, Performance, prediction, optimization, and user behavior of night ventilation, Energy and Buildings, Volume 166, 2018, Pages 60-72, ISSN 0378-7788, https://doi.org/10.1016/j.enbuild.2018.01.026.

[30]   Yuan S, Vallianos C, Athienitis A, Rao J. A study of hybrid ventilation in an institutional building for predictive control. Build Environ 2018;128:1–11. https://doi.org/10.1016/j.buildenv.2017.11.008.

[31]   Breesch H, Merema B, Versele A. Ventilative Cooling in a School Building: Evaluation of the Measured Performances. *Fluids*. 2018; 3(4):68.

[32]   Gwynne Á. Mhuireach, G.Z. Brown, Jeff Kline, Dristi Manandhar, Maxwell Moriyama, Dale Northcutt, Isabel Rivera, Kevin Van Den Wymelenberg, Lessons learned from implementing night ventilation of mass in a next-generation smart building, Energy and Buildings, Volume 207, 2020, 109547, ISSN 0378-7788, https://doi.org/10.1016/j.enbuild.2019.109547.

[33]   Santamouris M, Sfakianaki A, Pavlou K. On the efficiency of night ventilation techniques applied to residential buildings. Energy and Buildings. 2010 Aug 1;42(8):1309-13.

[34]   Guo R, Gao Y, Zhuang C, Heiselberg P, Levinson R, Zhao X, Shi D. Optimization of cool roof and night ventilation in office buildings: a case study in Xiamen, China. Renewable Energy. 2019 Oct 9.

[35]   Mylona Z, Kolokotroni M, Tassou SA. Coupling night ventilative and active cooling to reduce energy use in supermarkets with high refrigeration loads. Energy and Buildings. 2018 Jul 15;171:26-39.

[36]   Vujošević M, Krstić-Furundžić A. The influence of atrium on energy performance of hotel building. Energy Build 2017;156:140–50. https://doi.org/10.1016/j.enbuild.2017.09.068.

[37]   Karava P, Athienitis AK, Stathopoulos T, Mouriki E. Experimental study of the thermal performance of a large institutional building with mixed-mode cooling and hybrid ventilation. Build Environ 2012;57:313–26. https://doi.org/10.1016/j.buildenv.2012.06.003.

[38]   Ray SD, Gong NW, Glicksman LR, Paradiso JA. Experimental characterization of full-scale naturally ventilated atrium and validation of CFD simulations. Energy Build 2014;69:285–91. https://doi.org/10.1016/j.enbuild.2013.11.018.

[39]   Moosavi L, Mahyuddin N, Ab Ghafar N, Azzam Ismail M. Thermal performance of atria: An overview of natural ventilation effective designs. Renew Sustain Energy Rev 2014;34:654–70. https://doi.org/10.1016/j.rser.2014.02.035.

[40]   Salcido JC, Raheem AA, Issa RRA. From simulation to monitoring: Evaluating the potential of mixed-mode ventilation (MMV) systems for integrating natural ventilation in office buildings through a comprehensive literature review. Energy Build 2016;127:1008–18. https://doi.org/10.1016/j.enbuild.2016.06.054.

[41]   Daniel Daly, Paul Cooper, Zhenjun Ma, Qualitative analysis of the use of building performance simulation for retrofitting lower quality office buildings in Australia, Energy and Buildings, Volume 181, 2018, Pages 84-94, ISSN 0378-7788, https://doi.org/10.1016/j.enbuild.2018.09.040.

[42]   Ramponi R, Angelotti A, Blocken B. Energy saving potential of night ventilation: Sensitivity to pressure coefficients for different European climates. Appl Energy 2014; 123:185–95.

[43]   Kottek M, Grieser J, Beck C, Rudolf B, Rubel F. World map of the Köppen-Geiger climate classification updated. Meteorol Zeitschrift 2006;15:259–63.

[44]   Martins NR, da Graça GC. Validation of numerical simulation tools for wind-driven natural ventilation design. Build Simul 2016; 9:75–87. https://doi.org/10.1007/s12273-015-0251-6.

[45]   Franke J, Hirsch C, Jensen AG, Krüs HW, Schatzmann M, Westbury PS, et al. Recommendations on the use of CFD in wind engineering. Cost action C, vol. 14, 2004, p. C1.

[46]   Blocken B. Computational Fluid Dynamics for urban physics: Importance, scales, possibilities, limitations and ten tips and tricks towards accurate and reliable simulations. Build Environ 2015;91:219–45. https://doi.org/10.1016/j.buildenv.2015.02.015.

[47]   Richards PJ, Hoxey RP. Appropriate boundary conditions for computational wind engineering models using the k-ϵ turbulence model. J Wind Eng Ind Aerodyn 1993;46–47:145–53. https://doi.org/https://doi.org/10.1016/0167-6105(93)90124-7.

[48]   J. Wieringa, Updating the Davenport roughness classification, J. Wind Eng. Ind. Aerodyn., 44 (1992), pp. 357-368.

[49]   Hooff T Van, Blocken B, Tominaga Y. On the accuracy of CFD simulations of cross-ventilation flows for a generic isolated building: Comparison of RANS, LES and experiments. Build Environ 2017; 114:148–65. https://doi.org/10.1016/j.buildenv.2016.12.019.

[50]   Moser A, Clancy E, Collineau S, Fontaine J-R, Heiselberg P, Howarth A, et al. Techical Synthesis Report - Energy Efficient Ventilation of Large Enclosures. 1998.

[51]   Mateus NM, Simões GN, Lúcio C, da Graça GC. Comparison of measured and simulated performance of natural displacement ventilation systems for classrooms. Energy Build 2016;133:185–96. https://doi.org/10.1016/j.enbuild.2016.09.057.

[52]   S. Cui, M. Cohen, P. Stabat, D. Marchio, CO2 tracer gas concentration decay method for measuring air change rate, Building and Environment. 84 (2015) 162–169. https://doi.org/10.1016/j.buildenv.2014.11.007.

[53]   Avantaggiato, M. Mixed-mode ventilation design and thermal comfort in transitional spaces. 2018. [Ph.D. thesis]

[54]   EN ISO 7726. Ergonomics of the thermal environment. Instruments for measuring physical quantities.1998.

[55]   M.A. Humphreys. The optimum diameter for a globe thermometer for use indoors. Annals of Occupational Hygiene 1977; 20:135–40.

[56]   A. Simone, J. Babiak., M. Bullo, G. Landkilde., B.W: Olesen., "Operative temperature control of radiant surface heating and cooling systems", In proceedings of: Clima 2007 Wellbeing Indoors. Finland, Helsinki, June 10-14, 2007.

[57]   ASHRAE Standard 55. Thermal Environment Condition for Human Occupancy. American society of Heating, Refrigeration and Air-Conditioning Engineers. Atlanta, 2010.

[58]   Drury B. Crawley, Linda K. Lawrie, Frederick C. Winkelmann, W.F. Buhl, Y.Joe Huang, Curtis O. Pedersen, Richard K. Strand, Richard J. Liesen, Daniel E. Fisher, Michael J. Witte, Jason Glazer, EnergyPlus: creating a new-generation building energy simulation program, Energy and Buildings, Volume 33, Issue 4, April 2001, Pages 319-331 , ISSN 0378-7788, http://dx.doi.org/10.1016/S0378-7788(00)00114-6.

[59]   DOE, US. "EnergyPlus Engineering Reference." The Reference to EnergyPlus Calculations (2018).

[60]   Nuno M. Mateus, Armando Pinto, Guilherme Carrilho da Graça, Validation of EnergyPlus thermal simulation of a double skin naturally and mechanically ventilated test cell, Energy and Buildings, Volume 75, June 2014, Pages 511-522, ISSN 0378-7788, http://dx.doi.org/10.1016/j.enbuild.2014.02.043.

[61]   Z. Zhai, M. Johnson, M. Krarti, Assessment of natural and hybrid ventilation models in whole-building energy simulations, Energy and Buildings 43 (9)(2011) 2251–2261, http://dx.doi.org/10.1016/j.enbuild.2011.06.026.

[62]   Nuno M. Mateus, Guilherme Carrilho da Graça, Simulated and measured performance of displacement ventilation systems in large rooms, Building and Environment, Volume   114,   2017,   Pages   470-482,   ISSN   0360-1323, https://doi.org/10.1016/j.buildenv.2017.01.002.

[63]   C. Buratti, E. Moretti, E. Belloni, F. Cotana, Unsteady simulation of energy performance and thermal comfort in non-residential buildings, Building and

Environment, Volume 59, January 2013, Pages 482-491, ISSN 0360-1323, http://dx.doi.org/10.1016/j.buildenv.2012.09.015.

[64] F. Flourentzou, J. Van der Maas, C.-A. Roulet, Natural ventilation for passive cooling: measurement of discharge coefficients, Energy and Buildings, Volume 27, Issue 3, June 1998, Pages 283-292, ISSN 0378-7788, http://dx.doi.org/10.1016/S0378-7788(97)00043-1.

[65] Walton, G. N., Thermal Analysis Research Program Reference Manual. NBSSIR 83-2655. National Bureau of Standards, 1983.

[66] J. Park, X. Sun, J. Il Choi, G.H. Rhee, Effect of wind and buoyancy interaction on single-sided ventilation in a building, Journal of Wind Engineering and Industrial Aerodynamics. 171 (2017) 380–389. https://doi.org/10.1016/j.jweia.2017.10.016.

[67] G. Evola, V. Popov, Computational analysis of wind driven natural ventilation in buildings, Energy and Buildings. 38 (2006) 491–501. https://doi.org/10.1016/j.enbuild.2005.08.008.

[68] A. Hayati, M. Mattsson, M. Sandberg, Single-sided ventilation through external doors: Measurements and model evaluation in five historical churches, Energy and Buildings. 141 (2017) 114–124. https://doi.org/10.1016/j.enbuild.2017.02.034.

[69] H. Wang, P. Karava, Q. Chen, Development of simple semiempirical models for calculating airflow through hopper, awning, and casement windows for single sided natural ventilation, Energy Build. 96 (2015) 373–384, https://doi.org/10.1016/j.enbuild.2015.03.041.

[70] J. Wang, T. Zhang, S. Wang, F. Battaglia, Numerical investigation of single-sided natural ventilation driven by buoyancy and wind through variable window configurations, Energy Build. 168 (2018) 147–164, https://doi.org/10.1016/j.enbuild.2018.03.015.

[71] S. Kato, R. Kono, T. Hasama, R. Ooka, T. Takahashi, A wind tunnel experimental analysis of the ventilation characteristics of a room with single-sided opening in uniform flow, International Journal of Ventilation. 5 (2006) 171–178. https://doi.org/10.1080/14733315.2006.11683734.

[72]   W. De Gids, H. Phaff, Ventilation rates and energy consumption due to open windows: a brief overview of research in the Netherlands, Air Infiltration Rev, 4 (1982)

[73]   Per Heiselberg, Kjeld Svidt, Peter V. Nielsen, Characteristics of airflow from open windows, Building and Environment, Volume 36, Issue 7, 2001, Pages 859-869, ISSN 0360-1323, https://doi.org/10.1016/S0360-1323(01)00012-9.

[74]   J. Von Grabe, Flow resistance for different types of windows in the case of buoyancy ventilation, Energy and Buildings. 65 (2013) 516–522. https://doi.org/10.1016/j.enbuild.2013.06.035.

[75]   J. Von Grabe, P. Svoboda, A. Bäumler, Window ventilation efficiency in the case of buoyancy ventilation, Energy and Buildings. 72 (2014) 203–211. https://doi.org/10.1016/j.enbuild.2013.10.006.

[76]   J. Wang, Q. Huo, T. Zhang, S. Wang, F. Battaglia, Numerical investigation of gaseous pollutant cross-transmission for single-sided natural ventilation driven by buoyancy and wind, Building and Environment. 172 (2020) 106705. https://doi.org/10.1016/j.buildenv.2020.106705.

[77]   M. Caciolo, P. Stabat, D. Marchio, Full scale experimental study of single-sided ventilation: Analysis of stack and wind effects, Energy and Buildings. 43 (2011) 1765–1773. https://doi.org/10.1016/j.enbuild.2011.03.019.

[78]   W.G. Brown, K.R. Solvason, Natural convection through rectangular openings in partitions—1: Vertical partitions, International Journal of Heat and Mass Transfer, Volume 5, Issue 9, 1962, Pages 859-868, ISSN 0017-9310, https://doi.org/10.1016/0017-9310(62)90184-9.

[79]   Shaw, B. H., Heat and mass transfer by natural convection and combined natural and forced air flow through large rectangular openings in vertical partitions. In Proc. Int. Mech. Eng. Conf. on Heat and Mass Transfer by Combined Forced and Natural Convection, Manchester, UK, 1978, pp. 31-39.

[80]   M. Caciolo, S. Cui, P. Stabat, D. Marchio, Development of a new correlation for single-sided natural ventilation adapted to leeward conditions, Energy and Buildings. 60 (2013) 372–382. https://doi.org/10.1016/j.enbuild.2013.01.024.

[81] E. Dascalaki, M. Santamouris, A. Argiriou, C. Helmis, D.N. Asimakopoulos, K. Papadopoulos, A. Soilemes, Predicting single sided natural ventilation rates in buildings, Solar Energy. 55 (1995) 327–341. https://doi.org/10.1016/0038-092X(95)00057-X.

[82] A.A. Argiriou, C.A. Balaras, S.P. Lykoudis, Single-sided ventilation of buildings through shaded large openings, Energy. 27 (2002) 93–115. https://doi.org/10.1016/S0360-5442(01)00058-5.

[83] H. Wang, Q. Chen, A new empirical model for predicting single-sided, wind-driven natural ventilation in buildings, Energy and Buildings. 54 (2012) 386–394. https://doi.org/10.1016/j.enbuild.2012.07.028.

[84] P.D. O'Sullivan, M. Kolokotroni, A field study of wind dominant single sided ventilation through a narrow slotted architectural louvre system, Energy and Buildings. 138 (2017) 733–747. https://doi.org/10.1016/j.enbuild.2016.11.025.

[85] W. Pan, S. Liu, S. Li, X. Cheng, H. Zhang, Z. Long, T. Zhang, Q. Chen, A model for calculating single-sided natural ventilation rate in an urban residential apartment, Building and Environment. 147 (2019) 372–381. https://doi.org/10.1016/j.buildenv.2018.08.047.

[86] H.L. Gough, J.F. Barlow, Z. Luo, M.F. King, C.H. Halios, C.S.B. Grimmond, Evaluating single-sided natural ventilation models against full-scale idealised measurements: Impact of wind direction and turbulence, Building and Environment. 170 (2020) 106556. https://doi.org/10.1016/j.buildenv.2019.106556.

[87] S. Fan, M.S. Davies Wykes, W.E. Lin, R.L. Jones, A.G. Robins, P.F. Linden, A full-scale field study for evaluation of simple analytical models of cross ventilation and single-sided ventilation, Building and Environment. 187 (2021) 107386. https://doi.org/10.1016/j.buildenv.2020.107386.

[88] P. Sharpe, B. Jones, R. Wilson, C. Iddon, What we think we know about the aerodynamic performance of windows, Energy Build. (2020) 110556. https://doi.org/10.1016/j.enbuild.2020.110556.

[89]   A.G. Davenport, The application of statistical concepts to the wind loading of structures., Proc. Inst. Civ. Eng. 19 (1961) 449–472.

[90]   B. Blocken, W.D. Janssen, T. van Hooff, CFD simulation for pedestrian wind comfort and wind safety in urban areas: General decision framework and case study for the Eindhoven University campus, Environmental Modelling & Software, Volume 30, 2012, Pages 15-34, ISSN 1364-8152, https://doi.org/10.1016/j.envsoft.2011.11.009.

[91]   T. van Hooff, B. Blocken, Coupled urban wind flow and indoor natural ventilation modelling on a high-resolution grid: A case study for the Amsterdam ArenA stadium, Environmental Modelling & Software, Volume 25, Issue 1, 2010, Pages 51-65, ISSN 1364-8152, https://doi.org/10.1016/j.envsoft.2009.07.008.

[92]   P. Gousseau, B. Blocken, T. Stathopoulos, G.J.F. van Heijst, CFD simulation of near-field pollutant dispersion on a high-resolution grid: A case study by LES and RANS for a building group in downtown Montreal, Atmospheric Environment, Volume 45, Issue 2, 2011, Pages 428-438, ISSN 1352-2310, https://doi.org/10.1016/j.atmosenv.2010.09.065.

[93]   G. Remion, B. Moujalled, M. El, Review of tracer gas-based methods for the characterization of natural ventilation performance: Comparative analysis of their accuracy, Building and Environment. 160 (2019) 106180. https://doi.org/10.1016/j.buildenv.2019.106180.

[94]   B. Blocken, T. Stathopoulos, J.P.A.J. van Beeck, Pedestrian-level wind conditions around buildings: Review of wind-tunnel and CFD techniques and their accuracy for wind comfort assessment, Building and Environment. 100 (2016) 50–81. https://doi.org/10.1016/j.buildenv.2016.02.004.

[95]   Wolfram Language. (2019). MeanAround. Wolfram Language & System Documentation Center. Accessed 06 January 2021, Retrieved from https://reference.wolfram.com/language/ref/MeanAround.html.

[96]   H. Coanda, C. France, Device for deflecting a stream of elastic fluid projected into an elastic fluid, US Patent Office, 2,052,869, 1936.

[97] H.D. Goodfellow, E. Tahti, Industrial ventilation design guidebook, Academic press, 2002. https://doi.org/10.1016/s1074-9098(01)00282-9.

[98] T. van Hooff, B. Blocken, T. Defraeye, J. Carmeliet, G.J.F. van Heijst, PIV measurements and analysis of transitional flow in a reduced-scale model: Ventilation by a free plane jet with Coanda effect, Building and Environment. 56 (2012) 301–313. https://doi.org/10.1016/j.buildenv.2012.03.020.

[99] A.W.M. Yazid, nor A.C. Sidik, S.M. Salim, K.M. Saqr, A review on the flow structure and pollutant dispersion in urban street canyons for urban planning strategies, Simulation. 90 (2014) 892–916. https://doi.org/10.1177/0037549714528046.

[100] D. Voordeckers, T. Lauriks, S. Denys, P. Billen, T. Tytgat, M. Van Acker, Guidelines for passive control of traffic-related air pollution in street canyons: An overview for urban planning, Landscape and Urban Planning. 207 (2021) 103980. https://doi.org/10.1016/j.landurbplan.2020.103980.

[101] Y.D. Huang, R.W. Hou, Z.Y. Liu, Y. Song, P.Y. Cui, C.N. Kim, Effects of wind direction on the airflow and pollutant dispersion inside a long street canyon, Aerosol and Air Quality Research. 19 (2019) 1152–1171. https://doi.org/10.4209/aaqr.2018.09.0344.

[102] J.J. Baik, R.S. Park, H.Y. Chun, J.J. Kim, A laboratory model of urban street-canyon flows, Journal of Applied Meteorology. 39 (2000) 1592–1600. https://doi.org/10.1175/1520-0450(2000)039<1592:ALMOUS>2.0.CO;2.

[103] Y. He, A. Tablada, N.H. Wong, A parametric study of angular road patterns on pedestrian ventilation in high-density urban areas, Building and Environment. 151 (2019) 251–267. https://doi.org/10.1016/j.buildenv.2019.01.047.

[104] W. Wang, X. Wang, E. Ng, The coupled effect of mechanical and thermal conditions on pedestrian-level ventilation in high-rise urban scenarios, Building and Environment. 191 (2021) 107586. https://doi.org/10.1016/j.buildenv.2021.107586.

[105] R. Violette, E. De Langre, J. Szydlowski, Computation of vortex-induced vibrations of long structures using a wake oscillator model : Comparison with DNS and experiments, 85 (2007) 1134–1141. doi:10.1016/j.compstruc.2006.08.005.

[106] R. Bhatt, M.M. Alam, Vibrations of a square cylinder submerged in a wake, J. Fluid Mech. 853 (2018) 301–332.

[107] J. Zhao, J. Leontini, D. Lo Jacono, J. Sheridan, The effect of mass ratio on the structural response of a freely vibrating square cylinder oriented at different angles of attack, J. Fluids Struct. 86 (2019) 200–212. doi:10.1016/j.jfluidstructs.2019.02.008.

[108] B. Qin, M.M. Alam, Y. Zhou, Free vibrations of two tandem elastically mounted cylinders in crossflow, J. Fluid Mech. 861 (2019) 349–381. doi:10.1017/jfm.2018.913.

[109] R.D. Blevins, R.H. Scanlan, Flow-induced vibration, (1977).

[110] W. Sun, S. Jo, J. Seok, Development of the optimal bluff body for wind energy harvesting using the synergetic effect of coupled vortex induced vibration and galloping phenomena, Int. J. Mech. Sci. 156 (2019) 435–445. doi:https://doi.org/10.1016/j.ijmecsci.2019.04.019.

[111] M.M. Bernitsas, K. Raghavan, Y. Ben-Simon, E.M.H. Garcia, VIVACE (Vortex Induced Vibration Aquatic Clean Energy): A New Concept in Generation of Clean and Renewable Energy From Fluid Flow, in: 2006: pp. 619–637. doi:10.1115/OMAE2006-92645.

[112] NASA, GSFC, J. Schmaltz, M.L.R.R. Team, Cloud vortices off Heard Island, south Indian Ocean., NASA Goddard Sp. Flight Cent. (2015). https://commons.wikimedia.org/wiki/File:Cloud_vortices_(22531636120).jpg (accessed January 14, 2020).

[113] J. Wagner, Visualisation of the Von Kármán vortex sheet behind a circlular cylinder in air flow., (2014). https://commons.wikimedia.org/wiki/File:Karmansche_Wirbelstr_kleine_Re.JPG (accessed January 14, 2020).

[114] V. Strouhal, Über eine besondere Art der Tonerregung, Ann. Phys. 241 (1878) 216–251.

[115] A. Roshko, On the drag and shedding frequency of two-dimensional bluff bodies, (1954).

[116] Chu CR, Chiu YH, Tsai YT, Wu SL. Wind-driven natural ventilation for buildings with two openings on the same external wall. Energy Build 2015; 108:365–72. https://doi.org/10.1016/j.enbuild.2015.09.041.

[117] King MF, Khan A, Delbosc N, Gough HL, Halios C, Barlow JF, et al. Modelling urban airflow and natural ventilation using a GPU-based lattice-Boltzmann method. Build Environ 2017; 125:273–84. https://doi.org/10.1016/j.buildenv.2017.08.048.

[118] T. Kobayashi, M. Sandberg, T. Fujita, E. Lim, N. Umemiya, Simplified estimation OF wind-induced natural ventilation rate caused BY turbulence for a room with minute wind pressure, in: Proc. — Roomvent Vent, vol. 2018, 2018, pp. 613–618. https://www.lyyti.fi/reg_att/efA658E7F74904eE7C/D78bE5731da5113EF848.pdf.

[119] H.Y. Zhong, D.D. Zhang, D. Liu, F.Y. Zhao, Y. Li, H.Q. Wang, Two-dimensional numerical simulation of wind driven ventilation across a building enclosure with two free apertures on the rear side: Vortex shedding and "pumping flow mechanism," J. Wind Eng. Ind. Aerodyn. 179 (2018) 449–462. doi:10.1016/j.jweia.2018.07.002.

[120] H.Y. Zhong, D.D. Zhang, Y. Liu, D. Liu, F.Y. Zhao, Y. Li, H.Q. Wang, Wind driven "pumping" fluid flow and turbulent mean oscillation across high-rise building enclosures with multiple naturally ventilated apertures, Sustain. Cities Soc. 50 (2019) 101619. doi:10.1016/j.scs.2019.101619.

[121] H.-Y. Zhong, Y. Jing, Y. Liu, F.-Y. Zhao, D. Liu, Y. Li, CFD simulation of "pumping" flow mechanism of an urban building affected by an upstream building in high Reynolds flows, Energy Build. (2019). doi:10.1016/j.enbuild.2019.07.047.

[122] M. Shirzadi, M. Naghashzadegan, P. A. Mirzaei, Improving the CFD modelling of cross-ventilation in highly-packed urban areas, Sustain. Cities Soc. 37 (2018) 451–465. doi:10.1016/j.scs.2017.11.020.

[123] D.A. Yoder, J.R. DeBonis, N.J. Georgiadis, Modeling of turbulent free shear flows, Comput. Fluids. 117 (2015) 212–232. doi:10.1016/j.compfluid.2015.05.009.

[124] M. Ricci, L. Patruno, I. Kalkman, S. de Miranda, B. Blocken, Towards LES as a design tool: Wind loads assessment on a high-rise building, J. Wind Eng. Ind. Aerodyn. 180 (2018) 1–18. doi:10.1016/j.jweia.2018.07.009.

[125] J. Liu, J. Niu, C.M. Mak, Q. Xia, Detached eddy simulation of pedestrian-level wind and gust around an elevated building, Build. Environ. 125 (2017) 168–179. doi:10.1016/j.buildenv.2017.08.031.

[126] Y. Tominaga, A. Mochida, S. Murakami, S. Sawaki, Comparison of various revised k-ε models and LES applied to flow around a high-rise building model with 1:1:2 shape placed within the surface boundary layer, J. Wind Eng. Ind. Aerodyn. 96 (2008) 389–411. doi:10.1016/j.jweia.2008.01.004.

[127] J. Shao, J. Liu, J. Zhao, Evaluation of various non-linear k-e{open} models for predicting wind flow around an isolated high-rise building within the surface boundary layer, Build. Environ. 57 (2012) 145–155. doi:10.1016/j.buildenv.2012.04.018.

[128] S. Huang, Q.S. Li, S. Xu, Numerical evaluation of wind effects on a tall steel building by CFD, J. Constr. Steel Res. 63 (2007) 612–627. doi:10.1016/j.jcsr.2006.06.033.

[129] J. Liu, J. Niu, CFD simulation of the wind environment around an isolated high-rise building: An evaluation of SRANS, LES and DES models, Build. Environ. 96 (2016) 91–106. doi:10.1016/j.buildenv.2015.11.007.

[130] Y. Wu, J. Niu, Numerical study of inter-building dispersion in residential environments: Prediction methods evaluation and infectious risk assessment, Build. Environ. 115 (2017) 199–214. doi:10.1016/j.buildenv.2017.01.029.

[131] A. Okajima, Strouhal numbers of rectangular cylinders, (1982).

[132] T. Nakagawa, Vortex shedding behind a square cylinder in transonic flows, J. Fluid Mech. 178 (1987) 303–323. doi:10.1017/S002211208700123X.

[133] C.W. Knisely, Strouhal numbers of rectangular cylinders at incidence: A review and new data, J. Fluids Struct. 4 (1990) 371–393. doi:10.1016/0889-9746(90)90137-T.

[134] H. NAKAGUCHI, K. HASHIMOTO, S. MUTO, An Experimental Study on Aerodynamic Drag of Rectangular Cylinders, J. Japan Soc. Aeronaut. Eng. 16 (1968) 1–5. doi:10.2322/jjsass1953.16.1.

[135] F. Wang, K.M. Lam, G.B. Zu, L. Cheng, Coherent structures and wind force generation of square-section building model, J. Wind Eng. Ind. Aerodyn. 188 (2019) 175–193. doi:10.1016/j.jweia.2019.02.019.

[136] Y. Hui, K. Yuan, Z. Chen, Q. Yang, Characteristics of aerodynamic forces on high-rise buildings with various façade appurtenances, J. Wind Eng. Ind. Aerodyn. 191 (2019) 76–90. doi:10.1016/j.jweia.2019.06.002.

[137] C. Zheng, Z. Liu, T. Wu, H. Wang, Y. Wu, X. Shi, Experimental investigation of vortex-induced vibration of a thousand-meter-scale mega-tall building, J. Fluids Struct. 85 (2019) 94–109. doi:10.1016/j.jfluidstructs.2018.12.005.

[138] A. Fluent, User's Guide Release 19.2, Ansys Inc. (2018).

[139] J. Franke, Best practice guideline for the CFD simulation of flows in the urban environment, Meteorological Inst., 2007.

[140] B. Blocken, T. Stathopoulos, J. Carmeliet, CFD simulation of the atmospheric boundary layer: wall function problems, Atmos. Environ. 41 (2007) 238–252. doi:10.1016/j.atmosenv.2006.08.019.

[141] N.J. Georgiadis, D.P. Rizzetta, C. Fureby, Large-eddy simulation: Current capabilities, recommended practices, and future research, AIAA J. 48 (2010) 1772–1784. doi:10.2514/1.J050232.

[142] M. Ricci, L. Patruno, S. de Miranda, Wind loads and structural response: Benchmarking LES on a low-rise building, Eng. Struct. 144 (2017) 26–42. doi:10.1016/j.engstruct.2017.04.027.

[143] Ramponi R, Blocken B. CFD simulation of cross-ventilation for a generic isolated building : Impact of computational parameters. Build Environ 2012;53:34–48. https://doi.org/10.1016/j.buildenv.2012.01.004.

[144] Y. Tominaga, A. Mochida, R. Yoshie, AIJ guidelines for practical applications of CFD to pedestrian wind environment around buildings, 96 (2008) 1749–1761. doi:10.1016/j.jweia.2008.02.058.

[145] M. Germano, U. Piomelli, P. Moin, W.H. Cabot, A dynamic subgrid-scale eddy viscosity model, Phys. Fluids A. 3 (1991) 1760–1765. doi:10.1063/1.857955.

[146] Arinami Y, Akabayashi S, Tominaga Y, Sakaguchi J. Performance evaluation of single-sided natural ventilation for generic building using large-eddy simulations: Effect of guide vanes and adjacent obstacles. Build Environ 2019. https://doi.org/10.1016/j.buildenv.2019.01.021.

[147] Jan-Jan Soon, Angela Siew-Hoong Lee, Hock-Eam Lim, Izian Idris & William Yong-Keong Eng (2020) Cubicles or corner offices? Effects of academic performance on university graduates' employment likelihood and salary, Studies in Higher Education, 45:6, 1233-1248, DOI: 10.1080/03075079.2019.1590689

[148] ANSI/ASHRAE Standard 62.1-2019, Ventilation for Acceptable Indoor Air Quality.

[149] Celik, I. B., Cehreli, Z. N., and Yavuz, I. (2005). "Index of Resolution Quality for Large Eddy Simulations." ASME. J. Fluids Eng. September 2005; 127(5): 949–958.

[150] Pope, S. (2000). Turbulent Flows. Cambridge: Cambridge University Press. doi:10.1017/CBO9780511840531

[151] Nestoras Antoniou, Hamid Montazeri, Hans Wigo, Marina K.-A. Neophytou, Bert Blocken, Mats Sandberg, CFD and wind-tunnel analysis of outdoor ventilation in a real compact heterogeneous urban area: Evaluation using "air delay", Building and Environment, Volume 126, 2017, Pages 355-372, ISSN 0360-1323, https://doi.org/10.1016/j.buildenv.2017.10.013.

[152] Lilly DK. A proposed modification of the Germano subgrid-scale closure method. Phys Fluids A 1992; 4:633–5. https://doi.org/10.1063/1.858280.

[153] S. Murakami, A. Mochida, On turbulent vortex shedding flow past 2D square cylinder predicted by CFD, Journal of Wind Engineering and Industrial Aerodynamics, Volumes 54–55, 1995, Pages 191-211, ISSN 0167-6105, https://doi.org/10.1016/0167-6105(94)00043-D.

[154]   Ohtsuki Y., Wind tunnel experiments on aerodynamic forces and pressure distributions of rectangular cylinders in a uniform flow, Proc. 5th Symp. on Wind Effects on Structures, 1978, 169-175.

[155]   Bearman, P., & Obasaju, E. (1982). An experimental study of pressure fluctuations on fixed and oscillating square-section cylinders. Journal of Fluid Mechanics, 119, 297-321. doi:10.1017/S0022112082001360

[156]   M. Schatzmann, H. Olesen, J. Franke, COST 732 Model Evaluation Case Studies: Approach and Results, Cost Action, 2010.

[157]   G. Carrilho da Graça, N.C. Daish, P.F. Linden, A two-zone model for natural cross-ventilation, Building and Environment, Volume 89, 2015, Pages 72-85, ISSN 0360-1323, https://doi.org/10.1016/j.buildenv.2015.02.014.

[158]   Linden, P. F. (1999). The fluid mechanics of natural ventilation. Annual review of fluid mechanics, 31(1), 201-238.